

VERY HIGH FREQUENCY
NANOELECTROMECHANICAL
RESONATORS AND THEIR
CHEMICAL SENSING
APPLICATIONS

Thesis by

Mo Li

In Partial Fulfillment of the Requirements for the
degree of
Doctor of Philosophy



CALIFORNIA INSTITUTE OF TECHNOLOGY

Pasadena, California

2007

(Defended May 11th, 2007)

© 2007

Mo Li

All Rights Reserved

ACKNOWLEDGEMENTS

I want to thank all the people who have helped me throughout the research toward this thesis. Firstly, I would like to acknowledge my advisor, Dr. Michael Roukes, who took me on to his group since my first day at Caltech. During years in his group, he generously provided me with support, inspiration, guidance, encouragement, and freedom to pursue my research ideas. Secondly, I am very thankful to Dr. Hong Tang, who trained me on many experiment skills, shared me with his research ideas and thoughts, and mentored me on a day-to-day base. In fact, several research topics in this thesis began with his original ideas. I am indebt to Prof. Nate Lewis, Prof. Marc Bockrath, and Prof. Kerry Vahala, for serving in my exam committee. I am also privileged to work with Dr. Edward Myers and Dr. Sequoyah Aldridge on the DARPA MGA project. We worked very hard together, sometimes all day and all night, and successfully met several very harsh milestones before the impending deadlines. The whole Roukes group has always been a source of support and inspiration for me. My thanks go to Philip Feng, Sotiris Masmanidis, Ben Gudlewski, Steve Stryer, Igor Bargatin, Inna Kozinsky, Blake Axelord, Jessica Arlett, Renaud Richard, Wonhee Lee, Rassul Karabalin, and all the others in the group. I am also very grateful to Dr. Joe Simonson and Dr. Joshua Whiting, our collaborators at Sandia National Laboratories, for their help in building our GC systems and numerous very helpful discussions.

Finally, I wish to thank my parents and my sister in China, for their endless love and support to me during my more-than-twenty-year-long journey of study in schools.

To my wife

ABSTRACT

Nanoelectromechanical systems (NEMS) have been proven to be ultrasensitive sensors for a variety of physical variables with unprecedented sensitivity, including force, mass, electrical charge, magnetic field, pressure, and heat. This thesis is intended to discuss using NEMS devices as chemical gas sensors, in a portable and compact total chemical analysis system. An integrated transduction method using piezoresistive metallic thin film is described, which enables both fabrication and operation of nanoscale NEMS resonator devices with resonance frequency up to very high frequency (VHF). The advantages over using traditional doped semiconductor film as piezoresistive material is discussed. Performance and noise properties of the devices are carefully characterized. The dependence between quality factor, device dimension, and pressure is studied, and very high quality factor is obtained with devices at nanoscale dimensions, indicating advantages over their microscale counterparts. Subsequently, the resonator devices are employed as a mass sensor, demonstrating attogram scale mass sensitivity in ambient conditions. Application of these devices as detectors in a gas chromatographic (GC) system is then described, together with method of coating them with functional polymeric film. Detection of multiple analytes of nerve gas simulants with ultrahigh speed, superior sensitivity, and excellent selectivity is achieved. The replacement of conventional bulky detectors with an NEMS detector makes fully integrated microscale gas analysis system possible, which has promising potential applications in health care, medical science, and environmental science.

Table of Contents

ACKNOWLEDGEMENTS	iii
ABSTRACT	v
Table of Contents	vi
List of Figures	viii
List of tables	xiii
Chapter 1 Overview: nanoelectromechanical systems (NEMS) for chemical sensing..	1
1.1 Nanomechanical mass sensing.....	3
1.2 Micro- and nanomechanical chemical sensing	5
1.3 Scaling metrics for mass and chemical concentration sensing	6
1.4 Reference	9
Chapter 2 Self-sensing NEMS using metallic piezoresistive detection.....	10
2.1 Introduction to piezoresistivity	11
2.2 Rationale of using metallic piezoresistive detection on NEMS.....	17
2.3 Cantilever design	21
2.4 Fabrication of nanocantilevers.....	25
2.5 Low frequency cantilevers.....	29
2.6 HF/VHF cantilevers	34
2.7 Operation of high frequency nanocantilevers in ambient conditions	38
2.8 Piezoresistive microcantilevers for AFM	45

2.9	Reference	54
Chapter 3	Measurement techniques.....	57
3.1	Noise measurement: thermomechanical noise, Johnson noise and 1/f noise....	58
3.1.1	<i>Johnson noise and thermomechanical noise measurements</i>	59
3.1.2	<i>1/f noise</i>	67
3.2	Frequency down-conversion measurement.....	74
3.3	Phase-locked loop (PLL)	78
1.8	Reference	88
Chapter 4	Nanomechanical chemical gas analysis with gas chromatography (GC)	90
4.1	Introduction of gas chromatography: column and detectors.....	91
4.2	NEMS mass sensor in ambient condition	96
4.3	Polymeric film functionalized NEMS detector in GC	101
4.4	Reference	122
Chapter 5	Conclusion and future work.....	125
5.1	Conclusion	125
5.2	Future work.....	127
5.3	Reference	131
Appendix A	Electrochemical deposition of nano-magnet tip on microscale scanning probes.....	132
	Reference	138

List of Figures

Figure 2-1 Electrical conductor deforms under mechanical force.....	12
Figure 2-2 Impedance matching from high-impedance nanoscale devices to radio frequency electronics	19
Figure 2-3 Finite elements simulation of a Π shape cantilever under deformation.....	22
Figure 2-4 Fabrication process flow	26
Figure 2-5 SEM images of cantilevers made of 100 nm thick SiC and with 30 nm gold film.....	27
Figure 2-6 A doubly clamped beam with metalized bottom gate.....	28
Figure 2-7 A trampoline resonator with integrated heater and piezoresistive transducer.	28
Figure 2-8 Fundamental mode resonance response of cantilever from Figure 2-5a at constant DC bias voltage and varying bias voltage.	30
Figure 2-9 Fundamental mode resonance response of cantilever from Figure 2-5a at constant actuation voltage and varying bias voltage.....	30
Figure 2-10 Second mode resonance response of cantilever from Figure 2-5a at constant bias voltage and varying actuation voltage.....	31
Figure 2-11 Second mode resonance response of cantilever from Figure 2-5a at constant actuation voltage and varying bias voltage.....	31
Figure 2-12 Fundamental mode resonance response of cantilever from Figure 2-5b at constant bias voltage and varying actuation voltage. Dotted lines show cantilever's resonance response in air.	32
Figure 2-13 Second mode resonance response of cantilever b) at constant bias voltage and varying actuation voltage.....	33

Figure 2-14 Fundamental mode resonance response of cantilever from Figure 2-5c at constant bias voltage and varying actuation voltage, plotted in log scale.	35
Figure 2-15 Fundamental resonance mode of cantilever from Figure 2-5d, both in vacuum (red) and at 1 atm (blue), with actuation voltage varying from 100 mV to 500 mV.....	37
Figure 2-16 Resonance quality factor for cantilever from Figure 2-5b, c and d when operated in air at various pressures.	41
Figure 2-17 Knudsen number and air flow regime at varying pressure, for cantilever beams with different width (2 μm , 400 nm, 8 nm, and 2 nm respectively).....	42
Figure 2-18 Quality factor and pressure dependence of nanocantilever in different ambient gases.....	44
Figure 2-19 Commercial AFM microcantilever coated with gold film and processed with focused ion beam for piezoresistive detection.....	46
Figure 2-20 Piezoresistively detected resonance of commercial microcantilevers in air and vacuum with varying actuation voltage.....	46
Figure 2-21 Frequency down mixing method detected resonance of commercial microcantilever.	47
Figure 2-22 Modified AFM probe head and electrical setup to measure piezoresistive AFM signal.....	48
Figure 2-23 Diagram of modified signal configuration for piezoresistive readout.....	50
Figure 2-24 Images of silicon calibration grating sample, with 30 nm step height.....	52
Figure 2-25 Scan trace of calibration grating step of 30 nm.....	53
Figure 3-1 Circuitry to measure NEMS thermomechanical noise.....	62

Figure 3-2 Thermomechanical noise spectrum measured on a low frequency cantilever.	63
Figure 3-3 Thermomechanical noise spectrum measured on a VHF cantilever.....	64
Figure 3-4 Cantilever made of 30 nm silicon carbide, with very low force constant of 10 mN/m.	66
Figure 3-5 AC bridge setup to measure 1/f noise low resistance NEMS	69
Figure 3-6 Noise figure contours of Stanford Research SR 554 amplifier.....	69
Figure 3-7 Low frequency noise spectrum of 1 k Ω metal film resistor.....	71
Figure 3-8 Low frequency noise spectrum of two NEMS cantilever devices.	73
Figure 3-9 Frequency down-conversion piezoresistive measurement.....	76
Figure 3-10 Amplitude and phase of a cantilever measured with DC bias and a network analyzer.....	77
Figure 3-11 Amplitude and phase of a cantilever measured with the frequency down- conversion method.....	77
Figure 3-12 Basic phase lock loop (reproduced as in Ref 11).....	78
Figure 3-13 NEMS embedded in a phase-locked loop.....	79
Figure 3-14 Amplitude and phase response at resonance frequency of a typical cantilever in air	80
Figure 3-15 Polar plot of a NEMS amplitude-phase frequency response	81
Figure 3-16 Piezoresistive frequency down-conversion NEMS phase-locked loop	82
Figure 3-17 Y quadrature signal versus drive frequency of a typical NEMS cantilever...	83
Figure 3-18 Phase-locked loop gain measurement with loop gain value set by various lock-in sensitivities	85
Figure 3-19 PLL Frequency stability versus loop gain K.....	86

Figure 4-1 Schematic representation of the chromatographic process.	92
Figure 4-2 Instrument diagram of a GC (from www.practicingoilanalysis.com).....	94
Figure 4-3 Coating cantilever resonators with polymer	98
Figure 4-4 Frequency shift and quality factor reduction of the resonance response of the cantilever before (red) and after (blue) coating	98
Figure 4-5 Real-time NEMS chemisorption measurements.	100
Figure 4-6 Setup to test NEMS detector with commercial GC system with FID detector connected in serial.....	104
Figure 4-7 Gas chromatogram from NEMS detector (purple) and FID detector (blue), showing peaks from five analytes (3MH, DMMP, DIMP, DEMP, MS) with similar concentration.....	108
Figure 4-8 Gas chromatogram from NEMS detector (purple) and FID detector (blue), showing peaks from ten analytes (C8, Toluene, 3MH, DMMP, DIMP, DEMP, DCH, NAPTH, C11, MS) with similar concentration	109
Figure 4-9 Faster GC separation with 1 meter long column.....	109
Figure 4-10 Micro-machined flow chamber with microfluidic flow channel and the assembly with NEMS device chip.	110
Figure 4-11 Very fast GC chromatogram from both NEMS (red) and FID (blue) detectors, obtained using nanoliter volume chamber.	113
Figure 4-12 Relative response of DKAP-coated NEMS and FID detectors to various analytes	114
Figure 4-13 Chromatogram of thirteen analytes from cantilever resonators coated with DKPA and PCL polymer, respectively.....	115

Figure 4-14 Relative response of DKAP- and PCL-polymer coated NEMS to various analytes	115
Figure 4-15 Maximum NEMS detector frequency shift at various averaged DIMP concentrations..	117
Figure 4-16 Relative response of the NEMS detector with 10 nm thick polymer coating.	119
Figure 4-17 The function of equation (4.8) can be approximated using the square root of t when $m(t)/m_{max} < 0.6$	120
Figure 4-18 Spatial (depth) distribution of gas molecule concentration inside the polymer at various times (0.001, 0.01, 0.1, and 1 τ)	121
Figure 5-1 Differentially coated NEMS resonator array	129
Figure A-1 Electrodeposition setup	133
Figure A- 2 Deposition rate versus current density	134
Figure A-3 Patterning the PMMA e-beam resist on a seed layer for self-aligned electrodeposition.....	135
Figure A-4 Array of nanomagnets with dimension of 2 μm high and 300 nm wide	136
Figure A-5 A 500 nm by 2 μm permalloy nanomagnet on SiN membrane.....	137
Figure A-6 A mushroom shaped overgrown nanomagnet on the tip of a release cantilever	137

List of tables

Table 1-1 Scaling metrics of various quantities of a rectangular beam.....	7
Table 2-1 Poisson's ratio, guage factor, and resistivity of typical metals (Data from reference [1] and webelements.com)	13
Table 2-2 Piezoresistive coefficients for n-type and p-type silicon and germanium ⁷	15
Table 2-3 Properties of gold and silicon carbide	24
Table 2-4 Geometrical parameters of typical cantilevers	24
Table 2-5 Calculated and finite elements simulate results of cantilever parameters	24
Table 2-6 Parameters of typical cantilever devices as shown in Figure 2-5.....	39
Table 2-7 Properties of different ambient gases	44
Table 3-1 Phase-locked loop parameters measured and calculated.....	85
Table 4-1 Comparison of areal mass sensitivity of various acoustic devices and NEMS resonators.....	102
Table 4-2 List of tested chemicals and their formulas, densities, and molecular weights (MW), including CWA simulants (*) and interferents	107
Table A-1 Electrodeposition solution for permalloy (Fe ₂₀ Ni ₈₀) electro-deposition	133
Table A-2 Exposure dosage for hole patterns using on bilayer PMMA resist.	135

Chapter 1

Overview: nanoelectromechanical systems (NEMS) for chemical sensing

Modern advances in semiconductor fabrication technologies developed by the microelectronics industry and research have enabled very large-scale integration (VLSI) of billions of transistors onto a single chip. Nanotechnology, the technology based on nanometer scale dimension, was envisioned decades ago by Richard Feynman in 1959, emerged only after these fabrication technologies were rapidly developed after the 1980s. Only a few years later after Feynman's famous talk, microscale mechanical devices were proposed as a means to improve the state-of-the-art transistors at that time^{1,2}. The field of microelectromechanical systems, or MEMS, debuted also only when enough microfabrication techniques and tools were available, in the late 1980s. Then in the 1990s a new research field crossing over both nanotechnology and MEMS emerged, as a result of intensive and extensive research activities in both fields. That field is nanoelectromechanical systems or NEMS, which studies and develops electromechanical devices with nanoscale dimensions^{3,4}.

MEMS, the first wave of miniaturization of mechanical devices from macroscopic to microscale, have demonstrated lots of fantastic success. Examples include the accelerometer that is used to deploy the airbags in almost every modern automobiles, the digital light processor (DLP) device in color projectors, and the printing head in advanced

inkjet printers, only to name a few. Although NEMS, further miniaturization of MEMS to nanoscale, is still a nascent research field, many remarkable milestones have already been demonstrated. These achievements include the first microwave frequency nanomechanical resonator⁵, detection of single electron spin⁶, measurement of zeptogram scale mass⁷, mechanical motion detection near the quantum limit⁸, and so on. These accomplishments demonstrate the capability of NEMS which stems from their unique characteristics of their nanoscale dimensions. NEMS devices promise a variety of novel applications with superior performance.

This thesis focuses on the application of NEMS resonator devices for mass sensing and chemical gas sensing applications. In this overview, aspects of these applications are discussed and explained. Scaling metrics of some important parameters of the NEMS resonators related to mass and chemical gas sensing are derived. The results indicate the improvement of performance by miniaturization of the device dimensions, as demonstrated in the following chapters.

1.1 Nanomechanical mass sensing

A sensor that measures the mass change of itself is called a gravimetric sensor. Types of gravimetric sensors include quartz crystal microbalance (QCM), surface acoustic wave (SAW), bulk acoustic wave (BAW), and flexural plate wave (FPW) devices and other microscale mechanical resonators based on MEMS technologies. All these devices are operated at their characteristic resonance frequencies, and their frequencies are measured in response to the change of additive mass on the sensors' active surfaces. Since frequency measurement is regarded as the most precise of all science measurements (for example, National Institute of Standard and Technology's cesium fountain atomic clocks), and given the excellent frequency stabilities of these sensors, resonance-frequency-based gravimetric sensors provide mass sensing resolution far superior to any other sensing methods.

NEMS resonators are also a type of gravimetric sensor. They have demonstrated orders of magnitude improvement in mass sensing resolution than the above-mentioned macroscopic sensors. This improvement stems from NEMS resonators' miniature total mass, very high resonance frequency, and remarkable frequency stability, as indicated clearly from the expression of mass-frequency responsivity:

$$\mathfrak{R} = \frac{\partial \omega_0}{\partial M_{eff}} = -\frac{\omega_0}{2M_{eff}}. \quad (1.1)$$

This equation is derived from the expression of the eigen-frequency of a simple harmonic oscillator: $\omega_0 = \sqrt{K_{eff} / M_{eff}}$, where ω_0 is the angular frequency, M_{eff} is the effective mass, and K_{eff} is the effective spring constant of the resonator. The minimum resolvable

mass change of the resonator is then determined by the minimum measurable frequency change and the mass responsivity:

$$\delta m = \frac{\delta \omega_0}{|\Re|} = \left(\frac{\delta \omega_0}{\omega_0} \right) \cdot 2M_{eff}. \quad (1.2)$$

From equation (1.2), it is clear that the higher the frequency measurement accuracy $\delta \omega_0 / \omega_0$, and the smaller the effective resonator mass, the lower is the minimum resolvable mass δm . NEMS resonators have demonstrated better or comparable frequency stability with other microscale gravimetric sensors, in the range of one part per million (10^{-6}) to ten parts per billion (10^{-8}). But the effective mass of NEMS resonators is much smaller — at pictogram scale for typical high-frequency silicon or silicon carbide cantilevers, and at femtogram scale for UHF/microwave frequency doubly clamped beams and nanowires. So inherently, NEMS resonators will have unprecedented mass sensing resolution. Recent progress has achieved zeptogram scale mass sensing on an ultra-high-frequency NEMS resonator. The experiment demonstrated sensing physisorption of 100 zeptogram xenon atoms on the device surface at low temperature and in vacuum, with noise level at only 7 zeptogram. This mass resolution corresponds to the mass of one 4 kDa macromolecule or protein molecule, or 30 Xenon atoms. In this thesis, experiments carried out at room temperature and atmosphere pressure instead, demonstrating the sensing of single attogram gas molecules with 100 zeptogram noise level, will be described in detail. This demonstrates another benchmark for mass sensing in ambient conditions. With fast progresses in fabrication and measurement techniques, the ultimate goal of mass sensing at single Dalton level should be within reach in the very near future, so that mass spectroscopy can be implemented with these nanoscale devices

in an integrated and compact form which will have tremendous application opportunities in chemical and biological science and technology.

1.2 *Micro- and nanomechanical chemical sensing*

Mechanical gravimetric sensors can be applied straightforwardly for chemical sensing applications⁹. For that purpose, the mass of targeted chemical analytes of interest will be measured when the analyte molecules adsorb (absorb) onto (into) the active surface of the sensor. There are two types of radically different adsorption mechanisms between adsorbate molecules and surfaces: chemi-sorption and physisorption. For chemi-sorption, the adsorbate molecules form a direct chemical bond with the surface, while for physisorption, only weak physical forces (van der Waals force) hold adsorbate molecules on the surface. These two adsorption mechanisms can be quantitatively discriminated between by their adsorption energy. Typically, chemi-sorption energies are 80 - 400 kJ/mol, compared to physisorption which has adsorption energy less than 40 kJ/mol. However, in many cases, the distinction between these two mechanisms is not that clear and necessary. Details of the change and perturbation of molecular electron states, and their interaction with surface atoms upon adsorption need to be taken into consideration. Usually, a sorption process involves both physisorption and chemi-sorption processes.

To obtain both better chemical sensitivity and selectivity, modification of the sensor surface with functional coating material is essential. Coating materials employed for different sensing purpose include polymeric films, thiols, silanes, zeolites, metals, metal oxides, zeolites, antibodies, enzymes, lipids, and ssDNAs, each tailored for specific applications. For vapor-phase sensing of organic compounds, polymeric films are the

most often used coating material. Details of the vapor-phase sensing using polymeric films on gravimetric sensors will be addressed in Chapter 4.

1.3 Scaling metrics for mass and chemical concentration sensing

For vapor-phase chemical sensing, the purpose is to measure the concentration of the analytes, usually at very low level, in the ambient gaseous environment. Thus, the sensor's sensitivity of concentration sensing is the main concern in this scenario. The excellent mass sensitivity of a gravimetric sensor does not automatically transfer to good concentration sensitivity, for the surface area of the sensor has to be taken into account. Whether or not scaling down the dimensions of the sensor to nanoscale will improve concentration sensitivity, as it does for mass sensitivity, is not clear at the first glance. It is advisable to see qualitatively how scaling the dimensions will change the properties of the device.

Take a beam with a rectangular cross section for example. Assume its length L , width W , and thickness t , can be scaled down simultaneously. We can write $L=al$, $W=bl$, $t=cl$, so that they all are proportional to a linear dimension l . In Table 1-1, expressions of various important mechanical properties of the beam and theoretical sensitivities of the beam as a sensor are listed, as well as how these expressions scale with dimension l . In the table, Δf is the measurement bandwidth, A_{eff} is the effective surface area of the sensor, DR is the linear dynamic range, s is the sticking coefficient of the gas molecules at the sensor surface, and m_0 is the molecular mass of the gas species. However, some

quantities, such as quality factor Q and dynamic range DR , are assumed to have no dependence on the dimensions of the device, as suggested from reported experimental results showing that no simple dependence of these quantities on dimension can be found¹⁰. Yet this assumption holds only to a limited extent and remains to be checked in a more complete, detailed modeling of each device.

Table 1-1 Scaling metrics of various quantities of a rectangular beam

Resonance frequency	$f_0 = \frac{\alpha}{2\pi} \sqrt{\frac{E}{\rho}} \frac{t}{L^2}$	l^{-1}
Force constant	$k = \beta E \frac{wt^3}{L^3}$	l
Mass responsivity	$\mathfrak{R} = \frac{f_0}{2M_{eff}} = \alpha \sqrt{\frac{E}{\rho^3}} \frac{1}{wL^3}$	l^{-4}
Minimum resolvable mass	$\delta m = \frac{1}{\mathfrak{R}} \left(\frac{\omega_0}{Q} \Delta f \right)^{1/2} 10^{(-DR/20)}$	$l^{3.5}$
Minimum resolvable concentration	$\delta c = \frac{2.5}{A_{eff} \mathfrak{R} \cdot p_0 \cdot s} \sqrt{\frac{k_B T}{m_0} \frac{\omega_0}{Q} \Delta f^3} \cdot 10^{-(DR/20)}$	$l^{1.5}$
Areal mass sensitivity	$S_m = \frac{\mathfrak{R}}{f_0} A_{eff} = -\frac{A_{eff}}{2M_{eff}}$	l^{-1}

As discussed previously, both the resonance frequency and mass responsivity will increase, while the force constant will decrease, as the dimension l is scaled down. The thermomechanical noise limited minimum resolvable mass change decreases as $l^{3.5}$ ¹¹. To

convert this mass resolution to concentration resolution, we use the equation of flux dependent adsorption rate:

$$r_a = \frac{2}{5} \frac{p}{\sqrt{mk_b T}} s. \quad (1.3)$$

So within measurement time $\tau = 1/\Delta f$, the total mass of adsorbed gas molecules is $\Delta m = (r_a A_{eff} m_0) \cdot \tau$. If Δm is replaced with the minimum resolvable mass, and the concentration of the gas species is defined as the ratio of its partial pressure to ambient pressure: $c = p/p_0$, we can define the minimum resolvable concentration of the sensor δc . Using the scaling method, it is found that δc decreases with l as $l^{1.5}$, indicating the improved concentration sensitivity of the sensor when its dimensions are scaled downward. Also, the areal sensitivity S_m is a frequently used quantity for gravimetric sensors, and it also improves as l^{-1} when l decreases. (It will be noted in Chapter 4 that the effective thickness of the sensor plays the major role here.)

All of the above discussions explicate the advantages of nanoscale mechanical resonator sensors — they have both improved mass sensitivity and improved concentration sensitivity. They are therefore very promising for chemical sensing applications when relative concentration of vapor phase analytes is the objective of measurement. The work described in this thesis is motivated by these findings, and proves these predictions. Unprecedented sensitivity as well as substantially improved sensing speed have been successfully demonstrated, and will be discussed in detail.

1.4 Reference

- 1 Nathanso, H., et al. Resonant gate transistor. *IEEE Transactions on Electron Devices* **Ed14**, 117 (1967).
- 2 Newell, W. E. Miniaturization of tuning forks. *Science* **161**, 1320-1326 (1968).
- 3 Roukes, M. Plenty of room indeed. *Scientific American* **285**, 48 (2001).
- 4 Roukes, M. Nanoelectromechanical systems face the future. *Phys. World* **14**, 25-31 (2001).
- 5 Huang, X. M. H., et al. Nanodevice motion at microwave frequencies. *Nature* **421**, 496-496 (2003).
- 6 Rugar, D., et al. Single spin detection by magnetic resonance force microscopy. *Nature* **430**, 329-332 (2004).
- 7 Yang, Y. T., et al. Zeptogram-scale nanomechanical mass sensing. *Nano Lett.* **6**, 583-586 (2006).
- 8 LaHaye, M. D., et al. Approaching the quantum limit of a nanomechanical resonator. *Science* **304**, 74-77 (2004).
- 9 Hughes, R. C., et al. Chemical microsensors. *Science* **254**, 74-80 (1991).
- 10 Yasumura, K. Y., et al. Quality factors in micron- and submicron-thick cantilevers. *J. Microelectromech. Syst.* **9**, 117-125 (2000).
- 11 Ekinci, K. L., Yang, Y. T., and Roukes, M. L. Ultimate limits to inertial mass sensing based upon nanoelectromechanical systems. *J. Appl. Phys.* **95**, 2682-2689 (2004).

Chapter 2

Self-sensing NEMS using metallic piezoresistive detection

Measurement of nanoelectromechanical resonators with very high resonance frequency is challenging because the signal generated from the mechanical motion of the device is minuscule and buried in other parasitic or interference signals. Previously, typical readout methods such as magnetomotive and optical interferometry have been employed. However, these techniques require bulky setup, cryogenic temperatures or optical instruments that are not integratable to the chip scale. An alternative readout method is needed for efficient signal transduction from mechanical motion to electrical signal that is suitable for a very wide frequency range. For the future of large-scale integration of multiple NEMS devices with other micro- and nanoelectronics, this readout scheme also needs to be capable of being both scaled down to allow a high level of integration, and scaled up to allow large throughput fabrication and multiplexing of many devices that can be operated in parallel. Room temperature and atmosphere operation is also a prerequisite.

In this chapter, a method of utilizing the piezoresistivity of metallic film for reading out NEMS devices is described. Self-sensing NEMS resonator devices from low frequency up to very high frequency (VHF) is demonstrated. Noise and sensitivity

analysis is conducted based on measured data. Also, the dependence of resonance quality factor on ambient pressure of devices with various dimensions is studied. The attributes of metallic piezoresistive transduction scheme are manifested clearly by the measured data and theoretical analysis. Further, self-sensing cantilevers for atomic force microscopy (AFM) are also demonstrated, indicating promising application potential.

2.1 Introduction to piezoresistivity

Piezoresistivity is the effect that the resistance of an electrical conductor changes when it deforms under mechanical strain. It was first discovered by Lord Kelvin (William Thomson) in 1856. The geometrical deformation of a conductor implies that any conductor is piezoresistive, including both metal and semiconductor. The resistance-strain relation of piezoresistive material can be characterized by a figure of merit called gauge factor, defined as $\gamma = (dR/R)/(dL/L)$ — the relative change of resistance divided by the applied strain. The DC resistance of a uniform conductor with length L , cross section A , and electrical resistivity ρ is: $R = \rho L / A$. When the conductor is deformed, its partial resistance change can be calculated:

$$\frac{dR}{R} = \frac{d\rho}{\rho} + \frac{dL}{L} - \frac{dA}{A}. \quad (2.1)$$

If we know the Poisson's ratio of the material that the conductor is made of, equation (2.1) can be written as:

$$\frac{dR}{R} = \frac{d\rho}{\rho} + (1 + 2\nu)\frac{dL}{L} = \gamma \frac{dL}{L} \quad (2.2)$$

Thus we can find the expression for gauge factor is:

$$\gamma = (1 + 2\nu) + \frac{d\rho/\rho}{dL/L}. \quad (2.3)$$

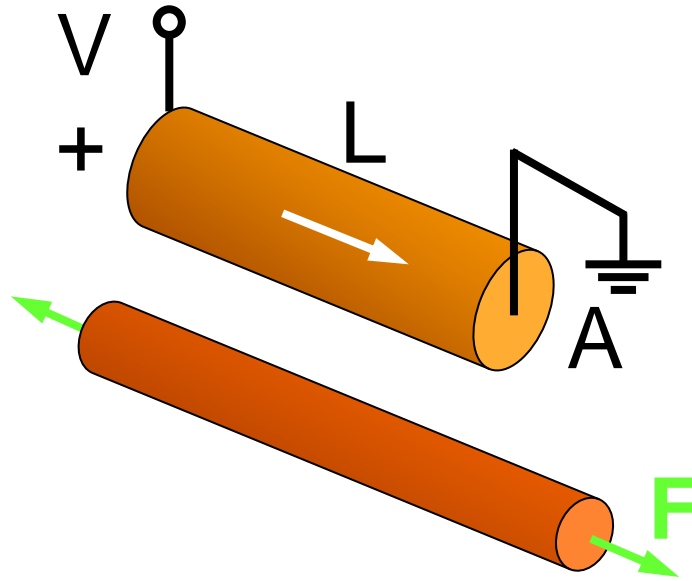


Figure 2-1 Electrical conductor deforms under mechanical force.

The first term in (2.3) derives solely from the geometrical deformation of the conductor. This effect is illustrated in Figure 2-1. For most conductive materials, Poisson's ratio is less than 0.5. For example, typical cited values for metals are 0.33 for aluminum, 0.42 for gold, 0.34 for copper, and 0.32 for titanium. So the contribution of the first term to gauge factor is less than 2. The second term stems from the conductivity change of the material under deformation. The value of this term can vary in three orders of magnitude for different materials with different conducting mechanisms. In typical metallic conductors (such as aluminum, copper, gold, platinum), this term is usually in the range of $1-3^{-1}$. In metals, a possible mechanism of this conductivity change is the modification of free electron path length caused by the elastic field generated by applied

stress², or in some magnetic metals, by the coupling between magnetoresistive and magnetostrictive effects. In general, including both terms, the gauge factor of bulk metallic conductor is commonly in the range of 1–3. Bulk values of Poisson’s ratio, gauge factor and resistivity of common metals are listed in Table 2-1.

Table 2-1 Poisson's ratio, gauge factor, and resistivity of typical metals

(Data from reference [1] and webelements.com)

Metal	Poisson’s ratio ν	Gauge factor γ	Electrical resistivity ρ ($\mu\Omega \cdot \text{cm}$)
Cu	0.35	1.96	1.7
Au	0.42	3.03	2.2
Al	0.34	2.17	2.65
Pd	0.39	2.23	10
Pt	0.39	2.54	10.6
Ni	0.30	1.88	7.0

Gauge factors of metallic thin films can be significantly different from the corresponding bulk values. The gauge factor of a particular metal film depends on its thickness, or the specific resistance of the film. This dependence can be divided into three regimes according to the film thickness. For relatively thick films (typically > 100 nm), their gauge factors approach the value of bulk. For the films of intermediate thickness (in the range of 100 nm to 10 nm) when the film is still continuous, the gauge factor has a lower value. This is due to the fact that for a two dimensional conductor, the translation factor of longitudinal deformation dL/L to cross sectional deformation dA/A equals only one Poisson ratio ν , instead of 2ν in a three dimensional conductor. For very thin films (less than 10 nm typically), it becomes discontinuous and approaches percolation regime that the conduction in the film is mainly by thermally excited electron hopping or

tunneling between isolated metal islands or particles. Thus, the electrical conduction becomes very sensitive to the strain which changes the separation between islands or particles, and the gauge factor diverges^{2,3}. For example, 3 nm gold film with specific resistance as high as 25 k Ω / \square shows a gauge factor of 24 to 48⁴.

Piezoresistance effect was discovered in semiconductor materials such as silicon and germanium in 1954 by Charles S. Smith⁵. The gauge factor of semiconductor material is usually orders of magnitude higher than that of metallic material. Apparently, the second term in (2.3) is dominant in this case. In simple explanation, this large gauge factor in semiconductor materials arises from the modulation of band structures, the redistribution of carriers in conducting valleys, and the subsequent change of carrier mobility and effective mass as the material is under mechanical stress and strain⁶. As with other electrical properties of a semiconductor, the gauge factor depends strongly on the doping type (n- or p-type) and doping concentration. Because of the crystalline structure of semiconductors, the piezoresistive coefficients of semiconductors have to be described as a tensor, in a way similar to the modulus of elasticity tensor. To define the tensor of piezoresistive coefficients, we start from Ohm's law:

$$E = \rho \cdot j = \left(1 + \frac{d\rho}{\rho}\right) \cdot \rho_0 j \quad (2.4)$$

where the conductor is under strain and resistivity ρ changes by $d\rho$. Then, Ohm's law needs to be written in vector form to incorporate the strain tensor:

$$\frac{1}{\rho_0} \begin{bmatrix} E_1 \\ E_2 \\ E_3 \end{bmatrix} = \begin{bmatrix} j_1 \\ j_2 \\ j_3 \end{bmatrix} + \begin{bmatrix} d_{11} & d_{12} & d_{13} \\ d_{21} & d_{22} & d_{23} \\ d_{31} & d_{32} & d_{33} \end{bmatrix} \begin{bmatrix} j_1 \\ j_2 \\ j_3 \end{bmatrix}. \quad (2.5)$$

In cubic crystalline, (2.5) can be simplified using symmetry to:

$$\frac{1}{\rho_0} \begin{bmatrix} E_1 \\ E_2 \\ E_3 \end{bmatrix} = \begin{bmatrix} j_1 \\ j_2 \\ j_3 \end{bmatrix} + \begin{bmatrix} d_1 & d_6 & d_5 \\ d_6 & d_2 & d_4 \\ d_5 & d_4 & d_3 \end{bmatrix} \begin{bmatrix} j_1 \\ j_2 \\ j_3 \end{bmatrix}. \quad (2.6)$$

The coefficient of d can be related to mechanical stress tensor with further simplification by the symmetry in cubic crystalline as:

$$\frac{d\rho}{\rho} = \begin{bmatrix} d_1 \\ d_2 \\ d_3 \\ d_4 \\ d_5 \\ d_6 \end{bmatrix} = \begin{bmatrix} \pi_{11} & \pi_{12} & \pi_{12} & 0 & 0 & 0 \\ \pi_{12} & \pi_{11} & \pi_{12} & 0 & 0 & 0 \\ \pi_{12} & \pi_{12} & \pi_{11} & 0 & 0 & 0 \\ 0 & 0 & 0 & \pi_{44} & 0 & 0 \\ 0 & 0 & 0 & 0 & \pi_{44} & 0 \\ 0 & 0 & 0 & 0 & 0 & \pi_{44} \end{bmatrix} \begin{bmatrix} \sigma_1 \\ \sigma_2 \\ \sigma_3 \\ \sigma_4 \\ \sigma_5 \\ \sigma_6 \end{bmatrix} = \pi \cdot \sigma. \quad (2.7)$$

Here tensor elements $\pi_{11}, \pi_{12}, \pi_{44}$ are called piezoresistive coefficients, and their values for p -type and n -type silicon and germanium are given in Table 2-2.

Table 2-2 Piezoresistive coefficients for n-type and p-type silicon and germanium⁷

	π_{11} (100 GPa)	π_{12} (100 GPa)	π_{44} (100 GPa)
n -Si (11.7 $\Omega \cdot \text{cm}$)	-102.2	53.4	-13.6
p -Si (7.87 $\Omega \cdot \text{cm}$)	6.6	-1.1	138.1
n -Ge (9.9 $\Omega \cdot \text{cm}$)	-4.7	-5.0	-137.9
p -Ge (15 $\Omega \cdot \text{cm}$)	-10.6	5.0	46.5

To compare with metal, the typical value of gauge factor for p -type doped single crystal silicon is in the range of 40–200, while n -type doped single crystal silicon has a relatively lower and negative value of gauge factor in the range of -20–-100. Polycrystalline silicon has a considerably lower gauge factor than single-crystal silicon, in the range of 10–30, and it is strongly dependent on structure of the film.

Giant piezoresistivity was reported recently on silicon nanowire, showing piezoresistance coefficient π_{11} as high as $-3.55 \times 10^{-8} \text{ Pa}^{-1}$ at $\langle 111 \rangle$ direction⁸, a factor of more than 30 higher than bulk silicon. This will correspond to a surprisingly high gauge factor, at the order of 3000–5000. Further comprehensive investigation is necessary to confirm and clarify this unexpectedly giant effect.

Piezoresistance effect in conducting materials has been widely used for sensing applications. The most commonly used is metal foil strain gauge. A variety of pure metals such as gold, chromium, silver, palladium, nickel, platinum, and alloys such as gold-nickel, nickel-chromium (Constantan), copper-nickel, and platinum-nickel, are used in commercial products. Although the gauge factors of metal films are two orders of magnitude lower than semiconductor films, metal film strain gauge still dominates the market. The reasons for this include low cost of fabrication, robustness, low temperature coefficient, and the capability of using flexible substrates such as polyimide and other polymeric materials. All of these enable much wider usages and applications for metal film strain gauge devices than for semiconductor gauges. However, semiconductor gauges are recently more often seen in applications requiring high precision and in cleaner environments, such as pressure transducers and other MEMS-based devices.

2.2 Rationale of using metallic piezoresistive detection on NEMS

To date, most self-sensing microcantilevers employ piezoresistive displacement transduction⁹⁻¹². A sensor patterned from piezoresistive material, a piezoresistor, affixed to moving parts of a mechanical device undergoes resistance change when the device is in motion and strain is induced in the sensor. With current biasing, such a piezoresistor converts the strain-induced resistance change into a measurable voltage. The integration of such displacement sensors with the mechanical elements eliminates the need for device alignment with an (otherwise) external readout, such as a laser. This brings immense simplification to instrument design. Even more important, however, is that, by circumventing optics, piezoresistive transduction yields access to dimensions far below the diffraction limit, where the substantial advantages of nanoscale sensors are available. However several important issues must be addressed to make this possible.

Previous efforts to optimize piezoresistive sensors have largely focused upon the use of doped semiconducting materials, since they can provide a very large gauge factor γ . It is widely assumed that optimal transducer performance is obtained simply by using materials offering maximal γ , for it provides the largest absolute signal level. However, this assumption becomes profoundly incorrect for nanoscale sensors.

The commonly held assumption is that a large gauge factor will serve to maximize a displacement sensor's performance, but this is actually only one element in

optimizing its transduction efficiency. There are three generic attributes of high- γ materials that are always *deleterious* to high sensitivity displacement transduction. The first is that high γ is generally achieved only with high resistivity materials and, hence, large two-terminal resistances are quickly attained when the size of a piezoresistive transducer patterned from such materials is scaled down to nanometer dimensions. This can make noise matching between nanoscale piezoresistors and readout circuitry extremely difficult to impossible, especially at high frequencies. In fact, below a particular size range set by the carrier depletion length, surface states in semiconducting transducers can render them susceptible to freeze-out at reduced temperatures, or in the worst case, non-conducting even at room temperature. A second issue, in fact related to the first, is that high γ is typically associated with very low carrier densities and, hence, often with highly disordered or percolative conduction. When such a piezoresistor is scaled downward in size its resistance increase is accompanied by a very large increase in low frequency 1/f noise, as described by Hooge's relation¹³, $S_R^{(1/f)} = 2\pi\zeta R^2 / (N\omega)$. This empirical relation describes how the spectral density of resistance fluctuations at angular frequency ω grows when the number of carriers becomes small. Here N is the number of carriers within the sample of resistance R , and ζ is a sample-specific materials parameter (for p+ Si, $\zeta \sim 10^{-5}$)¹⁴. Finally, a third deleterious attribute of high- γ materials is their large temperature coefficients. These, too, originate from the low carrier density in the semiconducting (compared to metallic) regime, and the thermally activated, defect-mediated transport that is involved.

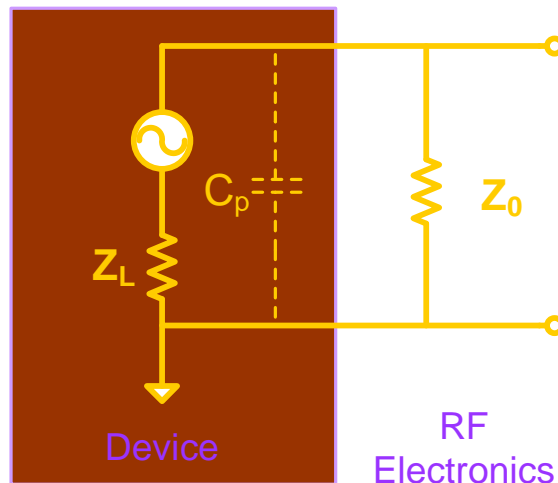


Figure 2-2 Impedance matching from high-impedance nanoscale devices to radio frequency electronics

These issues become more problematic for nanoscale piezoresistors. We find they may be circumvented, thereby enabling the immense advantages of self-sensing detection in the nanoscale regime, by replacing the conventionally employed semiconducting piezoresistive layer with a thin metal film. The underlying rationale for this replacement elucidates the true figure of merit for piezoresistive displacement transduction. It is not solely the gauge factor, but the *output (voltage domain) signal-to-noise ratio* (SNR), which also takes into account the coupling efficiency attained between the displacement transducer and its subsequent readout electronics. Specifically, for a nanoscale device, the loss of a factor of ~ 20 in γ that results upon transitioning from a semiconducting to a metallic transducer, is amply compensated by a profound reduction in the resistance of the latter, which can be a factor of $\sim 10^4$ or more. The latter arises directly from the huge disparity between the carrier density in thin metal films (on the

order of 10^{22} cm^{-3}) compared to that of doped semiconductor layers (on the order of 10^{18} cm^{-3} in the case of heavily doped semiconductors).

Use of metallic-density elements immensely simplifies impedance matching between the transducer and its subsequent readout, whose quality we characterize by the transmission coefficient, $1 - \Gamma(Z_L, Z_0)$ at their juncture. Here, $\Gamma = (Z_L - Z_0)/(Z_L + Z_0)$ is the junction reflection coefficient and Z_L and Z_0 are the impedances of the transducer output and the readout input. Typically, Z_0 is 50Ω for a low-noise, high frequency amplifier. As depicted in Figure 2-2, invariably, for high-impedance semiconducting devices of nanoscale dimensions $Z_L \gg Z_0$; consequently $\Gamma \sim 1$ and most of the signal is lost by reflection at readout's input. With nanoscale, metallic-density transducers we can engineer $Z_L \sim Z_0$, so that the transduced signal is optimally transmitted ($\Gamma \ll 1$). Further, low transducer output impedances provide greatly reduced susceptibility to signal degradation from the inevitable parasitic reactances, which otherwise will severely limit the accessible readout bandwidth of the circuit. For example, typically seen parasitic capacitance from the cabling and wiring of a readout circuit can be on the order of picofarad — with device impedance of $1 \text{ M}\Omega$, the cut-off frequency given by $1/2\pi RC$ will be less than 1 MHz . Signal above this frequency will be attenuated and accessible signal to noise ratio drops.

Further, metallic materials permit immense simplification of fabrication given their ease of deposition and patterning at the micro- and nanoscale. They can be deposited on a wide range of different substrates, including flexible polymeric materials

which cannot sustain the semiconductor process, which requires high processing temperature (deposition, doping, activation *etc.*). Their conductivity is robust against a wide range of chemical and plasma-based process conditions—in stark contrast to the well-known susceptibility of ultrathin low-density semiconducting layers to such processes.

2.3 Cantilever design

The most employed design of piezoresistive NEMS devices described in this thesis is cantilever. These piezoresistive cantilevers are designed with Π shape as depicted in Figure 2-3. The design of two “legs” on the cantilevers has two purposes: First, coated with metallic thin film, the legs form a conduction path for the piezoresistance measurement of the device. Secondly, when the cantilever devices displace, most of the mechanical strain will be concentrated at the leg area, thus providing improved piezoresistive transduction efficiency. This is justified by the finite elements simulation¹⁵ result in Figure 2-3, indicating the leg area has highest strain energy density.

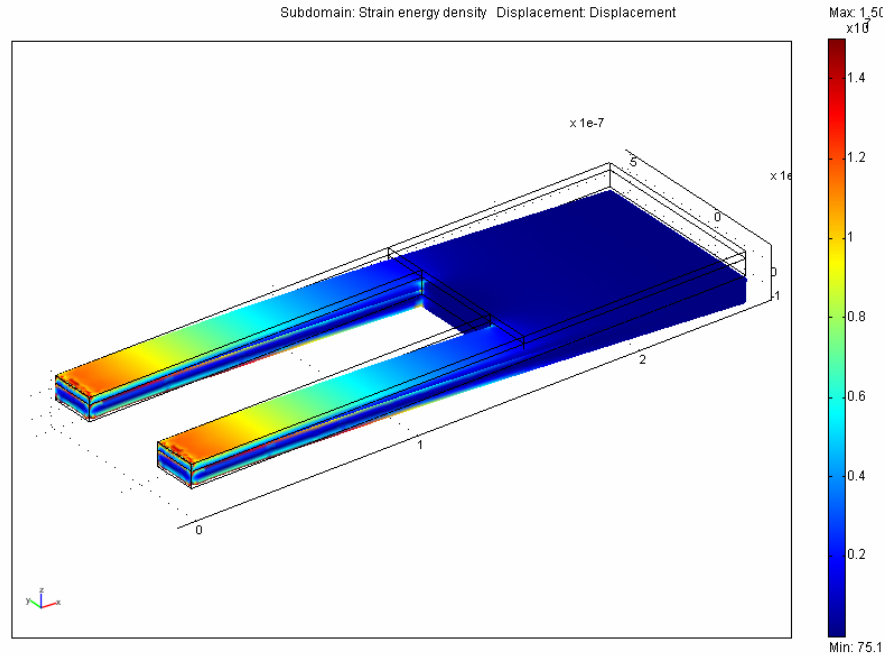


Figure 2-3 Finite elements simulation¹⁵ of a Π shape cantilever under deformation. The colorization shows the strain energy density, indicating the concentration at the leg area.

When designing a cantilever with predetermined force constant and fundamental mode resonance frequency, the following analytical equations derived from classical beam theory are used in the calculation¹⁶. The results are further confirmed by finite element simulation. Excellent agreement between two methods is usually obtained. In the equations, l , b and t are the total length, width, and thickness of the cantilever; l_1 and w are the length and width of each leg.

The force constant, effective mass, and resonance frequency are given in equations (2.8), (2.9), and (2.10) respectively:

$$k = \frac{E_{eff} t^3}{\frac{4l^3}{w} + (2l_1^3 - 6ll_1^2 + 6l^2l_1)\left(\frac{1}{b} - \frac{2}{w}\right)} \quad (2.8)$$

$$m_{eff} = \frac{\rho_{eff} t l^7}{w \left[\frac{4l^3}{w} + (2l_1^3 - 6ll_1^2 + 6l^2l_1)\left(\frac{1}{b} - \frac{2}{w}\right) \right]^2} \times \left\{ \begin{aligned} &72\left(\frac{w}{b}\right)\left[\frac{1}{20}\left(\frac{l_1}{l}\right)^5 + \frac{1}{252}\left(\frac{l_1}{l}\right)^7 - \frac{1}{36}\left(\frac{l_1}{l}\right)^6\right] + \\ &144\left[\frac{11}{420} + \frac{1}{12}\left(\frac{l_1}{l} - \frac{1}{2}\frac{l_1}{l}\right)^2\left(\frac{w}{b} - 2\right)^2 + \right. \\ &\left. \frac{1}{144}\left[2\left(\frac{l_1}{l}\right)^3 - 3\left(\frac{l_1}{l}\right)^2\right]\left(\frac{w}{b} - 2\right)^2 - \frac{1}{20}\left(\frac{l_1}{l}\right)^5 - \frac{1}{252}\left(\frac{l_1}{l}\right)^7 + \frac{1}{36}\left(\frac{l_1}{l}\right)^6\right] \end{aligned} \right\} \quad (2.9)$$

$$\omega = \sqrt{\frac{k}{m_{eff}}} \quad (2.10)$$

Since the cantilevers are coated with metal film, the effective density and Young's modulus of the bi-layer structure have to be used in the calculation¹⁶. They are given by equation (2.11) and (2.12):

$$\rho_{eff} = \frac{\rho_1 t_1 + \rho_2 t_2}{t_1 + t_2} \quad (2.11)$$

$$E_{eff} = \frac{t_2^3}{(t_1 + t_2)^3} \frac{t_1 E_1 E_2}{t_1 E_1 + t_2 E_2} \left[4 + 6\frac{t_1}{t_2} + 4\left(\frac{t_1}{t_2}\right)^2 + \frac{E_1}{E_2}\left(\frac{t_1}{t_2}\right)^3 + \frac{E_2 t_2}{E_1 t_1} \right]. \quad (2.12)$$

Here respectively t_1 and t_2 , ρ_1 and ρ_2 , E_1 and E_2 are the thickness, density, and Young's modulus of each layer of materials.

Typical properties of the materials, the design parameter of the cantilevers, and the results of calculation and simulation are listed in following tables, showing excellent consistency.

Table 2-3 Properties of gold and silicon carbide

Material	Young's modulus (GPa)	Density(g/cm ³)	Thickness (nm)
Au	78	19.32	30
3C-SiC	440	3.166	70

Table 2-4 Geometrical parameters of typical cantilevers

Cantilever	l (μm)	w (μm)	l_1 (μm)	w_1 (μm)	t (μm)
a	33	5	3	0.3	0.1
b	10	2	5	0.5	0.1
c	2.7	0.8	1.5	0.2	0.1
d	0.7	0.4	0.5	0.1	0.1

Table 2-5 Calculated and finite elements simulate results of cantilever parameters

Cantilever	Measured frequency [Hz]	Calculated frequency [Hz]	FE simulation frequency [Hz]	Calculated spring constant from Eq. (1) [N/m]	FE simulation spring constant [N/m]
a	52 k	48 k	51.2 k	0.006	0.005
b	1.6 M	1.2 M	1.3 M	0.12	0.15
c	8 M	7.6 M	8.4 M	1.16	1.15
d	127 M	125 M	128.4 M	32.2	32.1

2.4 Fabrication of nanocantilevers

Nanocantilevers are fabricated with reactive plasma-etching-based surface micromachining techniques. The starting material is epitaxial 3C silicon carbide (3C-SiC) on silicon substrate, or PECVD grown silicon nitride (SiN) on silicon substrate. This layer of material forms the supporting mechanical structure of the cantilever. Silicon carbide and silicon nitride are selected for their excellent mechanical properties, easiness of fabrication, and robustness to chemical and physical etching processes.

We then define cantilever structure using electron beam lithography. Typically two layers of resist, 4% 495 K PMMA and 2% 950 K PMMA in anisole (Microchem, MA) are spin coated on the substrate at 4000 rpm and baked at 180 °C. After the exposure and development, 2–5 nm chromium and 30 nm gold films are thermally evaporated and lifted off in acetone. These metal layers serve as both a self-aligned mask in the subsequent etching process and as a piezoresistive transducer layer on the final device. Then the SiC (SiN) /metal cantilever is released from the substrate with electron cyclone etching (ECR) in two steps, using argon and nitrogen trifluoride (NF₃) plasma. In the first etching step, the chamber pressure is set at 20 mTorr and DC bias of –250 V is applied to the plasma. At this condition, the etching process is highly anisotropic, and the SiC or SiN layer is etched vertically toward the substrate. For 80 nm SiC and 100 nm SiN, the etching time is about 45 seconds and 20 seconds, respectively. In the second etching step, DC bias voltage is reduced to –100 V and the etching is thus changed to be more isotropic, in order to etch the silicon substrate. In this way, the cantilever structure is undercut and eventually released from the silicon substrate. The etching selectivity

between silicon and SiC (estimated to be larger than 70) is much larger than that between silicon and SiN (less than 10). So SiN is less tolerant to the over-etching in the second isotropic etching than SiC, and accurate timing is very important. Figure 2-4 illustrates the etching process.

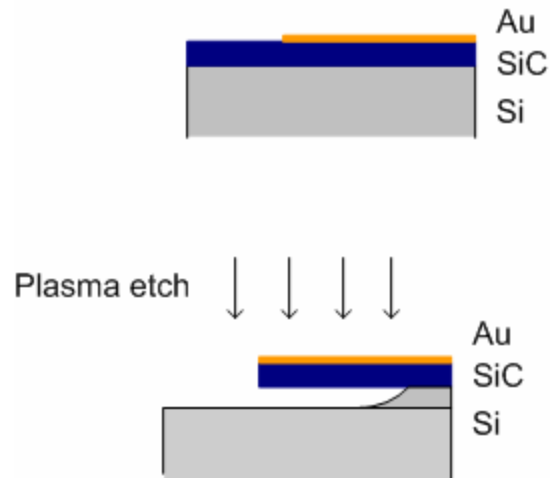


Figure 2-4 Fabrication process flow

In Figure 2-5, scanning electron microscope images of four typical devices made of silicon carbide and gold are shown. Their lengths vary from 30 μm to 600 nm. The geometry of the cantilever, especially the length and the width of the legs, is designed with consideration of both wanted resonance frequency and low two-terminal resistance. Completed devices have typical resistance below 100 Ohm. Their resonance frequencies and force constants are listed in Table 2-5. The excellent etching selectivity of silicon carbide to silicon can be clearly seen from the picture. For instance, in fabricating the large cantilever (Figure 2-5a), the silicon substrate is undercut by more than 5 μm to release the cantilever, while the 300 nm wide legs still remain, with negligible etching.

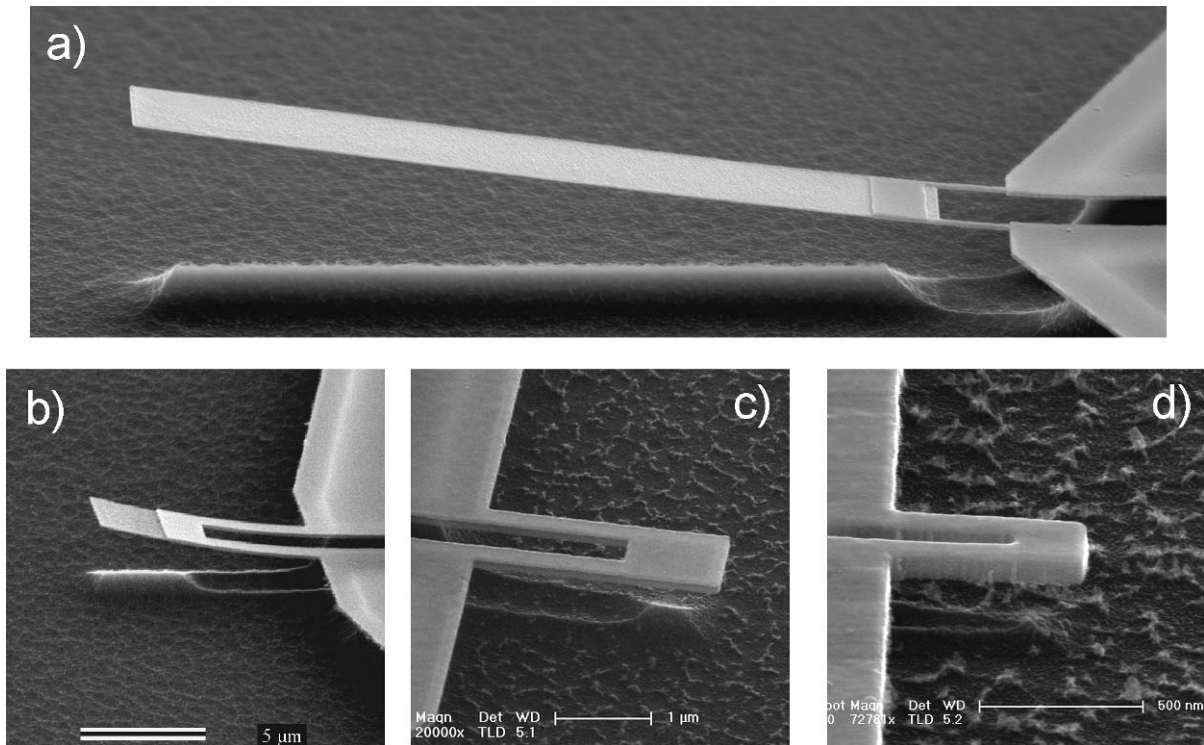


Figure 2-5 SEM images of cantilevers made of 100 nm thick SiC and with 30 nm gold film. Their dimensions are: a) $33\ \mu\text{m} \times 5\ \mu\text{m}$; b) $10\ \mu\text{m} \times 2\ \mu\text{m}$; c) $2.5\ \mu\text{m} \times 0.8\ \mu\text{m}$; d) $0.6\ \mu\text{m} \times 0.4\ \mu\text{m}$

Structures other than cantilevers are also fabricated in a similar way, such as a doubly clamped beam shown in Figure 2-6, and a trampoline resonator with integrated heater and piezoresistive transducer shown in Figure 2-7.

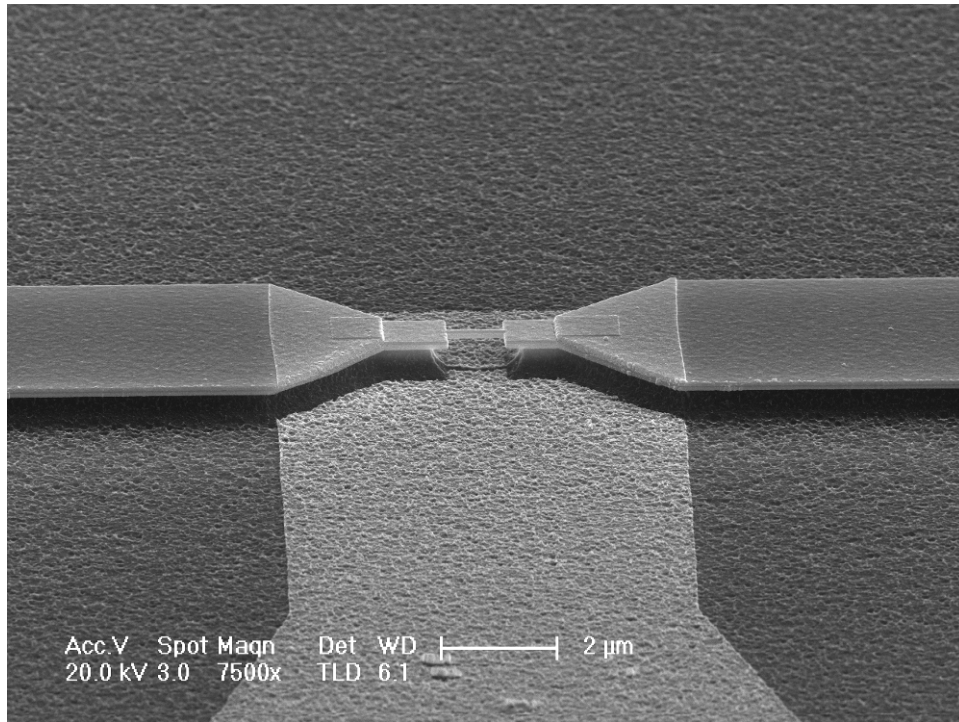


Figure 2-6 A doubly clamped beam with metalized bottom gate

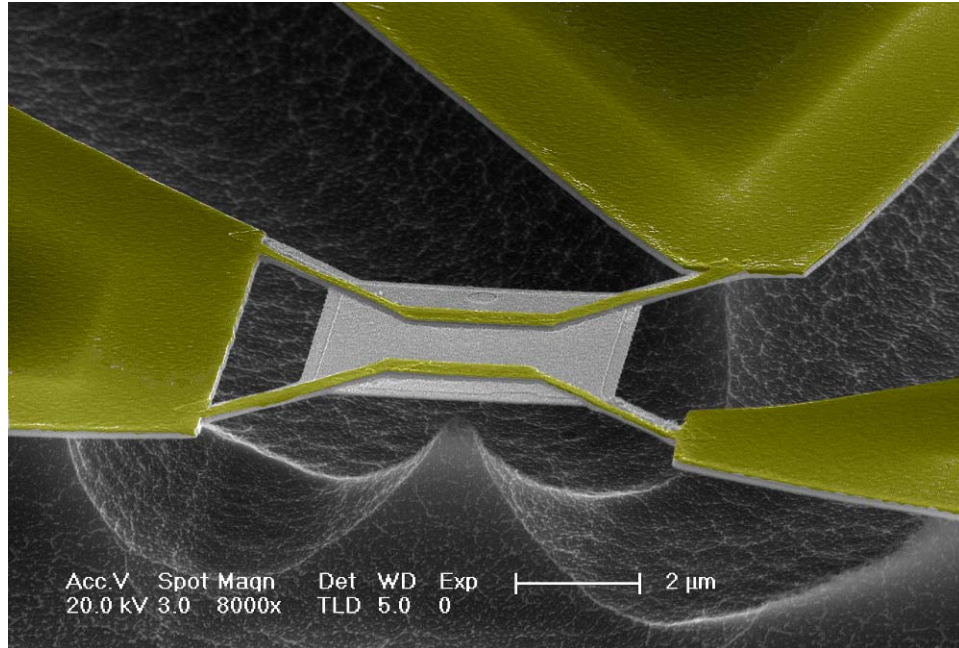


Figure 2-7 A trampoline resonator with integrated heater and piezoresistive transducer.

Gold layer is in yellow false color

2.5 Low frequency cantilevers

Low frequency cantilevers such as the one shown in Figure 2-5a have very low force constants in the range of mN/m to $\mu\text{N/m}$ (This cantilever has a force constant of 6 mN/m). As described in Chapter 3, this low force constant implies very high force sensitivity, which is optimal for detection of small forces.

Figure 2-8 to Figure 2-11 show the measured piezoresistive response of the cantilever in Figure 2-5a at its both fundamental resonance mode of 52 kHz and second resonance mode of 640 kHz, with varying actuation voltage, and bias voltage, respectively. The response of the piezoresistive transducer shows excellent linearity with both actuation and bias voltages, as expected for the metallic piezoresistivity. Resonance quality factor of this low frequency cantilever is around 500 in vacuum.

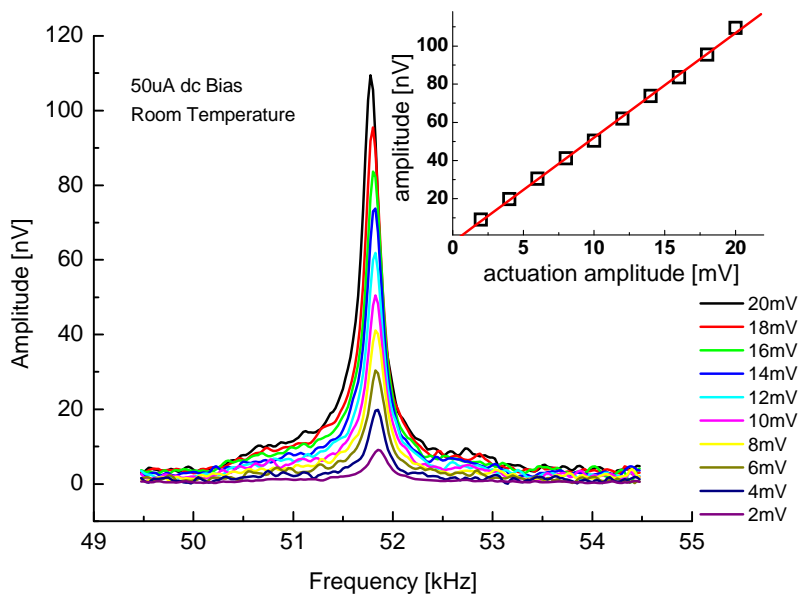


Figure 2-8 Fundamental mode resonance response of cantilever from Figure 2-5a at constant DC bias voltage and varying bias voltage. Inset: response amplitude versus actuation voltage amplitude

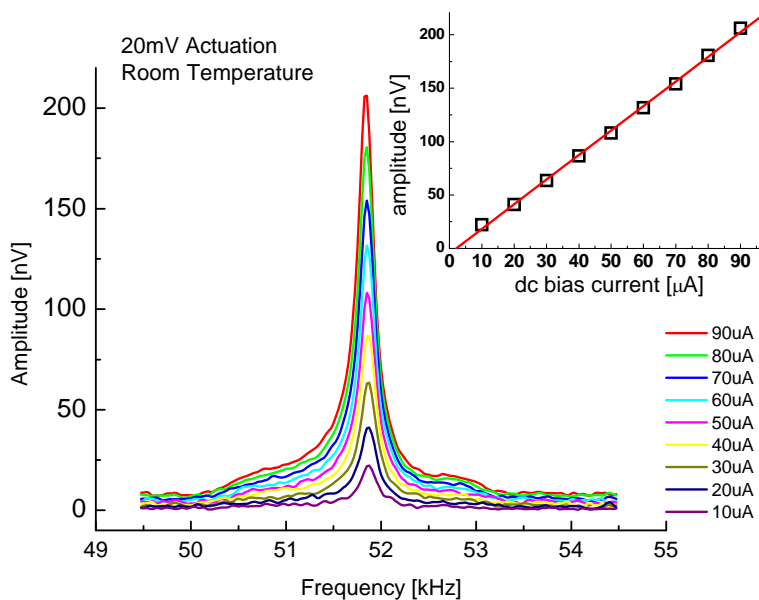


Figure 2-9 Fundamental mode resonance response of cantilever from Figure 2-5a at constant actuation voltage and varying bias voltage. Inset: response amplitude versus bias voltage amplitude

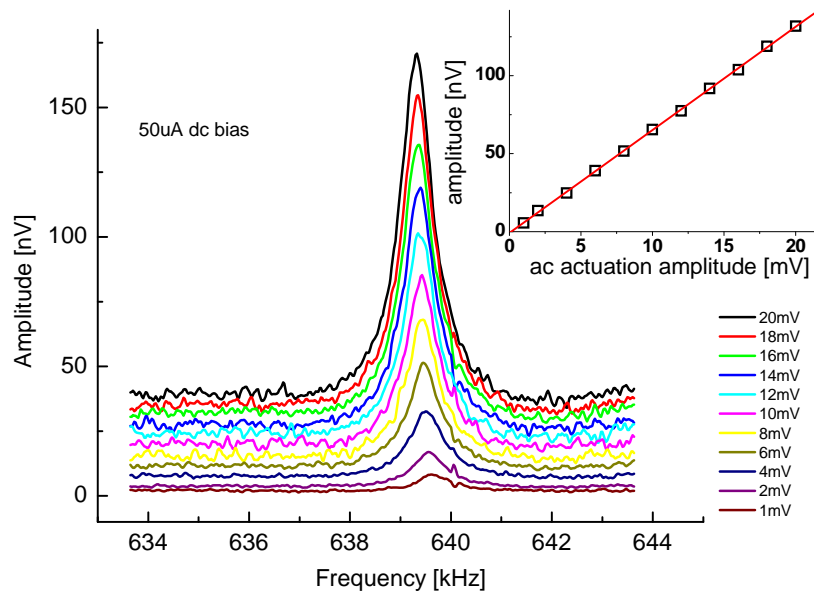


Figure 2-10 Second mode resonance response of cantilever from Figure 2-5a at constant bias voltage and varying actuation voltage. Inset: response amplitude versus actuation voltage amplitude

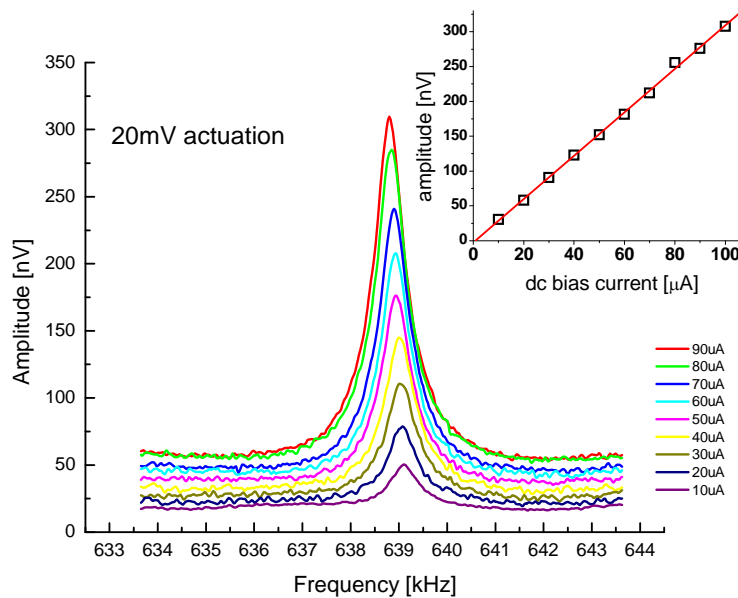


Figure 2-11 Second mode resonance response of cantilever from Figure 2-5a at constant actuation voltage and varying bias voltage. Inset: response amplitude versus bias voltage amplitude

Resonance responses of cantilever from Figure 2-5b are shown in Figure 2-12 and Figure 2-13. The second resonance mode has a frequency at about 15 MHz, into the high frequency (HF) band. Both insets show the linear response to varying actuation voltage. Also notable is that the cantilever from Figure 2-5b shows quality factor of 20 in atmospheric pressure, as shown with dotted lines in Figure 2-12.

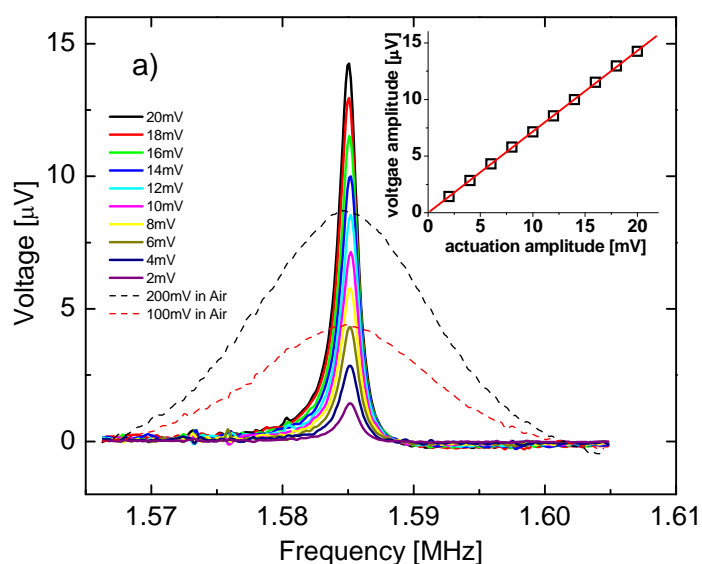


Figure 2-12 Fundamental mode resonance response of cantilever from Figure 2-5b at constant bias voltage and varying actuation voltage. Dotted lines show cantilever's resonance response in air. Inset: response amplitude versus actuation voltage amplitude

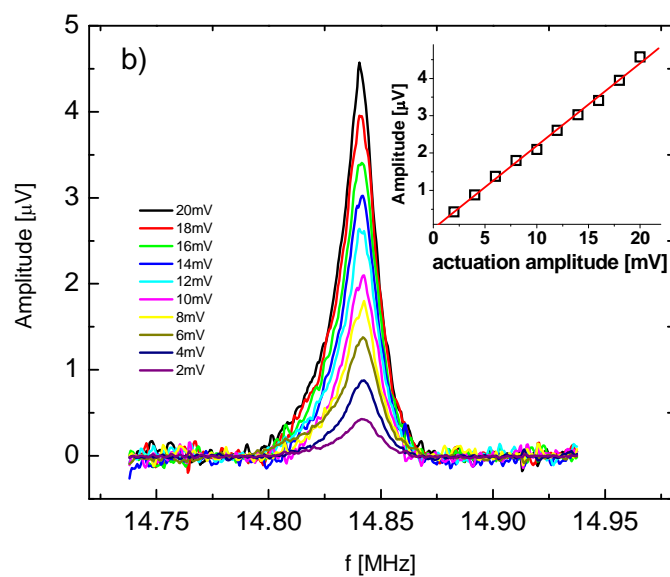


Figure 2-13 Second mode resonance response of cantilever b) at constant bias voltage and varying actuation voltage. Inset: response amplitude versus actuation voltage amplitude

2.6 HF/VHF cantilevers

Further miniaturization of cantilever dimension will increase its resonance frequency. Cantilevers such as the ones shown in Figure 2-5c and d have resonance frequency well into the high frequency (HF, 3–30 MHz) and very high frequency (VHF, 30–300 MHz) bands. The advantages of low impedance metallic piezoresistive transducers are manifested by the excellent responses and signal to noise ratios of the resonant motion detection. No extra impedance-matching circuitry between the device and pre-amplification stage are needed to readout the signal so that commercial 50 Ω input impedance low-noise RF amplifiers (MITEQ AU-1442) can be conveniently used. Details of direct resonance measurement of these HF cantilevers are described in Chapter 3.

Figure 2-14 shows the resonance response of the cantilever c in Figure 2-5 in vacuum with varying actuation voltages, plotted in decibel units. Measured thermomechanical noise spectrum is also shown as the black trace. Two resonance peaks are observed because the usage of the frequency down conversion measurement scheme which is also described in Chapter 3. This data demonstrates the remarkable linear dynamic range (DR) of these cantilevers, on the order of 80 dB as measured from the thermomechanical noise floor to the onset of nonlinearity. DR is an important figure-of-merit for nanomechanical resonators, as it determines the largest signal to noise ratio that can be achieved^{17,18}. Also, when measuring the shift of the device's resonance frequency, it is crucial in determining the minimum resolvable frequency shift¹⁷. Nonlinear response is observed at very high actuation amplitude, showing the resonance peak tilting toward

the lower frequency size¹⁹. This indicates the softening nonlinear behavior of the device, possibly due to the bi-layer structure of the device²⁰.

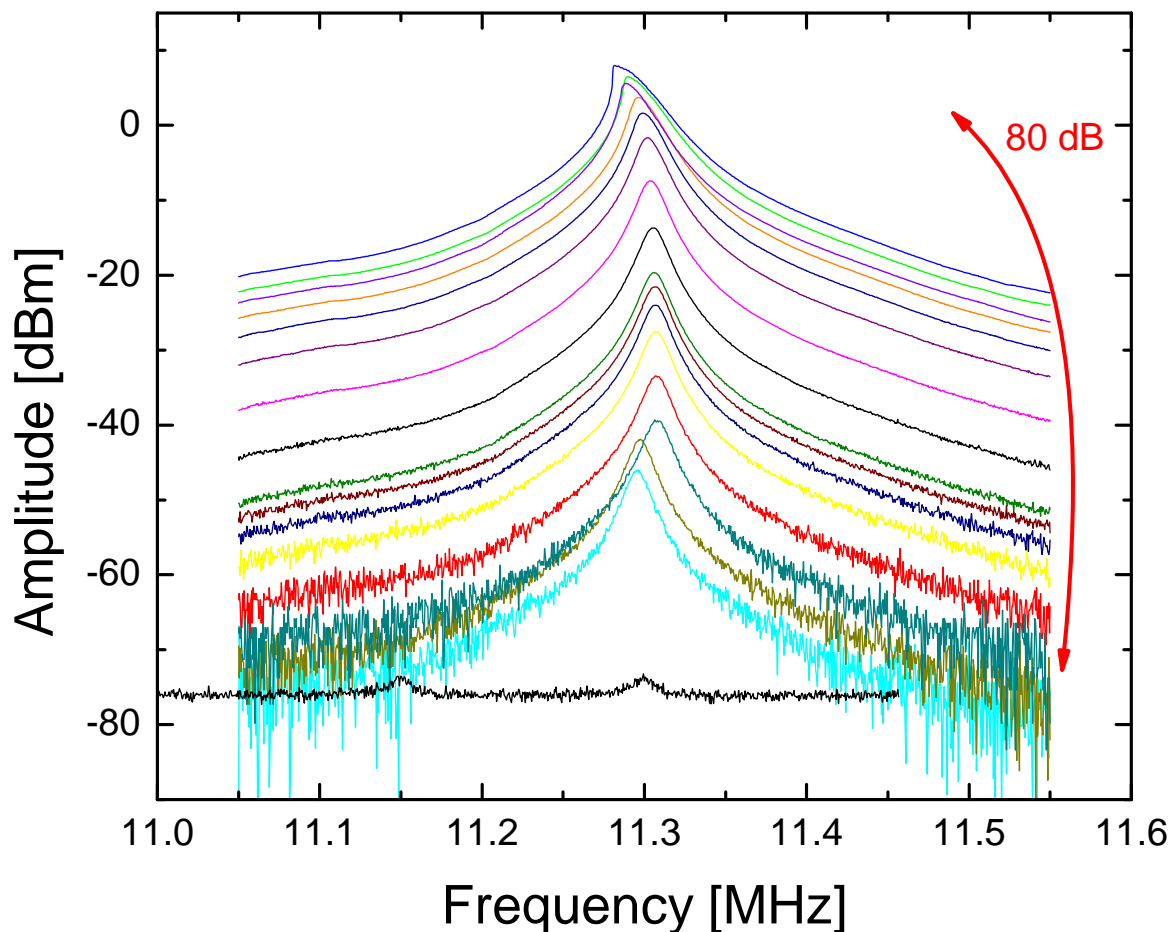


Figure 2-14 Fundamental mode resonance response of cantilever from Figure 2-5c at constant bias voltage and varying actuation voltage, plotted in log scale. Nonlinear response is observed with largest actuation. Black trace shows the thermomechanical noise spectrum of the same cantilever using the frequency down conversion scheme as described in Chapter 3. This data shows the excellent linear dynamic range (DR) of this cantilever, at the order of 80 dB measured from thermomechanical noise floor to the onset of nonlinearity.

The smallest cantilever of Figure 2-5d has a remarkably high resonance frequency at 127 MHz, the first ever achieved in VHF band. This device has a length of only 600 nm and width only 400 nm. Figure 2-15 shows its measured fundamental mode resonance response both in vacuum and at 1 ATM air. Very remarkably, a quality factor of 400, the highest among all cantilevers, is observed in air. This avoidance of vacuum requirement for operation makes these nanoscale cantilevers very promising for various applications at ambient conditions, such as gas sensing, which will be described in details in later chapters.

In terms of pushing the frequency limit of these cantilever devices, the highest frequency that has been demonstrated is more than 180 MHz. However, the detection bandwidth is not limited by metallic piezoresistive readout, but by the design of cantilevers. By designing doubly clamped beams or other structures, detection of nanomechanical motion at frequency higher than 1 GHz is possible. In fact, using the same readout method, high-order modes of a complicated device at frequencies as high as 1.094 GHz have been observed by others²¹. Another limitation on operation frequency here is the piezoelectric disk used to actuate. Even with the very high quality single crystal (PMN-PT, TRS Technologies Inc.), the achievable actuation amplitude tails off at above 100 MHz. An alternative high efficiency driving mechanism is necessary to expand the operation frequency beyond the VHF band up to UHF and microwave frequencies. One possible solution includes the integration of piezoelectric material such as AlN, GaN, or PZT onto the NEMS device. There are many challenges to accomplish with that, but it is certainly very worth exploring.

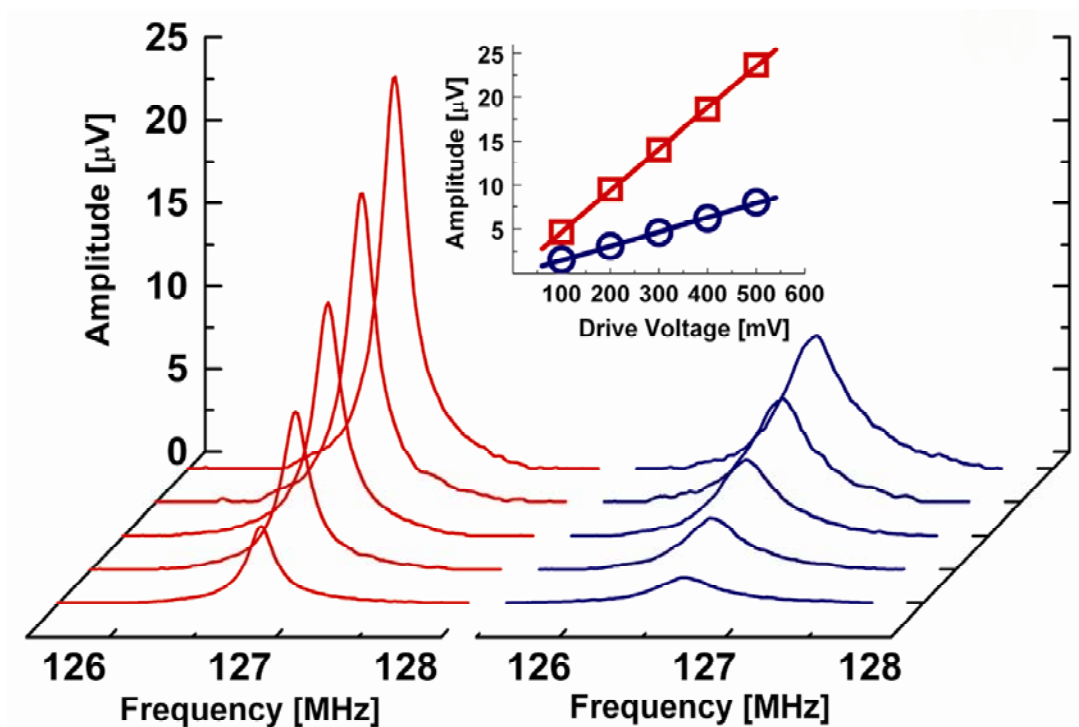


Figure 2-15 Fundamental resonance mode of cantilever from Figure 2-5d, both in vacuum (red) and at 1 atm (blue), with actuation voltage varying from 100 mV to 500 mV. The inset shows that resonance amplitude is linearly proportional to the actuation voltage.

2.7 Operation of high frequency nanocantilevers in ambient conditions

Quality factor Q is very crucial for the performance of a mechanical resonator. Fundamentally, quality factor characterizes the energy dissipation rate of the resonating system into the surrounding environment, and, as elucidated by fluctuation-dissipation theory, the noise induced by the environment to the system²². So far, the unprecedented sensitivity and resolution of NEMS devices, such as zeptogram-scale mass sensing, are only obtainable in a vacuum environment, which is required for NEMS resonators to retain a very high resonance quality factor. Both signal to noise ratio and accuracy of determining the resonance frequency of the NEMS resonators depend highly on high quality factor¹⁷. This vacuum requirement is becoming a major inconvenient constraint for wide application of NEMS, as most interesting sensing applications involving chemical and biological samples are only viable in ambient environments, namely at atmospheric pressure, or in liquid. Several methods to improve the quality factor of mechanical resonators in heavily damping environments have been proposed and implemented, including parametric amplification and active feedback control^{23,24}. However, successful demonstration of high Q at very high frequency in ambient conditions is still rare.

In Figure 2-15, a noteworthy attribute of a very high frequency nanocantilever is demonstrated. Even at atmospheric pressure, the quality factor of that cantilever still remains at 400, decreased by only a factor of 2 from its value (900) in vacuum. This is

unlike larger cantilevers, whose quality factors usually drop by a factor of more than 10, as shown in Table 2-6.

Table 2-6 Parameters of typical cantilever devices as shown in Figure 2-5

Cantilever	Dimension ($\mu\text{m} \times \mu\text{m} \times \mu\text{m}$)	Frequency	Force constant (N/m)	Q at .01 Torr (300K)	Q at 1 Atm (300K)
a	33 \times 5 \times 0.1	52 kHz	5×10^{-3}	500	15
b	10 \times 2 \times 0.1	1.6 MHz	0.15	950	20
c	2.7 \times 0.8 \times 0.1	8 MHz	1.15	1000	90
d	0.6 \times 0.4 \times 0.1	127 MHz	32.1	900	400

This prompted us to carefully study the quality factor dependence on ambient pressure of these cantilevers. Measured data is plotted in Figure 2-16. At low pressure, these three cantilevers (b, c, d in Figure 2-5 and Table 2-6) have similar Q values, at about 1000. As pressure increases, their Q values start to decrease. This initial decrease is due the damping caused by momentum exchange between the ambient gas molecules and the motional devices, and can be modeled using classical gas kinetic theory in free molecular flow regime. Equation (2.13) gives the Q expression corresponding to this damping mechanism for a simple “diving board” cantilever, showing an inverse proportion to ambient pressure P ²⁵. The total Q value is given by equation (2.14) — the total damping to the device is the sum of intrinsic damping and the damping from gas molecules. Here, ρ is the density of the material that the device is made of, d is the thickness of the device, f_0 is the resonance frequency, R_0 is molar gas constant, T is

absolute temperature, M_0 is the molar mass of the gas ($M_0=29$ g/mol for air), and P is pressure.

$$Q_m = \left(\frac{\pi}{2}\right)^{\frac{3}{2}} \rho d f_0 \frac{\sqrt{R_0 T / M_0}}{P} \quad (2.13)$$

$$\frac{1}{Q} = \frac{1}{Q_i} + \frac{1}{Q_m} \quad (2.14)$$

In Figure 2-16, measured data is fitted with equation (2.13) and (2.14). Deviation of the data points from the fitting function happens at higher pressure, indicating the breakdown of the free molecular flow modeling. It is also noticeable that the smaller the cantilever, the higher pressure this deviation starts at. This is due to the size dependence of fluid dynamics modeling regimes of devices with various dimensions. Generally, smaller devices tend to have larger quality factor than larger devices at high pressure, even though their intrinsic Q may not be higher.

Intrinsic quality factor as high as 100,000 has been observed on optimally designed NEMS devices²⁶. The relatively low Q value observed on these cantilever devices is possibly due to the dominance of dissipation by the internal friction inside the metal layer on the device²⁷. Since much higher Q value is observed on devices without metallization²⁸, other intrinsic mechanisms — such as thermoelastic and surface states damping — contribute only a little dissipation. To improve the Q of metalized devices, optimized deposition methods and annealing processes need to be developed.

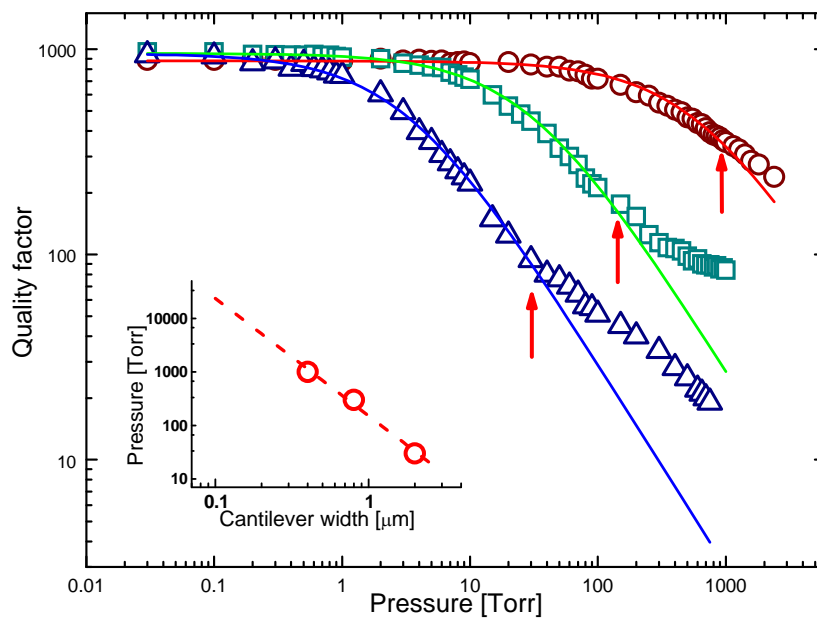


Figure 2-16 Resonance quality factor for cantilever from Figure 2-5b, c and d when operated in air at various pressures. Q factors at 1 Atm are 20, 90, and 400, respectively. The measured cantilever Q s (symbols) deviate from predictions based upon molecular flow (solid lines) at the crossover into the viscous flow regime (red arrows). This occurs at 30, 300, and 1000 torr, for the 2 μm , 800 nm, and 400 nm wide cantilevers, respectively. Inset: The relation between the pressure at crossover and cantilever width

Fluid dynamic modeling of the mechanical devices can be divided into three different regimes, which can be demarcated by a dimensionless number — the *Knudsen* number²⁹. Knudsen number is defined as the ratio of mean free path of the ambient gas l_{mfp} to the characteristic dimension of the device structure. In the case of flexural mode of cantilever devices, this characteristic dimension is the width w of the cantilever. At high Knudsen number regime ($K_n > 10$) with low pressure such that the mean free path of gas is much larger than the width of the cantilevers, it is in the free molecular flow regime. At

low Knudsen number ($K_n < 0.01$) with high pressure, the air flow is in a continuum regime. A cross-over or Knudsen flow regime exists in between $0.01 < K_n < 10$.

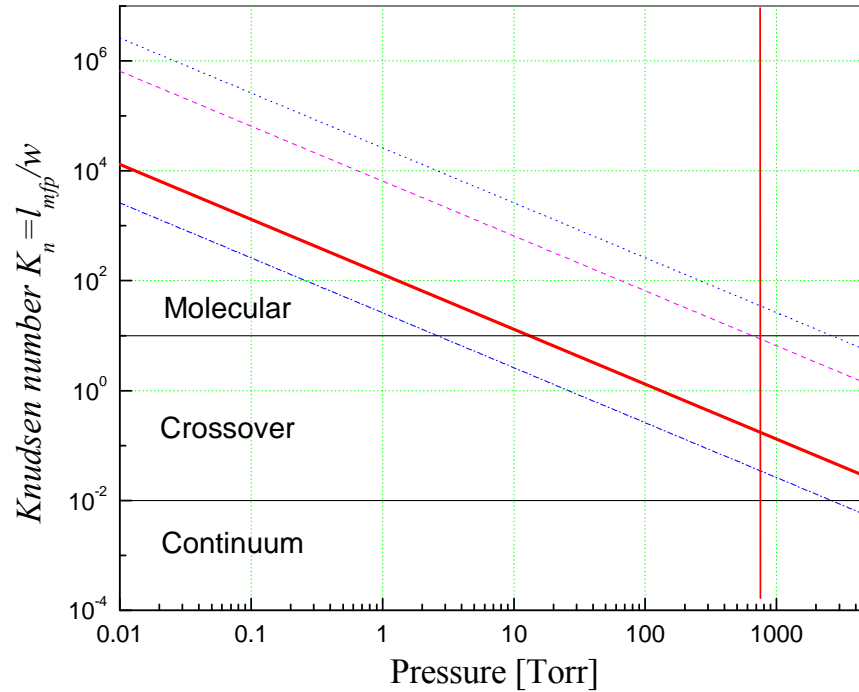


Figure 2-17 Knudsen number and air flow regime at varying pressure, for cantilever beams with different width (2 μm , 400 nm, 8 nm, and 2 nm respectively)

In Figure 2-17, the Knudsen number for cantilever beams with different widths is plotted against air pressure. What's noteworthy is that for nanoscale cantilever beams, the continuum flow limit can break down even at atmosphere pressure where the mean free path of air is about 65 nm. For example, a beam with width of only 2 nm, such as a single wall nanotube, is still in free molecular flow regime at atmospheric pressure. It can be clearly seen in Figure 2-17 that for the smallest cantilever with width of 400 nm, it is in the cross-over flow regime at atmospheric pressure. The data in Figure 2-16 shows the Q

value of the smallest cantilever drops substantially slower than larger cantilevers, for it remains in the cross-over regime (or Knudsen flow) at high pressure. In continuous flow regime, the viscous damping of air dominates and generally induces faster drop of the Q value as pressure increases, as indicated by modeling. Detailed analysis of the damping mechanisms and device design rationale to optimize the quality factor is beyond this work's scope and can be found in the literature³⁰. Cross-over regime or Knudsen flow is difficult to characterize analytically, but efforts have been made to approximate the problem for nanoscale oscillating beams²⁹. A straightforward conclusion is that nanoscale mechanical devices tend to sustain high quality factors at high pressure, which enables them to be operational with the same measurement accuracy and resolution as is achievable by larger devices in vacuum conditions.

Quality factor and pressure dependence in different gases are also measured with a nanocantilever having resonance frequency at 77 MHz. Nitrogen, helium, and tetrafluoroethane ($C_2H_2F_4$, hereafter TFE) are tested, and the quality factor and pressure dependence is measured with different gases. Clearly, in heavier gases (such as TEF), the quality factor of the cantilever drops faster with increasing pressure than it does in lighter gases (such as helium), as indicated by equation (2.13). Their difference in viscosity must also be considered to account for different viscous damping. These results demonstrate the advantages of using hydrogen as the ambient gas for nanomechanical resonators (for its lower molar mass and lower viscosity). In fact, as described in Chapter 4, for chemical gas sensing in a gas chromatography system, hydrogen is commonly used as a carrier gas

because it provides the best separation speed. In a hydrogen environment, nanocantilevers show the best quality factor at atmospheric pressure.

Table 2-7 Properties of different ambient gases

Gas	Molar mass	Density at standard conditions (g/l)	Absolute viscosity (10^{-6} Pa s)	Kinematic viscosity (10^{-6} m ² /s)
hydrogen	2	0.089	8.76	98.43
helium	4	0.179	18.6	103.9
nitrogen	28	1.25	17.81	14.25
TFE	102	4.55	unknown	unknown

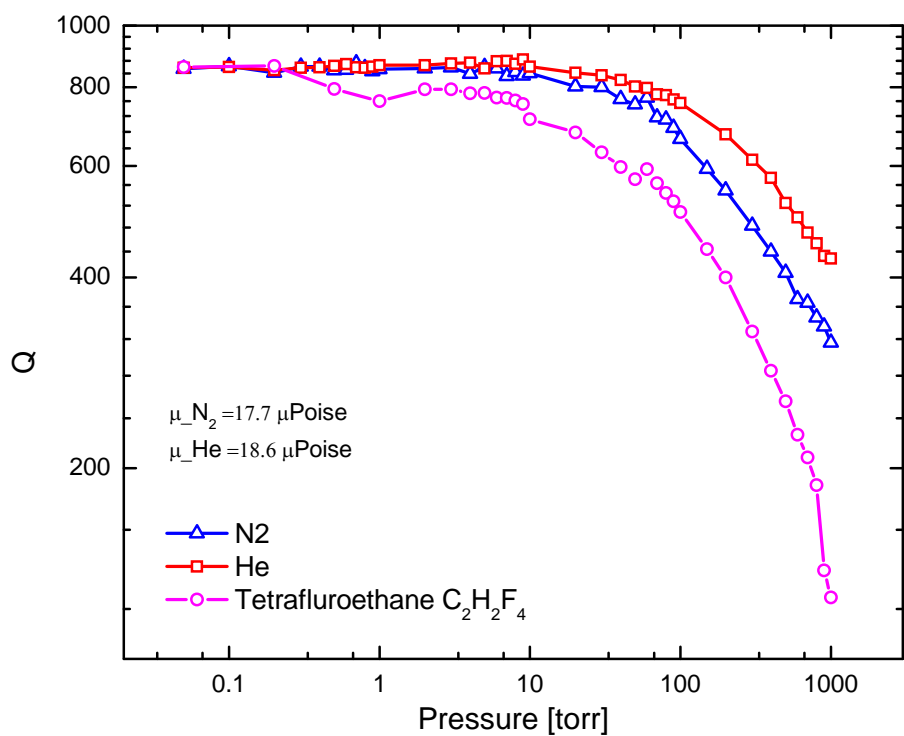


Figure 2-18 Quality factor and pressure dependence of nanocantilever in different ambient gases

2.8 Piezoresistive microcantilevers for AFM

In 1993, Tortonese et. al.⁹ first demonstrated using doped silicon piezoresistive microcantilevers for atomic force microscopy (AFM). Atomic resolution was achieved with their system. However, options for further improvement and wide usage of this type of self-sensing cantilever are limited. Probable reasons for that include the high cost and complex process of making those cantilevers, the high temperature coefficients of the piezoresistive transducer, and most importantly, their limited resolution.

The success of making metallic piezoresistive cantilevers and their excellent performance inspired us to use them for AFM applications. As demonstrated, these cantilevers are fairly easy to fabricate, only requiring one more step of metallization. To demonstrate, commercial AFM microcantilevers (μ Mash®, 15 series silicon cantilever, typical resonance frequency 325 kHz, force constant 40 N/m) are used, and Cr/Au film is evaporated onto one side of them. Focused ion beam was used to cut an opening on the cantilevers to define a similar two-leg structure as in previous micro-machined piezoresistive cantilevers. In Figure 2-19, an image of the microcantilever after the processing is shown, and their resonance responses measured by piezoresistive detection both in vacuum and in air are shown in Figure 2-20. The resonance frequency is lowered from the original value after the process because of the cutting and mass loading of the gold film. We hereafter can use these cantilevers for AFM in tapping mode. Frequency down mixing method is used to reduce the capacitively coupled background signal, and detected amplitude and phase of the resonance signal is shown in Figure 2-21. Details of this technique are covered in Chapter 3.

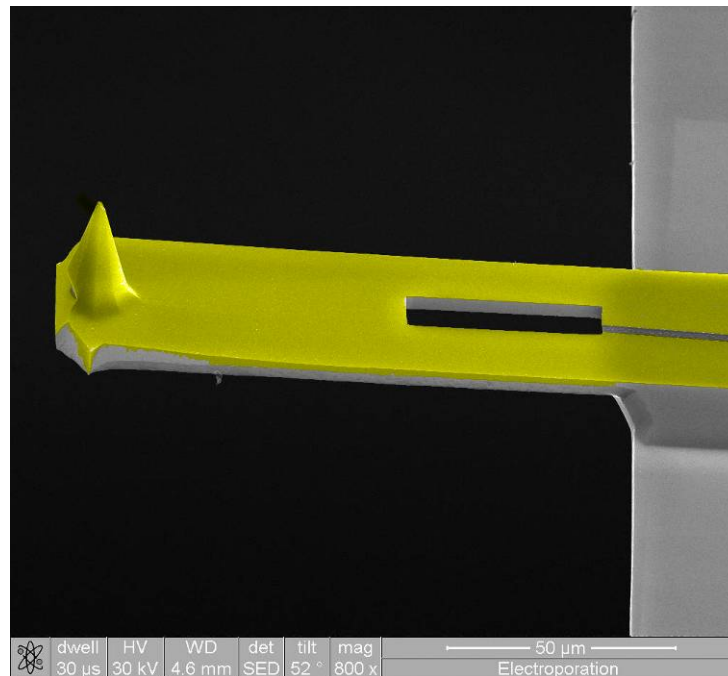


Figure 2-19 Commercial AFM microcantilever coated with gold film and processed with focused ion beam for piezoresistive detection

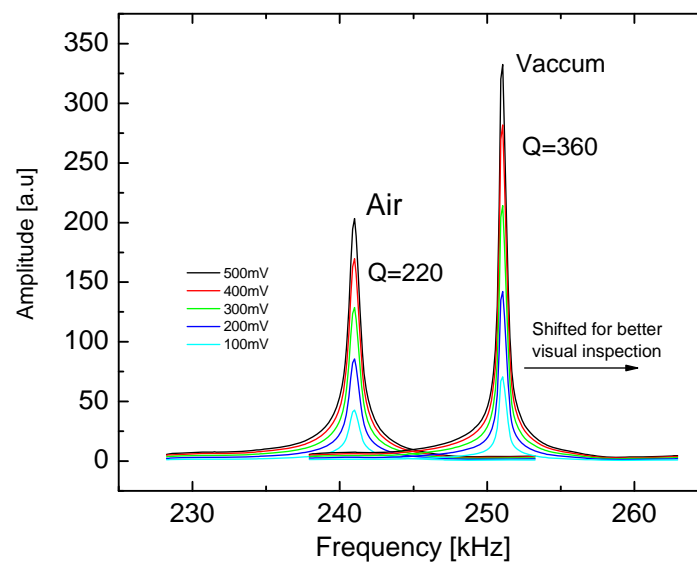


Figure 2-20 Piezoresistively detected resonance of commercial microcantilevers in air and vacuum with varying actuation voltage

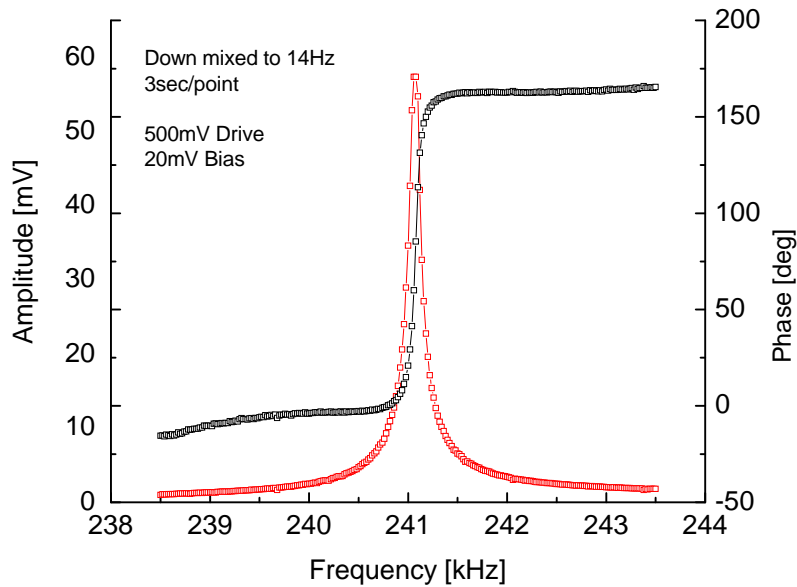


Figure 2-21 Frequency down mixing method detected resonance of commercial microcantilever. Very low background signal can be obtained

Digital instruments 3100 AFM was used to test these modified microcantilevers. The AFM probe head was also modified to connect the piezoresistor on the microcantilever to an external pre-amplifier and lock-in amplifier. Signal access modulus (SAM) was used to send the external driving signal to the piezoelectric actuator on the probe head, and to reroute the piezoresistive readout signal output from the lock-in amplifier's auxiliary output port to the AFM controller and computer. Since the phase signal channel from the extender electronics module to the controller is used, the piezoresistive signal was recognized by the controller and computer as a phase signal. Figure 2-22 shows the modified probe head and electronics used to measure the piezoresistive signal from the cantilever.

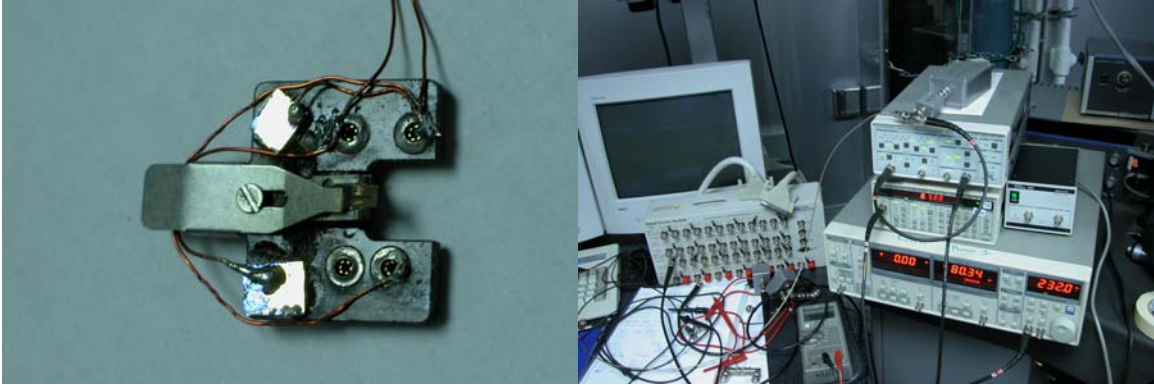


Figure 2-22 Modified AFM probe head and electrical setup to measure piezoresistive AFM signal

At tapping mode, the cantilever is driven at its resonance and its amplitude is read by the photodiode detector via optical level setup. A feedback loop is used to keep this amplitude constant and to move the height of the cantilever by a piezoelectric tube element so that the cantilever tip is kept at a fixed distance above the local topographical height of the sample surface. Thus this height adjustment feedback control signal is proportional to the sample surface height relative to a reference plane, and is read by the AFM controller as a height signal. However, in this mode, the cantilever is maintained at constant oscillation amplitude so that the piezoresistive resonance signal will have no change in response to the sample surface topography. The constant height feedback loop has to be stopped to allow the change of cantilever tip and sample distance, and consequently the cantilever oscillation amplitude. In this way, we can read the piezoresistive resonance signal to reveal the height of the sample surface, because the amplitude and frequency of the oscillating cantilever is affected by the tip-surface distance, due to the van der Waals force between them. DI AFM system provides a very convenient operation mode called “interleave” scan mode, designed for applications such

as magnetic force microscopy (MFM) and electric force microscopy (EFM). Briefly, in this mode, each scan line is scanned twice by the cantilever tip. In the first scan, the constant height feedback is on and the height profile of the trace is recorded. A mean height value of the sample surface in this trace is then calculated and used to lift the cantilever to a constant height above the mean value, large enough to avoid the tip touching the surface. In the second scan of the same line, feedback control is turned off and the signal from the second channel is recorded. Often it records the magnetic or electrical force between the sample and cantilever, but in our case, piezoresistive resonance signal is recorded. So by using this interleave mode, two images of the sample are acquired: one from the height signal and one from the piezoresistive resonance signal which should record the same surface height topography of the sample. A diagram of our modified signal configuration using the signal access module is shown in Figure 2-23.

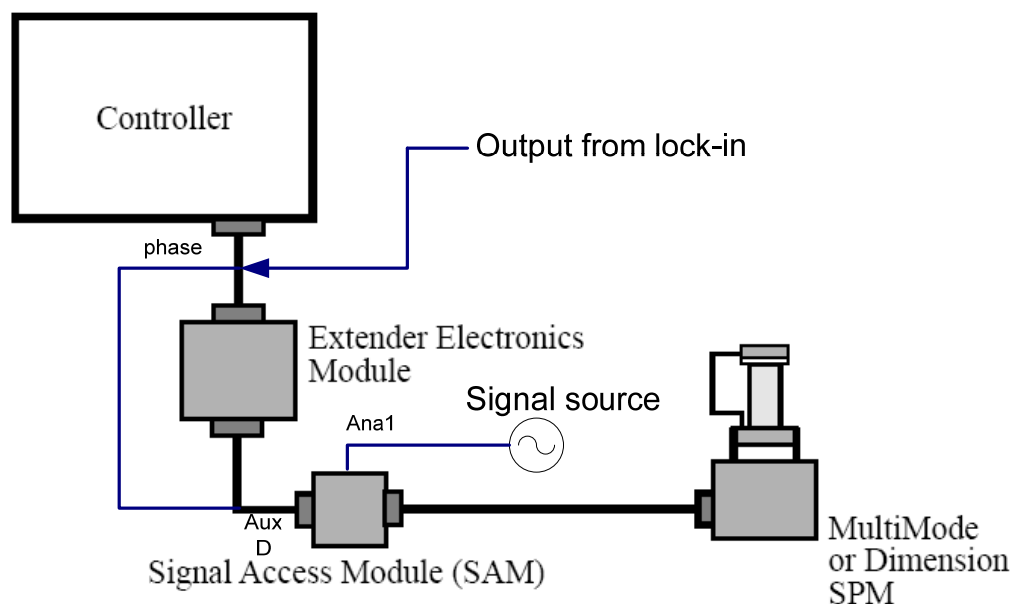


Figure 2-23 Diagram of modified signal configuration for piezoresistive readout (Adapted from Veeco DI Nanoscope™ signal access module manual)

Preliminary scanning experiments on a silicon calibration grating sample obtained decent images. Figure 2-24 shows two scanned images of the sample, one from the height signal and one from piezoresistive resonance signal when the AFM is under interleave mode. The piezoresistive signal is recognized by the AFM computer as a phase signal. These two images show excellent consistence, except for extra noise in the second image from un-optimized detection circuitry and open-loop operation during the second scan, which lets in noises from system vibration and instability. Single scan traces from two signals are displayed in Figure 2-25. Even without other higher-level feedback control, as used in the constant height scanning mode, the piezoresistance resonance signal follows the sample surface height profile very well.

These data first demonstrate the feasibility of using self-sensing metallic piezoresistive read-out for AFM applications. This method has great potential as a highly integrated and compact instrument by circumventing the need for laser optics and consequent maintenance and alignment of components. The low impedance of the transducer also allows high frequency cantilevers to be used for very high speed (> 1 MHz) and wide bandwidth scanning probe applications. Only one extra fabrication process is needed to convert available commercial cantilevers to self-sensing cantilevers. The attributes of low cost, easy fabrication, high sensitivity, and low temperature coefficients enable these cantilevers to be the very promising next generation of scanning probes.

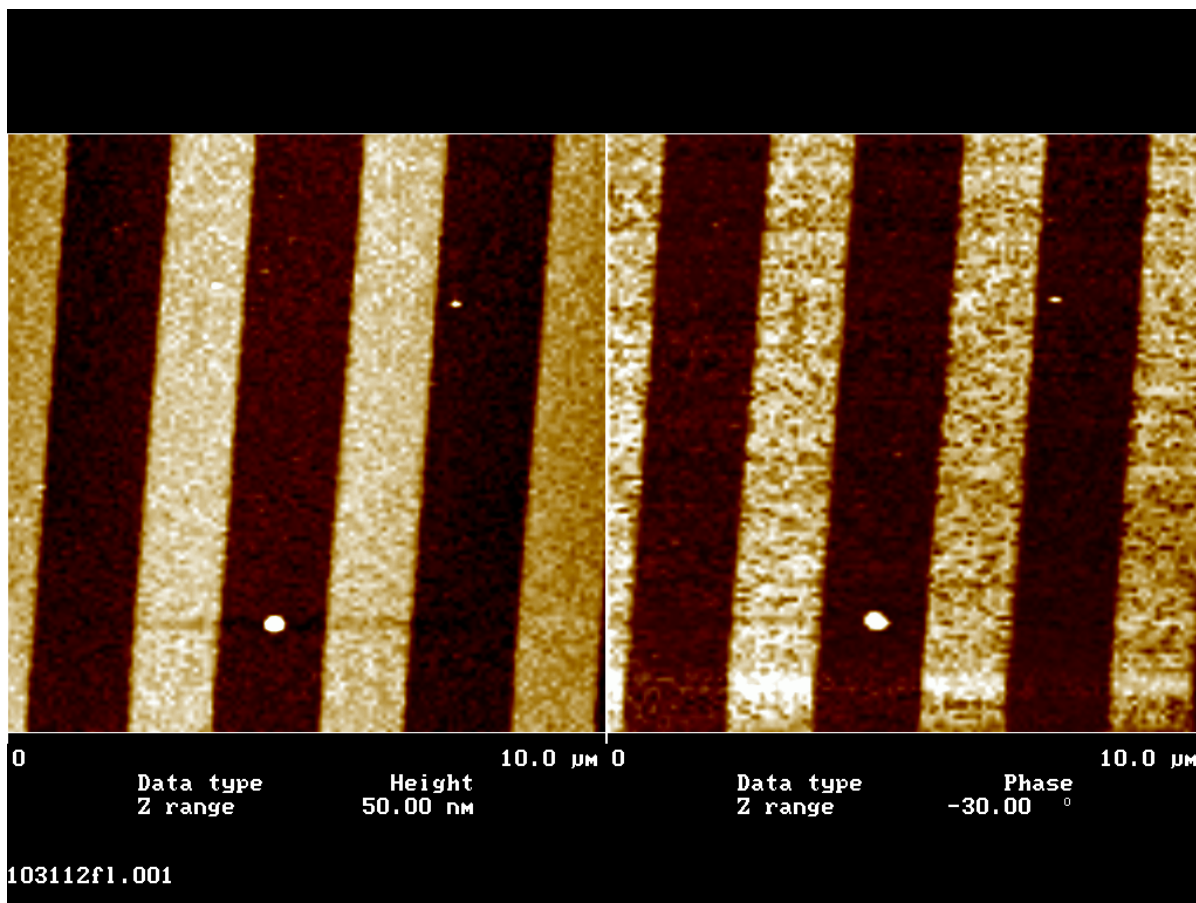


Figure 2-24 Images of silicon calibration grating sample, with 30 nm step height. Left image is from the height signal. Right image is from piezoresistive resonance signal. It is recognized by the AFM control computer as a phase signal

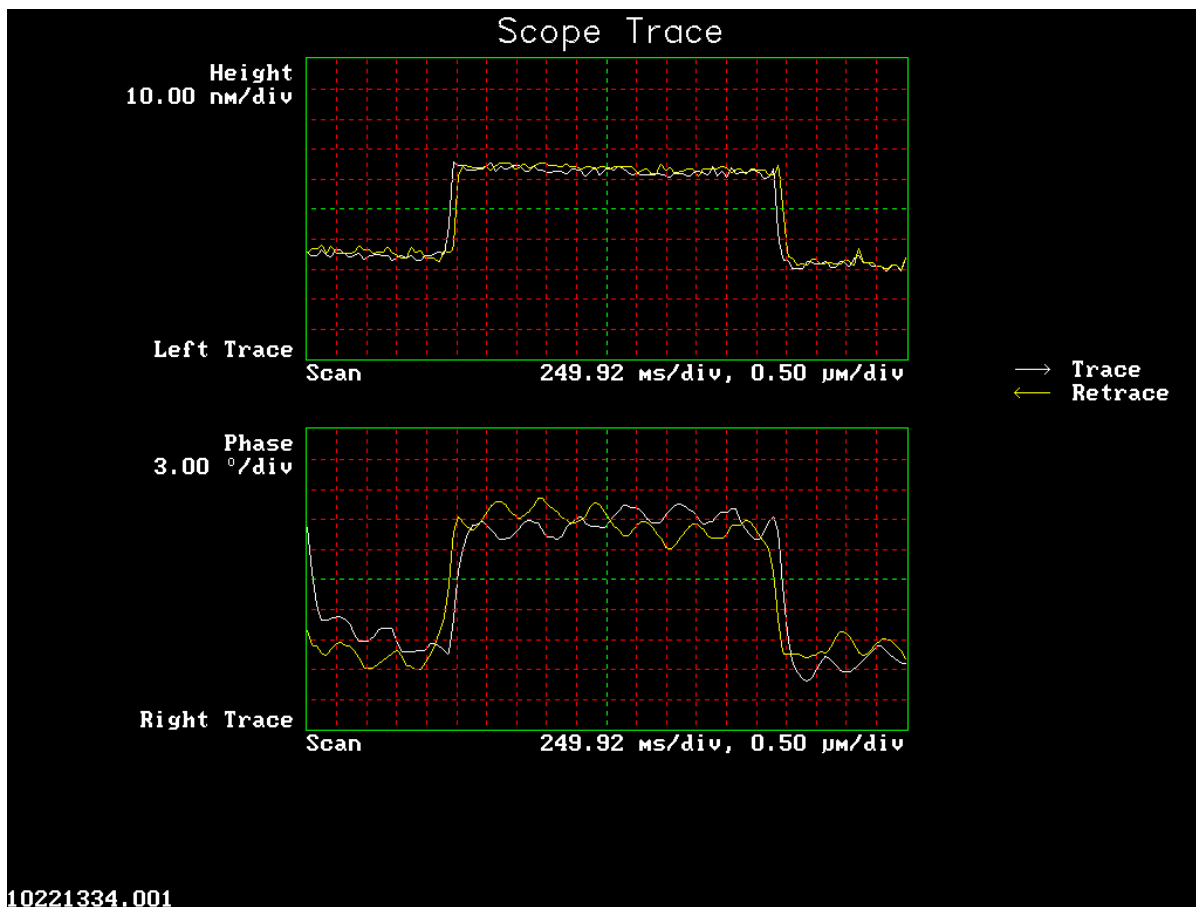


Figure 2-25 Scan trace of calibration grating step of 30 nm. Top trace is from height signal and bottom trace is from piezoresistive resonance signal. Again, the piezoresistive signal is recognized as a phase signal by the system.

2.9 Reference

- 1 Kuczynski, G. C. Effect of elastic strain on the electrical resistance of metals. *Phys. Rev.* **94**, 61-64 (1954).
- 2 Parker, R. L. and Krinsky, A. Electrical resistance-strain characteristics of thin evaporated metal films. *J. Appl. Phys.* **34**, 2700-2708 (1963).
- 3 Jen, S. U., et al. Piezoresistance and electrical resistivity of pd, au, and cu films. *Thin Solid Films* **434**, 316-322 (2003).
- 4 Li, C. S., Hesketh, P. J., and Maclay, G. J. Thin gold film strain-gauges. *J. Vac. Sci. Technol. A* **12**, 813-819 (1994).
- 5 Smith, C. S. Piezoresistance effect in germanium and silicon. *Phys. Rev.* **94**, 42-49 (1954).
- 6 Kanda, Y. Piezoresistance effect of silicon. *Sensors and Actuators a-Physical* **28**, 83-91 (1991).
- 7 Harris, C. M. and Crede, C. E., *Shock and vibration handbook*, 2d ed. (McGraw-Hill, New York, 1976).
- 8 He, R. and Yang, P. Giant piezoresistance effect in silicon nanowires. *Nature Nanotechnology* **1**, 42 (2006).
- 9 Tortonese, M., Barrett, R. C., and Quate, C. F. Atomic resolution with an atomic force microscope using piezoresistive detection. *App. Phys. Lett.* **62**, 834-836 (1993).
- 10 Harley, J. A. and Kenny, T. W. High-sensitivity piezoresistive cantilevers under 1000 angstrom thick. *App. Phys. Lett.* **75**, 289-291 (1999).

- 11 Ried, R. P., et al. 6-mhz 2-n/m piezoresistive atomic-force-microscope cantilevers with incisive tips. *J. Microelectromech. Syst.* **6**, 294-302 (1997).
- 12 Takahashi, H., Ando, K., and Shirakawabe, Y. Self-sensing piezoresistive cantilever and its magnetic force microscopy applications. *Ultramicroscopy* **91**, 63-72 (2002).
- 13 Hooge, F. N. 1/f noise is no surface effect. *Phys. Lett. A* **29**, 139-140 (1969).
- 14 Arlett, J. L., et al. Self-sensing micro- and nanocantilevers with attonewton-scale force resolution. *Nano Lett.* **6**, 1000-1006 (2006).
- 15 Femlab 3.1 (Comsol AB, Burlington, MA, USA).
- 16 Roark, R. J., Young, W. C., and Budynas, R. G. *Roark's formulas for stress and strain*, 7th ed. (McGraw-Hill, New York, 2002).
- 17 Ekinci, K. L., Yang, Y. T., and Roukes, M. L. Ultimate limits to inertial mass sensing based upon nanoelectromechanical systems. *J. Appl. Phys.* **95**, 2682-2689 (2004).
- 18 Postma, H. W. C., et al. Dynamic range of nanotube- and nanowire-based electromechanical systems. *App. Phys. Lett.* **86**, - (2005).
- 19 Husain, A., et al. Nanowire-based very-high-frequency electromechanical resonator. *App. Phys. Lett.* **83**, 1240-1242 (2003).
- 20 Kozinsky, I., et al. Tuning nonlinearity, dynamic range, and frequency of nanomechanical resonators. *App. Phys. Lett.* **88**, - (2006).
- 21 Bargatin, I., Kozinsky, I., and Roukes, M. L. Efficient electrothermal actuation of multiple modes of high-frequency nanoelectromechanical resonators. *App. Phys. Lett.* **90** (2007).

- 22 Callen, H. B. and Welton, T. A. Irreversibility and generalized noise. *Phys. Rev.* **83**, 34-40 (1951).
- 23 Anczykowski, B., et al. Analysis of the interaction mechanisms in dynamic mode sfm by means of experimental data and computer simulation. *Applied Physics a-Materials Science and Processing* **66**, S885-S889 (1998).
- 24 Tamayo, J., et al. High-q dynamic force microscopy in liquid and its application to living cells. *Biophysical Journal* **81**, 526-537 (2001).
- 25 Newell, W. E. Miniaturization of tuning forks. *Science* **161**, 1320-1326 (1968).
- 26 Harrington, D. A., Mohanty, P., and Roukes, M. L. Energy dissipation in suspended micromechanical resonators at low temperatures. *Physica B* **284**, 2145-2146 (2000).
- 27 Liu, X., et al. Low-temperature internal friction in metal films and in plastically deformed bulk aluminum. *Physical Review B* **59**, 11767 (1999).
- 28 Sekaric, L., et al. Nanomechanical resonant structures in silicon nitride: Fabrication, operation and dissipation issues. *Sensors and Actuators a-Physical* **101**, 215-219 (2002).
- 29 Bhiladvala, R. B. and Wang, Z. J. Effect of fluids on the q factor and resonance frequency of oscillating micrometer and nanometer scale beams. *Phys. Rev. E* **69**, 036307 (2004).
- 30 Cho, Y. H., Pisano, A. P., and Howe, R. T. Viscous damping model for laterally oscillating microstructures. *J. Microelectromech. Syst.* **3**, 81-87 (1994).

Chapter 3

Measurement techniques

In this chapter, detailed descriptions of measurement techniques, setup and schematics are included. In the first section, the principles and the methods to measure noise performance of the studied NEMS devices are described, including Johnson noise, $1/f$ noise, and thermomechanical noise. Then measurement scheme using frequency down-conversion in order to reduce the coupled background signal is explained. Finally, phase-locked loop technique implemented to track and measure the resonance frequency of the NEMS devices is described. Both theoretical analysis and data acquired from NEMS devices measurement are discussed and compared. Expectation for further improvement of frequency measurement accuracy is also discussed.

3.1 Noise measurement: thermomechanical noise, Johnson noise and $1/f$ noise

In order to analyze and optimize the device performance, it is necessary to understand every source of noise. Quantitative measurement of every type of noise is essential to determine the sensitivity and resolution of the device.

For piezoresistive transduction of mechanical devices, the main intrinsic noise sources include the thermal noise of the resistive transducer itself, i.e., Johnson noise; the low frequency $1/f$ noise, or Hooge's noise; and the thermomechanical noise of the mechanical device¹. Johnson noise is also called white noise, as its spectral density is constant over the frequency spectrum until extremely high frequencies are reached. The spectrum of $1/f$ noise is as described by its name, having one over f dependence on frequency. It is only noticeable at relatively low frequency below which it dominates over Johnson noise. Thermomechanical noise is the mechanical analog of Johnson noise, arising from the thermally actuated mechanical fluctuation of the device, and can be better understood using fluctuation-dissipation theorem². More detailed explanation can be found elsewhere³. For a mechanical resonator device, the noise spectrum shows a Lorentzian peak at the resonance frequency. The visibility of thermomechanical noise peak is an indication of optimal transducer read-out noise performance such that the thermal noise of the mechanical motion dominates the readout noise. All of these noises are intrinsic and fundamental to the device, and can only be improved by means of the design of the device and the selection of material. For a given device, there are no other methods to reduce these noises except for reducing the temperature. Reduction of these

noises by proper selection of transducer material and device engineering to achieve optimal sensitivity and resolution is one of the main goals of device researches.

To characterize each noise source, different measurement schemes must be employed. Details of each of them and results measured from various piezoresistive NEMS devices are discussed in the following sections.

3.1.1 Johnson noise and thermomechanical noise measurements

The noise of a measurement system consists of two major parts, the noise from the device itself and noise from the read-out amplifiers employed in the measurement. For the amplifier noise in an appropriate cascade of multiple amplification stages, if the first stage provides sufficient gain, subsequent stages will only contribute negligible noises when referred to the input. So, most of the time, only the noise of the first amplifier (preamplifier) needs to be considered.

The Johnson noise spectral density of a resistor R is given by

$$v_n^J = \sqrt{4k_B TR} \quad [\text{V}/\sqrt{\text{Hz}}], \quad (3.1)$$

where:

$$k_B = \text{Boltzman constant} = 1.38 \times 10^{-23} \text{ J/K},$$

T = absolute temperature of the resistor,

R = resistance of the resistor.

When the device is connected to an amplifier, contribution of the amplifier noise to the total noise in the system can be calculated using the noise figure (NF) of the amplifier. Noise figure (NF) is defined as:

$$NF = 20 \log_{10} \frac{\text{total noise after amplification(referred to input)}}{\text{thermal noise of the device}} \text{ [dB]} \quad (3.2)$$

So the total noise referred to input after the first amplification is:

$$v_n^T = \text{total noise} = 10^{(NF/20)} \times \text{thermal noise} = 10^{(NF/20)} \times \sqrt{4k_B TR} \quad (3.3)$$

For a typical metallic piezoresistive NEMS device with DC resistance of 100 Ω , using an amplifier with noise figure of 2 dB at the interested frequency range, the expected total noise spectral density referred to input at that frequency range will be 1.6 nV/ $\sqrt{\text{Hz}}$.

Thermomechanical noise of a mechanical device can be transduced into electrical signal, as extra voltage noise appearing above the existing noise floor using various transduction schemes, such as piezoresistive and optical detection methods¹. Given sufficient measurement sensitivity, thermomechanical motion of a high-Q mechanical resonator device can be conveniently measured in the electrical domain, showing a Lorentzian noise spectral peak centered at its resonance frequency. Metallic piezoresistive read-out has been demonstrated with superior sensitivity, such that thermomechanical noise spectrum peaks at as high as 127 MHz can be observed with our cantilevers.

It is also notable that measurement of thermomechanical noise spectra provides a viable way to calibrate the displacement sensitivity. This technique has been proven to be a reliable method and is widely used to calibrate scanning probes in the AFM community⁴. An example of using this method is described in this section.

From fluctuation-dissipation theory, the thermomechanical noise arises from a white equivalent noise force exerted on the device by the heat bath of the surrounding environment, and its force spectral density is given as:

$$S_{th}^F = \frac{4k_B T K}{\omega_0 Q}. \quad (3.4)$$

Again here:

k is Boltzman constant,

T is absolute temperature,

K is the force constant of the device,

ω_0 is the resonance frequency,

Q is the quality factor.

For a damped resonator, the displacement spectral density resulting from this thermal driving force is:

$$S_{th}^z(\omega) = \frac{4\omega_0 k_B T}{mQ} \frac{1}{(\omega_0^2 - \omega^2)^2 + (\omega_0 \omega / Q)^2}. \quad (3.5)$$

So at resonance frequency, the displacement spectral density is

$$S_{th}^z \frac{1}{2} = \sqrt{\frac{4k_B T Q}{\omega_0 K}}. \quad (3.6)$$

By measuring the thermomechanical noise in the electrical domain, and calibrating the spectral signal with the expected displacement spectral density, the sensitivity of transduction from displacement to voltage can be calculated.

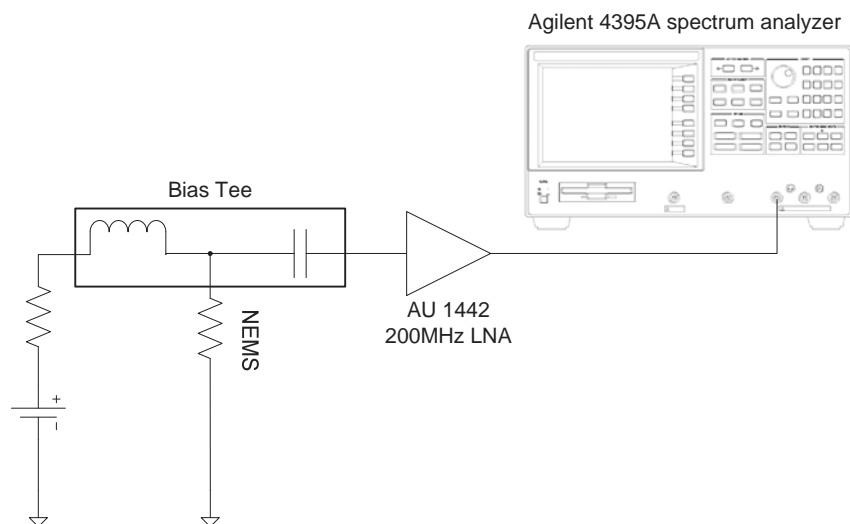


Figure 3-1 Circuitry to measure NEMS thermomechanical noise

Measurement circuitry shown in Figure 3-1 is used to measure the thermomechanical noise spectra of piezoresistive cantilever devices. The cantilever device is biased with a battery DC source via a bias tee to isolate the DC and AC parts of the signal. A low noise RF preamplifier (Mitek®, AU1442, 0.02-200 MHz) with a noise figure of 2dB is used for the first-stage amplification, and the output is fed to a spectrum analyzer (Agilent 4395A). The thermomechanical motion of the device induces strain fluctuation in the device's piezoresistor and causes fluctuation of its resistance. Under DC bias voltage, this resistance fluctuation is transferred into voltage noise, amplified, and measured as electrical voltage noise on the spectrum analyzer.

Typical noise spectra measured with low frequency cantilevers, as shown in Figure 2-5a and Figure 2-5b is displayed in Figure 3-2. Both the fundamental and second resonance modes of the cantilever from Figure 2-5a can be seen in the plot. The background noise floor varies with frequency due to different measurement conditions and the noise from the amplifier.

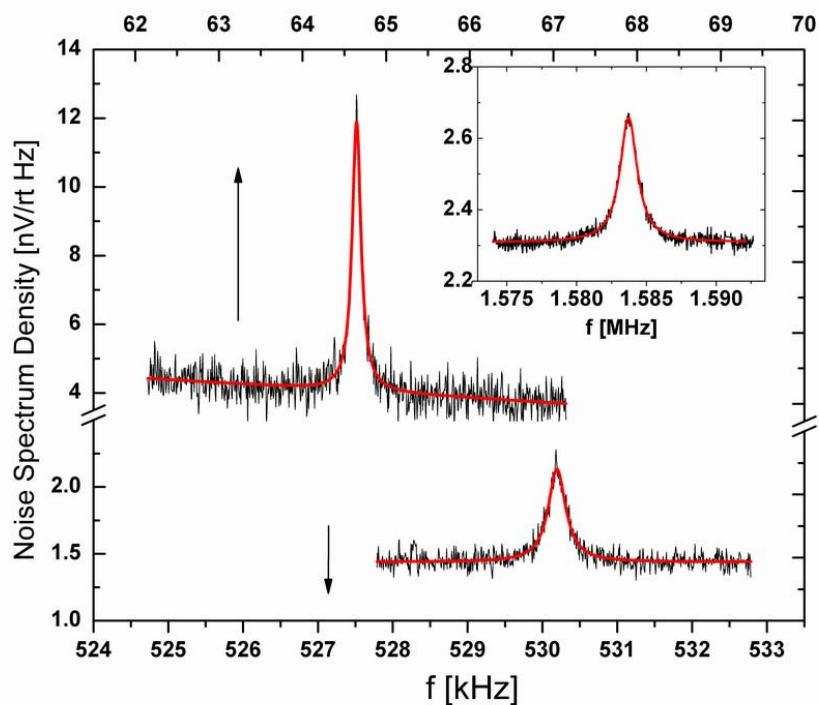


Figure 3-2 Thermomechanical noise spectrum measured on a low frequency cantilever. Noise spectral peak at first and second mechanical mode can be seen. Inset: Noise spectrum measured with 1.5 MHz cantilever. All data are measured with 100 mV bias voltage.

Metallic piezoresistive read-out is sensitive enough here to measure thermomechanical noise up to the VHF band (30 MHz – 300 MHz) for the first time to

our knowledge. In Figure 3-3, a 127 MHz device as shown in Figure 2-5d is measured, at room temperature and in 1 ATM pressure air. The displayed data is averaged by 200.

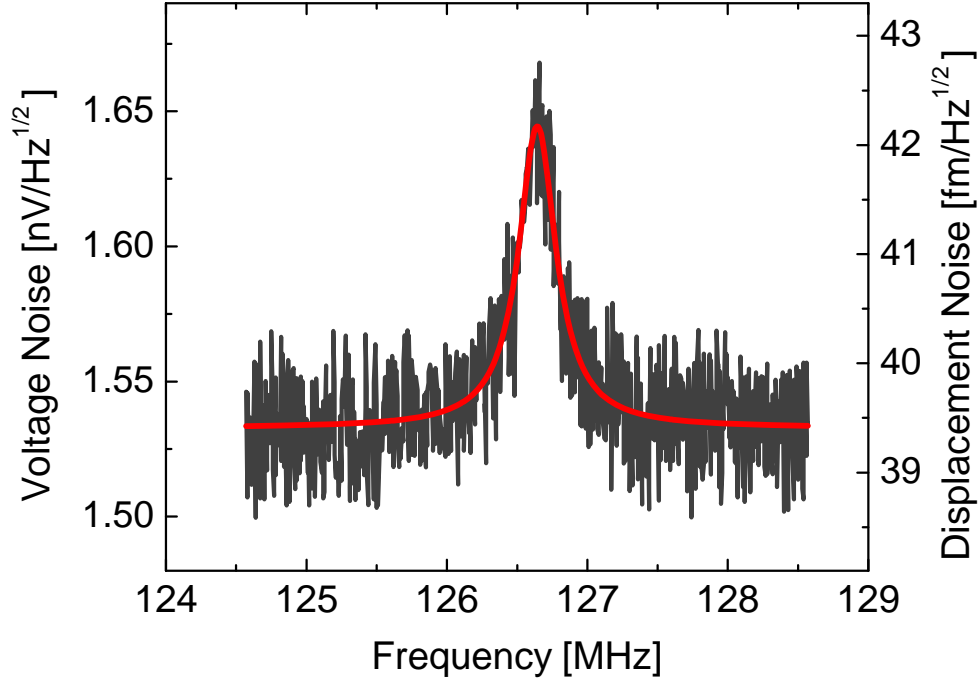


Figure 3-3 Thermomechanical noise spectrum measured on a VHF cantilever

We thus can use this measurement to calibrate the cantilever's displacement sensitivity. Its fundamental-mode force constant for end loading is $K \sim 32$ N/m, evaluated both analytically and by finite element simulation. Considering Figure 3-3, the output voltage noise floor near the 127 MHz resonance, $v_n^0 = (S_T + S_V)^{1/2} \sim 1.519$ nV/ $\sqrt{\text{Hz}}$, consists of the Johnson noise of the piezoresistive transducer ($R \sim 90 \Omega$, $S_T^{1/2} = \sqrt{4k_B T R} \sim 1.22$ nV/ $\sqrt{\text{Hz}}$) and the readout amplifier's noise referred to its input, $S_V^{1/2} \sim 0.92$ nV/ $\sqrt{\text{Hz}}$ (NF \sim 2dB at 50 Ω). The measured voltage noise spectral density on resonance is $v_n = (v_n^0 + v_n^m)^{1/2} \sim 1.644$ nV/ $\sqrt{\text{Hz}}$. The contribution arising from the

cantilever's thermomechanical motion is thus $v_n^m \sim 0.63 \text{ nV}/\sqrt{\text{Hz}}$. The displacement noise floor on resonance for a 127 MHz cantilever, limited by thermal noise, is $S_z^{1/2} = \sqrt{4k_b T Q / (2\pi f_0 K)} = 16 \text{ fm}/\sqrt{\text{Hz}}$. Hence we deduce the displacement responsivity (transduction "gain") of this self-sensing device as $R_v^z = 0.63 \text{ nV}/\sqrt{\text{Hz}} / 16 \text{ fm}/\sqrt{\text{Hz}} = 0.04 \text{ nV}/\text{fm}$. We further employ this responsivity to evaluate the displacement resolution, imposed by the off-resonance output voltage noise floor referred to the displacement domain using this responsivity, $x_n = \sqrt{S_z} \sim \sqrt{S_{V_{out}}(\omega \neq \omega_0) / R_T^2}$, which yields $x_n \sim (1.519 \text{ nV}/\sqrt{\text{Hz}}) / (0.04 \text{ nV}/\text{fm}) = 39 \text{ fm}/\sqrt{\text{Hz}}$. Thus, at 1 atm this displacement noise background, referred to the input (displacement domain), corresponds to resolution of $39 \text{ fm}/\sqrt{\text{Hz}}$, which is comparable to state-of-the-art optical detection via fiber-optic interferometry⁵.

As clearly seen in equation (3.6), cantilevers with a very high force constant K can provide very good displacement sensitivity at very high frequencies. In other circumstances, high force sensitivity is desired. From equation (3.4), a very low force constant K is wanted for applications requiring sensing small forces. Such cantilevers will have relatively large amplitude in thermomechanical motion. Figure 3-4 shows an example. This cantilever is made with 30 nm silicon carbide material, having a force constant of only 10 mN/m but a resonance frequency still around 1 MHz. The effect of its thermomechanical motion can clearly be seen in the SEM picture as the blurring of the cantilever tip. Its spectrum can be acquired by focusing the electron beam at the cantilever tip and analyzing the spectrum from the secondary electron detector. Using

equation (3.4), we can calculate thermomechanical noise limited force sensitivity of this cantilever as $144 \text{ aN}/\sqrt{\text{Hz}}$.

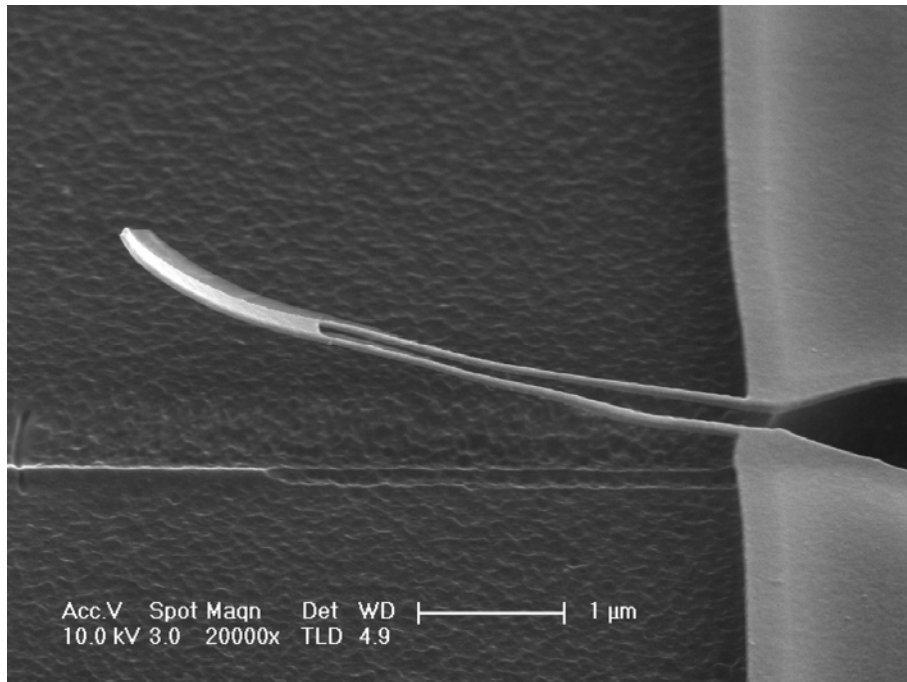


Figure 3-4 Cantilever made of 30 nm silicon carbide, with very low force constant of 10 mN/m. Its thermomechanical motion can be seen in this SEM picture, causing the blurring at the tip in the image.

From the same thermomechanical noise spectrum in Figure 3-2, we can also try to estimate the strain gauge factor of the gold film on cantilever. Equipartition principle also applies to elastic energy of the system: $E_{eff}V_{eff}\langle\varepsilon^2\rangle = k_bT$, where E_{eff} and V_{eff} are effective Young's modulus and volume respectively⁶. Most of the strain energy is concentrated on the legs, so that we can take the volume of them as effective volume. The mean squared strain is transferred to mean square noise voltage power by $\langle v^2 \rangle = \gamma^2 V_b^2 \langle \varepsilon^2 \rangle$. Using integrated voltage power and calculated value of mean squared strain, strain gauge factor

can be estimated. Finite element analysis also gives a numerical value for the ratio of mean squared strain value in metal layer only and averaged value in the composite cantilever leg structure. In this way, the gauge factor is estimated to be 2.38, which is consistent with the measured value in literature⁷.

3.1.2 1/f noise

Another significant attribute of metallic piezoresistive NEMS devices is its low 1/f noise, as compared to conventional semiconductor devices. This is due to the fact that metallic film has orders of magnitude higher carrier density ($\sim 10^{22} \text{ cm}^{-3}$) than semiconductors ($10^{18} \sim 10^{20} \text{ cm}^{-3}$). As described by Hooge's relation⁸, $S_R^{(1/f)} = 2\pi\zeta R^2 / (N\omega)$, metallic devices will have much larger the total number of carriers N than a semiconductor device of the same dimension. Also, semiconductor materials have a higher value of ζ , due to the doping atoms, defects, and combination-recombination processes inside the material. This attribute of low 1/f noise will be significantly advantageous for applications involving low frequency measurements, such as contact mode AFM, and other static force measurements.

However, measuring the very low 1/f noise of metallic devices is challenging, as most amplifiers using semiconductor transistors will have higher noise than the metallic device at low frequency. An AC bridge method, invented by John Scofield in 1987⁹, has to be employed to enable successful measurement. With this method, the measurement of device noise is super-heterodyned to the modulation frequency at which the preamplifier has optimal noise performance and contributes negligible extra noise.

A diagram of the measurement setup is shown in Figure 3-5. The first amplification stage uses transformer coupled amplifier (Stanford Research SR544). Its noise figure contour is shown in Figure 3-6. It can be seen that the best noise performance is at around 100 Hz and 50 Ω source resistance, corresponding to a noise figure less than 0.2 dB or less than 2% of the total noise. So at this condition, noise from the amplifier is truly negligible. The NEMS devices measured in the experiments typically have a resistance less than 100 Ω . The devices under measurement are connected in a Wheatstone bridge configuration with two high-precision metal wire decade resistors. Those decade resistor can be tune with precision better than 0.01% to null out any DC imbalance of the bridge, minimizing the loading to the amplifier transformer. A Stanford research SR830 lock-in amplifier is used to provide an excitation signal at 109 Hz with RMS amplitude of 10 mV. Demodulated signal output from the lock-in is connected to a HP 35665A FFT spectrum analyzer. Varying lock-in time constant (or measurement bandwidth) is used to measure different decades of frequency spectrum.

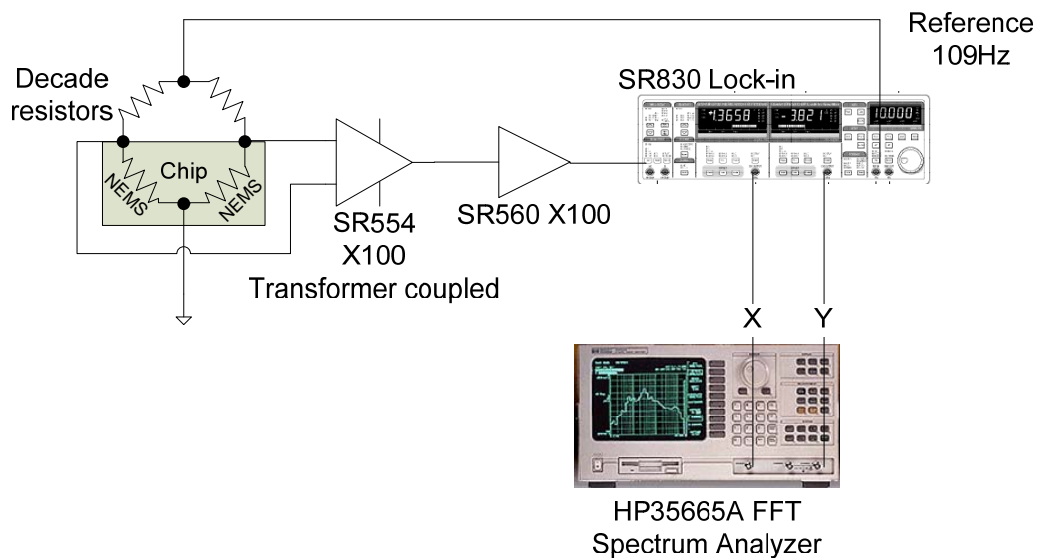


Figure 3-5 AC bridge setup to measure $1/f$ noise low resistance NEMS

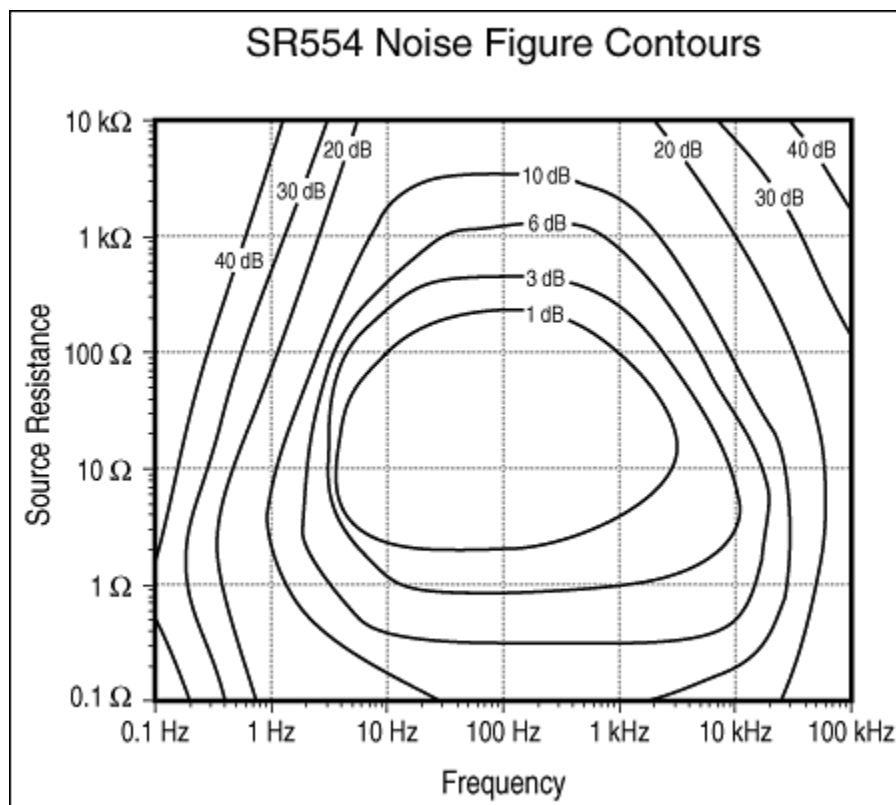


Figure 3-6 Noise figure contours of Stanford Research SR 554 amplifier

Another important and very useful attribute of this measurement method is that it is a phase-sensitive detection (PSD). The dual phase lock-in amplifier can measure both the amplitude and phase information in the noise spectrum. In fact, the measured spectrum from the lock-in can be express as⁹:

$$S_v(f) = S_v^0(f_0 - f) + S_v^i(f) \cos^2 \delta . \quad (3.7)$$

Here f_0 is the carrier frequency, and f is the sweeping frequency in the spectrum. S_v^0 is the phase-insensitive background noise power spectrum, including Johnson noise from the device and amplifier noise. The significance of this AC bridge method is that the measured low-frequency noise is $S_v(f = 0) = S_v^0(f_0)$. So if f_0 is selected to be at the lowest noise point in the amplifier noise figure contours, amplifier noise is minimized. S_v^i is the phase-sensitive part of the noise, in our case mostly including the $1/f$ noise of the device. (It is actually due to the $1/f$ resistance fluctuation of the devices.) It only appears as voltage noise when excitation current is flowed through the device, and can be measured with different phase δ . Using lock-in amplifier, both in-phase ($\delta = 0$) and its quadrature phase ($\delta = 90^\circ$) components of noise spectrum can be measured, and both components of S_v^0 and S_v^i can be decomposed with the measurements as described by equation (3.8).

$$S_v(f, \delta) = \begin{cases} S_v^0(f_0 - f) & , \delta=0 \\ S_v^0(f_0 - f) + S_v^i(f) & , \delta=90^\circ \end{cases} \quad (3.8)$$

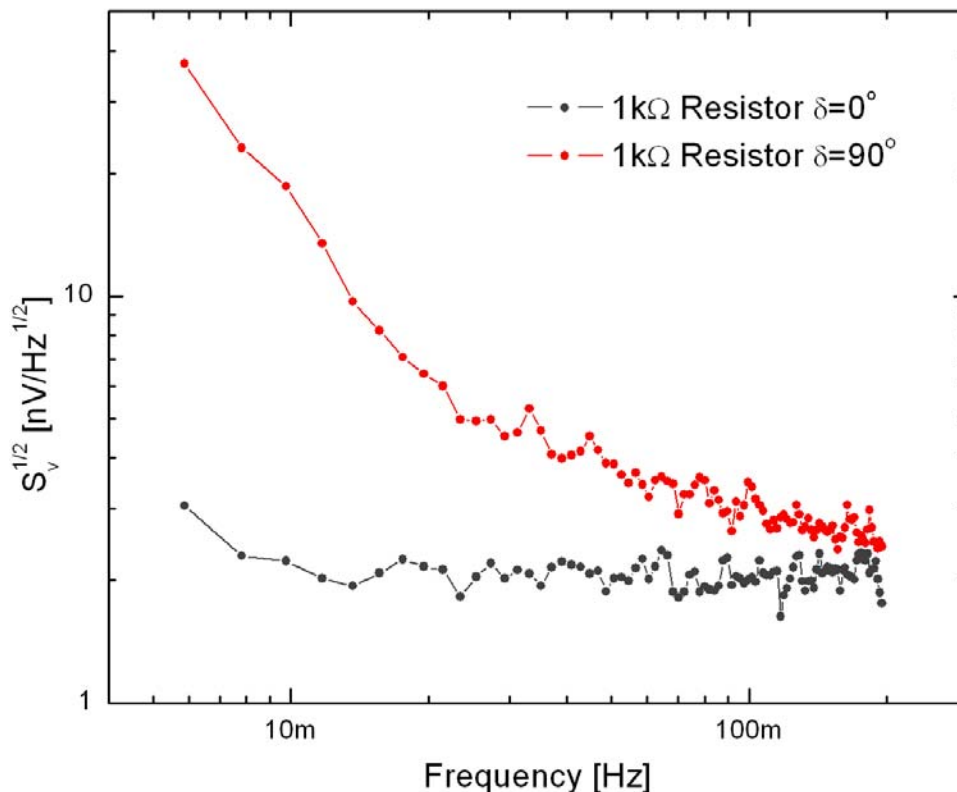


Figure 3-7 Low frequency noise spectrum of 1 k Ω metal film resistor. Both quadratures of lock-in modulation are measured

An example of the phase-sensitive measurement is shown in Figure 3-7, measured with a commercial metal film resistor. Both quadratures from the lock-in are plotted. The spectrum for $\delta = 0$ shows negligible frequency dependence over the measured frequency band as predicted by equation (3.8), except for some increase at very low frequencies (mainly due to the drift of measurement instruments), while the spectrum measured with $\delta = 90^\circ$ shows clear $1/f$ frequency dependence with a knee at around 100 mHz. This demonstrates the capability of the heterodyne measurement method, and also the very low $1/f$ noise of metal film devices.

Two NEMS cantilever devices, as shown Figure 2-5c and d are then measured, and the result is displayed in Figure 3-8. The dimension of the cantilever from Figure 2-5c's metallic piezoresistor is 3 μm long and 0.2 μm wide, while the cantilever from Figure 2-5d's piezoresistor is 1 μm long and 0.1 μm wide. Including the different resistance of the two devices, from Hooge's relation, the cantilever in Figure 2-5d is expected to have larger $1/f$ noise than the cantilever in Figure 2-5c. This is exactly what was observed from measured noise spectrum data, which shows higher noise from Figure 2-5d's cantilever at low frequency, even though it has less noise at higher frequency. The measured $1/f$ noise frequency knees are 8 Hz for Figure 2-5c's cantilever and 100 Hz for Figure 2-5d's cantilever, respectively. The very low $1/f$ noise of these nanoscale devices is very significant compared with measured data from semiconductor (doped silicon) devices which shows $1/f$ noise at 100 $\text{nV}/\sqrt{\text{Hz}}$ level with frequency knee at around 1–10 kHz ¹⁰. When scaled to the same dimension and biasing conditions, the estimated $1/f$ noise of metallic devices is more than two orders of magnitudes lower than that of devices made of doped silicon, as expected from the previous discussion.

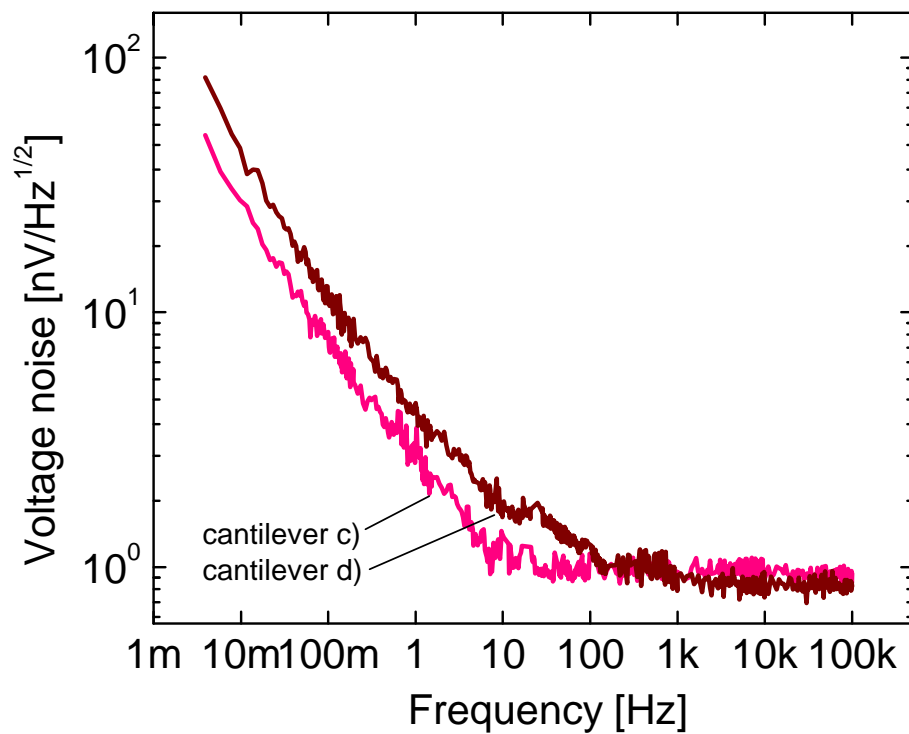


Figure 3-8 Low frequency noise spectrum of two NEMS cantilever devices. Their $1/f$ noise knees are measured to be at 8 Hz for cantilever Figure 2-5c and at 100 Hz for cantilever Figure 2-5d respectively

3.2 Frequency down-conversion measurement

The piezoresistive detection enables convenient electrical measurement of the devices' mechanical motion with integrated transduction. But unlike optical detection methods in which the actuation and detection circuits are isolated by laser beam, piezoresistive detection method integrates both into one electrical circuit. Although the impedance mismatching problem can be solved by using low resistivity metal film transducers, other problems caused by this integration still remain. The major one is the strong capacitively coupled background signal from the piezoelectric actuator to the detection port when homodyne detection is used. This background signal can be many orders of magnitude larger than the actual piezoresistive signal from the miniscule mechanical motion of the device. It severely lowers the system's dynamics range and makes the cantilever useless for practical applications which require accurate measurement of resonance frequency, amplitude and phase.

A heterodyne frequency down-conversion method was invented by Bargatin et. al., originally designed for solving impedance mismatching problems for their doped silicon piezoresistive cantilevers with high resonance frequency. A diagram of the measurement scheme is shown in Figure 3-9. Instead of using DC bias, an AC biasing signal is used, and its frequency is kept at $\omega + \Delta\omega$, a fixed intermediate frequency $\Delta\omega$ higher than the actuation frequency ω . So we can write the AC voltage signal generated across the NEMS devices as:

$$\begin{aligned}
\tilde{v}_o &= \frac{R_{d0}}{R_{d0} + R_b} V_{b0} \cos[(\omega + \Delta\omega)t] \times \frac{\Delta R_{d0}}{R_{d0}} \cos(\omega t + \phi) \\
&= \frac{\Delta R_{d0}}{R_{d0} + R_b} V_{b0} [\cos(\Delta\omega t - \phi) + \cos((2\omega + \Delta\omega)t + \phi)]
\end{aligned} \tag{3.9}$$

Here R_{d0} and R_b are the DC resistance of the device and a bias resistor, ΔR_{d0} is the amplitude of the resistance change of the device when it is driven with the actuator at frequency ω . An AC biasing signal $V_{b0} \cos[(\omega + \Delta\omega)t]$ is applied to the device. The bias signal mixes with the mechanical motion of the piezoresistor, and generates signals at beat frequencies $\Delta\omega$ and $2\omega + \Delta\omega$. Since the intermediate frequency $\Delta\omega$ can be set to be much lower than ω , the higher frequency beat signal at $2\omega + \Delta\omega$ can be easily filtered with a low pass filter. Only the lower frequency signal at $\Delta\omega$ is measured and the output signal can be expressed as:

$$v_o = \frac{\Delta R_{d0}}{R_{d0} + R_b} V_{b0} \cos(\Delta\omega t - \phi). \tag{3.10}$$

Since this beat frequency signal can only be generated from the mechanical oscillation of devices, and all other coupled signals at higher frequency from both the actuator and bias signal source can be aggressively removed by filters, in principle no background signal will be measured with this method. However, some nonlinear effects and interference still exist in the system and produce some frequency components at $\Delta\omega$, but with much lower amplitude compared to the wanted signal.

Figure 3-9 depicts the measurement setup. Two frequency sources are used to generate actuation and bias signals. Their outputs are split and mixed with a commercial mixer to provide the reference signal at intermediate frequency $\Delta\omega$ for the lock-in

amplifier. Intermediate frequency in the range of 50 kHz to 100 kHz, is often used. The signal from the device is filtered with a very sharp low-pass filter (cutoff frequency = 100 kHz), and measured with a lock-in amplifier after amplification.

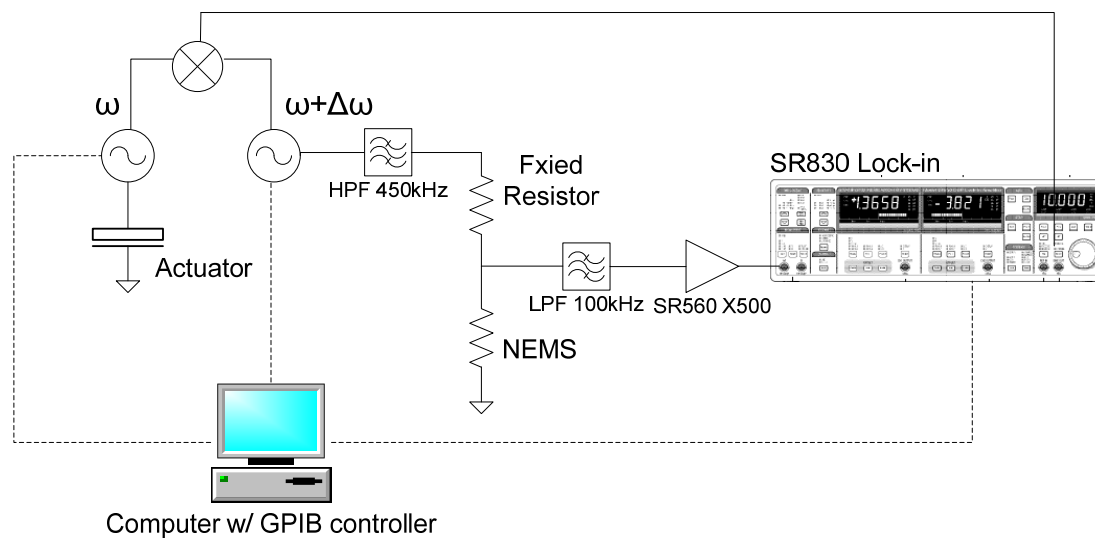


Figure 3-9 Frequency down-conversion piezoresistive measurement

Example results of using homodyne measurement with DC bias and network analyzers, and using frequency down-conversion methods are shown in Figure 3-10 and Figure 3-11. In Figure 3-10, the resonance peak is on a relatively large background, and the phase response is distorted and shifted. The greatly reduced signal background, and preserved phase of the resonance is very remarkable in Figure 3-11. The resonance peak amplitude to background ratio is higher than 100.

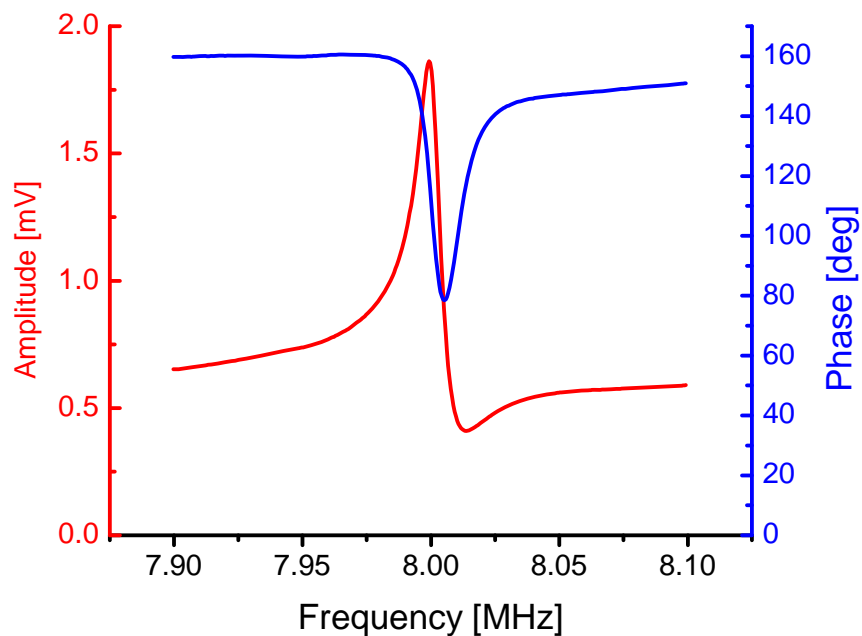


Figure 3-10 Amplitude and phase of a cantilever measured with DC bias and a network analyzer

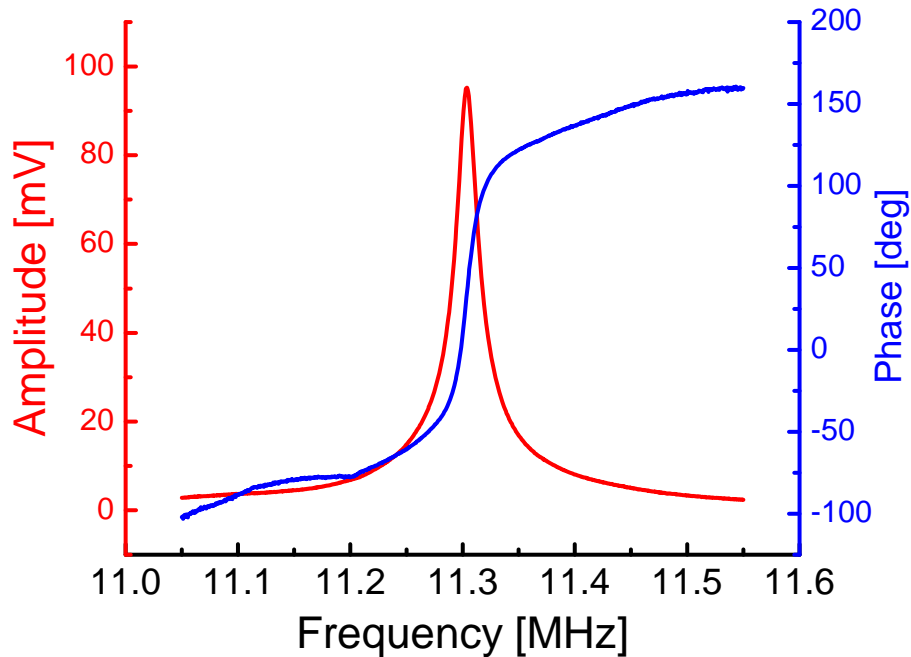


Figure 3-11 Amplitude and phase of a cantilever measured with the frequency down-conversion method

3.3 Phase-locked loop (PLL)

Phase-locked loop (PLL) is a very widely used technique in both analog and digital circuits, with applications for radio, telecommunications, and computers¹¹. In our nanomechanical resonator research, this technique is employed to track the resonance of the resonator device in real time, and for mass sensing and chemical gas sensing applications. It can provide frequency measurement at very high precision with large applicable bandwidth.

A phase-locked loop is composed of three elementary components (Figure 3-12): a phase detector, a loop filter and a voltage-controlled oscillator (VCO). In a nutshell, the principle of the phase-lock loop can be explained as follows: The phase of a periodic input signal is compared with the phase of a VCO signal at the phase detector and the difference is output as an error signal. This error signal is fed back to the control port of the VCO after a low-pass loop filter, and tunes the VCO frequency toward the input signal's frequency to reduce the error signal and close the loop. At locked state, the VCO frequency will be exactly equal to the frequency of the input signal within the loop bandwidth.

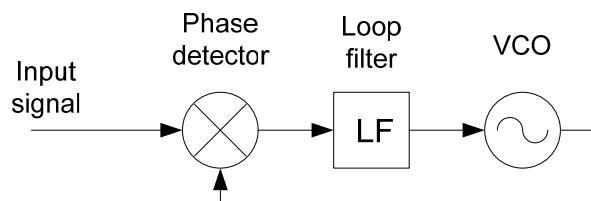


Figure 3-12 Basic phase lock loop (reproduced as in Ref 11)

When PLL is used to track the resonance frequency of a NEMS resonator, NEMS is actuated by the actuation signal output from the VCO, as shown in the diagram of Figure 3-13, in a way slightly different than the basic loop. The resonator response signal is amplified, and compared against the VCO signal at the phase detector. The error signal is fed back to control the VCO. Ideally, the resonator response signal should have the same frequency as the actuation signal from the VCO, but with a shifted phase from the resonator. It is clear from the displacement response function of a forced oscillator with damping:

$$z(\omega) = \frac{f/m}{\omega^2 - \omega_0^2 + i\omega\omega_0/Q}. \quad (3.11)$$

Its amplitude and phase are:

$$A(\omega) = \frac{f/m}{[(\omega^2 - \omega_0^2)^2 + \omega^2\omega_0^2/Q^2]^{1/2}} \quad (3.12)$$

$$\phi = \arctan\left[-\frac{(\omega_0^2 - \omega^2)}{\omega_0\omega/Q}\right]. \quad (3.13)$$

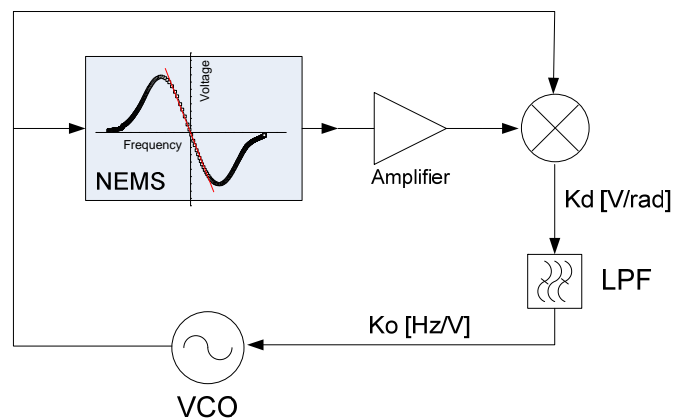


Figure 3-13 NEMS embedded in a phase-locked loop

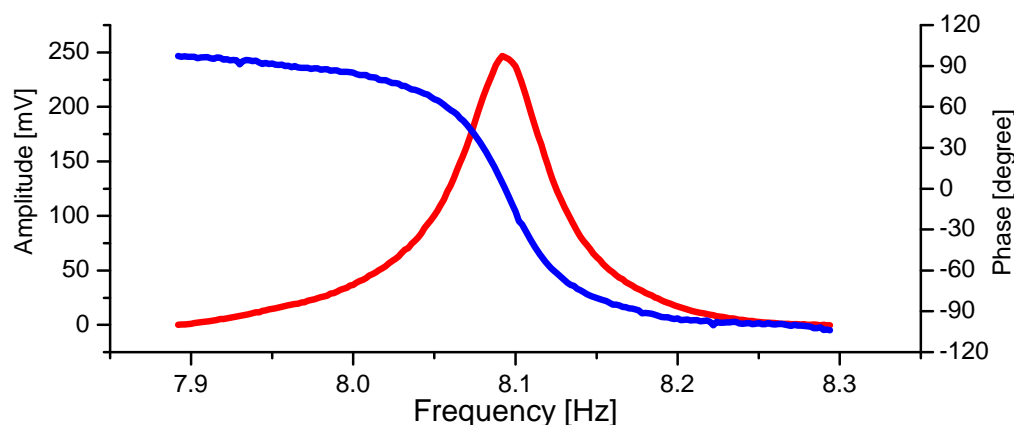


Figure 3-14 Amplitude and phase response at resonance frequency of a typical cantilever in air

As shown in Figure 3-14, at resonance $\omega = \omega_0$, the phase shift of the resonator is zero, and so is the error signal from the phase detector. It is clearer to see when the response is plotted in a polar coordinate, as in Figure 3-15. The circled point is the resonance and tracked point of PLL. Usually, a tunable phase shifter can be inserted before the phase detector to null out unwanted phase shift from the circuit components. The low pass filter will filter out high frequency signal components and noise. Three important loop parameters determining the loop gain and bandwidth are phase detector gain K_d , loop filter gain K_1 , and VCO gain K_o .

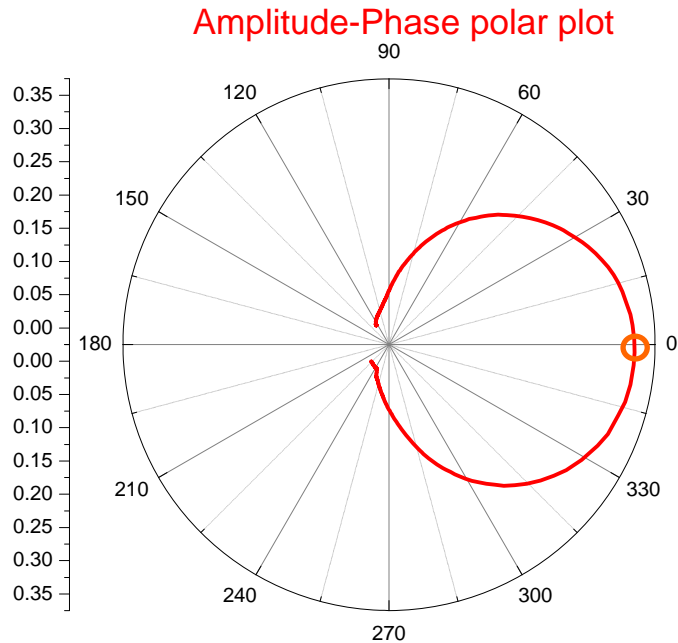


Figure 3-15 Polar plot of a NEMS amplitude-phase frequency response

Since the signal from the NEMS resonator using piezoresistive detection is often coupled with some background signal, basic loop configuration has to be modified to incorporate the frequency down-conversion method, similar to Figure 3-9 but without computer control. A diagram of the actual circuitry is shown in Figure 3-16.

One signal generator (HP 8648B) with external frequency modulation input is used as VCO. A signal at fixed intermediate frequency $\Delta\omega$ is generated by another generator, and split to the lock-in reference input and to mix with the actuation signal, generating the biasing signal at beat frequency $\omega + \Delta\omega$. A high pass filter after the mixer is necessary to filter out leaked signal at frequency $\Delta\omega$. Signal from the NEMS resonator is further filtered and amplified. Then the lock-in amplifier is used to demodulate the signal at the intermediate frequency $\Delta\omega$. One quadrature (Y) from the lock-in analog

output is fed back to the frequency modulation port of the VCO and tunes its frequency. This is because from equation (3.10) $Y \propto \sin(\theta)$. Since at resonance, $\theta = 0$, and $Y = 0$, when the loop tracks the resonance of NEMS, the negative feedback forces the NEMS signal's phase to be zero so that VCO frequency follows the resonance frequency.

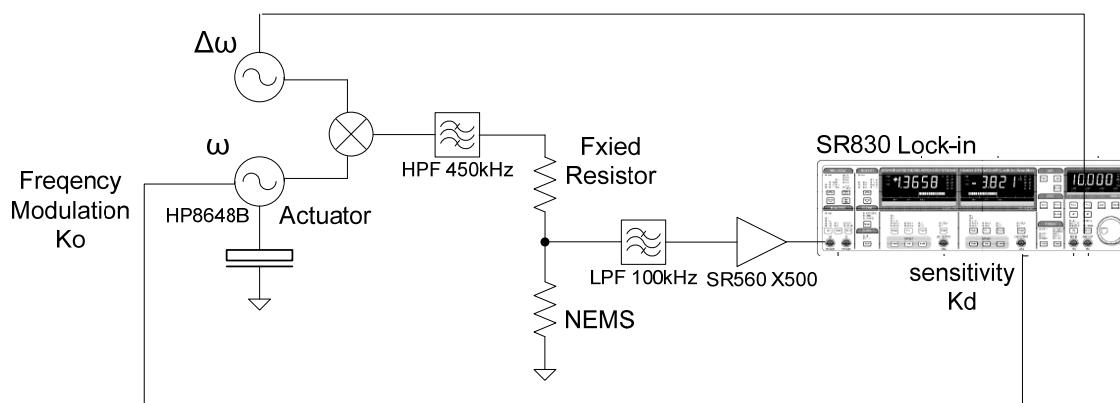


Figure 3-16 Piezoresistive frequency down-conversion NEMS phase-locked loop

If we plot quadrature Y versus frequency, when the phase shift from other circuit components is compensated, Y equals zero when VCO frequency is at resonance frequency. So the error signal (Y) can be approximated in linear relation to the frequency as equation (3.14) for small error signal:

$$v_e \equiv Y = K_d(f_c - f_{PLL}). \quad (3.14)$$

Here f_c is the center frequency of the resonance, f_{PLL} is the loop operating frequency or the VCO output frequency, and K_d is the feedback gain (V/Hz). Y quadrature data measured from a typical cantilever resonator device is shown in Figure 3-17.

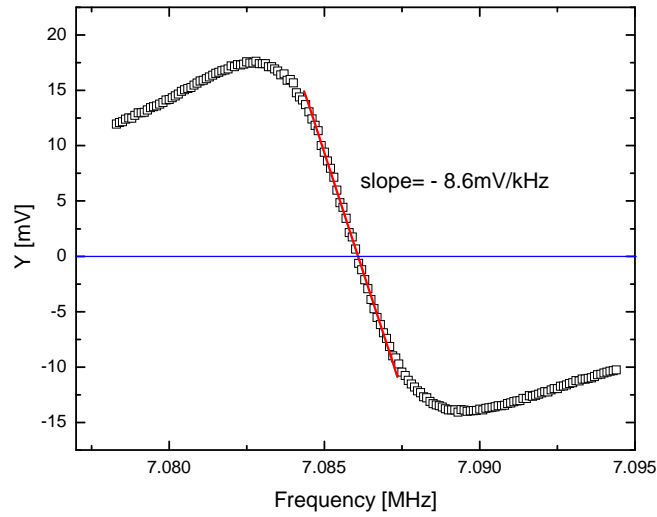


Figure 3-17 Y quadrature signal versus drive frequency of a typical NEMS cantilever

The error signal (Y quadrature signal) tunes VCO frequency as described by equation (3.15):

$$f_{PLL} = f_{VCO} + K_o v_e \quad (3.15)$$

Here f_{VCO} is the center frequency of the VCO with zero control voltage (free running frequency), and K_o is the VCO gain (Hz/V).

So the full closed loop can be described as:

$$\begin{aligned} f_{PLL} &= f_{VCO} + K_o K_d (f_c - f_{PLL}) \\ \Rightarrow \\ f_{PLL} &= \frac{K_o K_d}{1 + K_o K_d} f_c + \frac{1}{1 + K_o K_d} f_{VCO} \cdot \\ &= f_c^0 + \frac{K_o K_d}{1 + K_o K_d} \Delta f_c \end{aligned} \quad (3.16)$$

Here we use $f_c = f_c^0 + \Delta f_c$ and $f_{VCO} = f_c^0$, assuming that the VCO center frequency is set the same as the resonator's initial frequency. The final equation tells how the loop works. When the resonance frequency changes by Δf_c , the loop frequency changes by $\Delta f_c K / (1 + K)$, where $K = K_o K_d$ is the total loop gain. So the higher the loop gain, the more faithful the PLL tracks resonance frequency.

The VCO gain K_o can be set by the frequency modulation amplitude of the signal generator (HP 8648B). The actual loop feedback gain K_d is determined by the NEMS resonator (its frequency, quality factor, and signal amplitude), and the voltage gain of subsequent amplifiers and the lock-in amplifier. The value of K_d can be approximated with the slope of the data at the vicinity of the resonance frequency. In Figure 3-17, the measured slope is 8.6 mV/kHz. Knowing the value of K_o , their product gives the total loop feedback gain. We thus can calculate the total loop gain from the above parameters.

The loop gain can also be measured by changing the center frequency of the VCO and reading the locked frequency of the loop. From equation (3.16), the later is proportional to the VCO center frequency with coefficient of $(1 + K)^{-1}$. From measured data, we can determine the value of K . In the following, we use both methods to measure and calculate the loop gain, and compare their results. Figure 3-18 shows the measured data of loop gain, with various K_d and fixed K_o at 2 kHz/V, using a typical 7 MHz cantilever resonator. K_d is changed by changing the sensitivity of the lock-in amplifier.

Then, both calculated and measured values of loop gain are listed in Table 3-1. Excellent agreement can be found between the two methods.

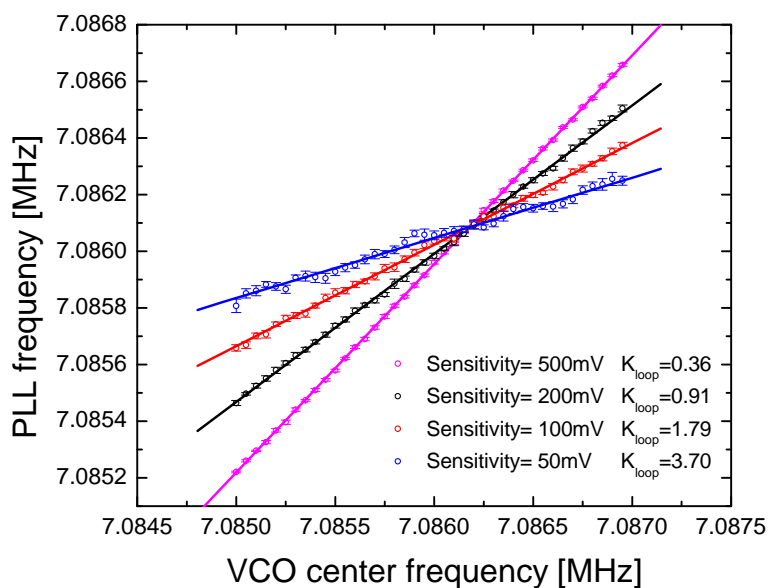


Figure 3-18 Phase-locked loop gain measurement with loop gain value set by various lock-in sensitivities

Table 3-1 Phase-locked loop parameters measured and calculated

VCO gain K_o (Hz/V)	2000			
Lock-in sensitivity (mV)	50	100	200	500
Feedback gain K_d (V/kHz)	1.72	0.86	0.43	0.172
Calculated total loop gain	3.44	1.72	0.86	0.344
Measured total loop gain	3.70	1.79	0.91	0.36

Equation (3.16) tells us that the loop frequency changes with the resonator frequency, with a coefficient of $(K/K+1)$. So the loop frequency fluctuation is also scaled by the factor of $(K/K+1)$ from the frequency fluctuation of the resonator itself. This effect can be clearly seen in Figure 3-19, the loop frequency fluctuation versus various loop gain K , and the fitting to $(K/K+1)$ functional form.

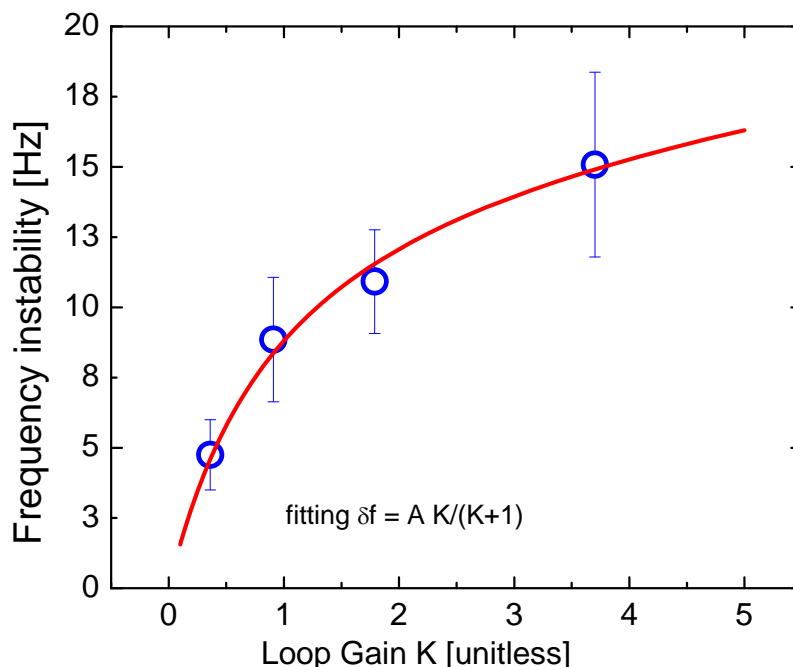


Figure 3-19 PLL Frequency stability versus loop gain K .

It is helpful to consider the minimum resolvable frequency shift limited by the thermomechanical noise of the mechanical resonator. A simplified expression is given in equation (3.17), where DR is the maximum dynamic range available to the resonator, defined as the ratio of the critical amplitude at the onset of nonlinearity to the thermomechanical displacement noise floor¹². BW is the measurement bandwidth.

$$\delta\omega = \left(\frac{\omega_0}{Q} \cdot BW\right)^{1/2} 10^{(-DR/20)} \quad [\text{Hz}/\sqrt{\text{Hz}}] \quad (3.17)$$

For the cantilever measured in Figure 3-19, its resonance frequency is $\omega_0 \sim 7$ MHz, and its quality factor is $Q \sim 500$ in vacuum. Assuming measurement bandwidth of 10 Hz and resonator dynamic range 60 dB, the minimum resolvable frequency shift is evaluated to be 0.37 Hz, corresponding to a mass resolution of about 40 zeptogram. This is way below the actual measured frequency fluctuation in Figure 3-19, even with very low loop gain. Thus, it can be concluded that the frequency noise in the PLL measurement is not limited by the intrinsic noise of the resonator, but mostly from the noise in the measurement electrical circuits and environmental fluctuations, including temperature and pressure variation¹³. These extra noise sources severely deteriorate the mass sensitivity of the resonator. Detailed theoretical noise analysis can be found in Reference¹². One order of magnitude improvement in frequency noise performance can be expected upon optimization of the system.

An alternative implementation of phase-locked loop is to use a microcomputer as a feedback controller, such as the scheme shown in Figure 3-9. In such a scheme, the frequency of the signal generator is not controlled by analog signal and using a VCO, but is calculated and set by the computer software. Thus, there is no limit on the range of traceable frequency by the resonator bandwidth (100 kHz to 1MHz for typical high frequency resonators) or the modulation amplitude of the VCO (up to 100 kHz for model HP 8648B). The drawback is that the loop bandwidth is limited by the speed of communication between the computer and the instruments, which is about 10 Hz in our setup, using the GPIB interface. This scheme is more often used for low bandwidth measurement in this thesis, while the analog loop allows for much faster measurements.

1.8 Reference

- 1 Gabrielson, T. B. Mechanical-thermal noise in micromachined acoustic and vibration sensors. *IEEE Transactions on Electron Devices* **40**, 903-909 (1993).
- 2 Callen, H. B. and Welton, T. A. Irreversibility and generalized noise. *Phys. Rev.* **83**, 34-40 (1951).
- 3 Cleland, A. N. and Roukes, M. L. Noise processes in nanomechanical resonators. *J. Appl. Phys.* **92**, 2758-2769 (2002).
- 4 Hutter, J. L. and Bechhoefer, J. Calibration of atomic-force microscope tips. *Rev. Sci. Instrum.* **64**, 1868-1873 (1993).
- 5 Rugar, D., Mamin, H. J., and Guethner, P. Improved fiber-optic interferometer for atomic force microscopy. *App. Phys. Lett.* **55**, 2588-2590 (1989).
- 6 Heer, C. V. *Statistical mechanics, kinetic theory, and stochastic processes*. (Academic Press, New York, 1972).
- 7 Li, C. S., Hesketh, P. J., and Maclay, G. J. Thin gold film strain-gauges. *J. Vac. Sci. Technol. A* **12**, 813-819 (1994).
- 8 Hooge, F. N. 1/f noise is no surface effect. *Phys. Lett. A* **29**, 139-140 (1969).
- 9 Scofield, J. H. Ac method for measuring low-frequency resistance fluctuation spectra. *Rev. Sci. Instrum.* **58**, 985-993 (1987).
- 10 Harley, J. A. and Kenny, T. W. High-sensitivity piezoresistive cantilevers under 1000 angstrom thick. *App. Phys. Lett.* **75**, 289-291 (1999).
- 11 Gardner, F. M. *Phaselock techniques*, 3rd ed. (John Wiley & Sons, Hoboken, NJ, 2005).

- 12 Ekinci, K. L., Yang, Y. T., and Roukes, M. L. Ultimate limits to inertial mass sensing based upon nanoelectromechanical systems. *J. Appl. Phys.* **95**, 2682-2689 (2004).
- 13 Robins, W. P. *Phase noise in signal sources: Theory and applications*. (Peter Peregrinus on behalf of the Institution of Electrical Engineers, London, 1982).

Chapter 4

Nanomechanical chemical gas analysis with gas chromatography (GC)

Microscale total analysis system (μ TAS) has been of great research interest during the last few decades¹. The need for miniaturized, compact, portable, and high-speed chemical and biological analysis systems is driven by applications both in chemical, biological, and environmental sensing, and in homeland security².

Both qualitative and quantitative measurement and detection of specific chemical compounds provide important information for the above-mentioned application circumstances. Separation-based chemical analysis methods, such as chromatography and electrophoresis, are particularly suitable for those tasks. Particularly in chromatography, separation of a complex chemical mixture is achieved by the different partition between a mobile phase and a stationary phase of each composition. A non-specific or selective detector can be used to detect the separated analytes, and provide quantitative analysis information about the mixture^{3,4}. Miniaturization of such a chromatographic system is being pursued by several groups, and substantial progresses have been made⁵.

In this chapter, we describe the development of a polymer-coated NEMS resonator detector in a miniaturized gas chromatographic system. After a brief

introduction of gas chromatography, cumulative improvements of device sensitivity, speed, and analysis capability are described. Finally, a successful analysis of the mixture of chemical warfare agent simulants and their interferents are discussed. Problems related to the slow diffusion process of gas species into polymer phase are also discussed.

4.1 Introduction of gas chromatography: column and detectors

Gas chromatography or GC is one of the most important instruments in modern analytical chemistry. It can be used to analyze organic and inorganic materials, in gas, liquid, and solid phase (after being dissolved in solvents). Quantitative analysis of complicated samples with high precision is obtained routinely. For example, a gas chromatography-mass spectroscopy or GC/MS system is considered the gold standard of analytical chemistry. Modern instruments utilize high levels of automation so that hundreds of samples can be analyzed per day^{6,7}.

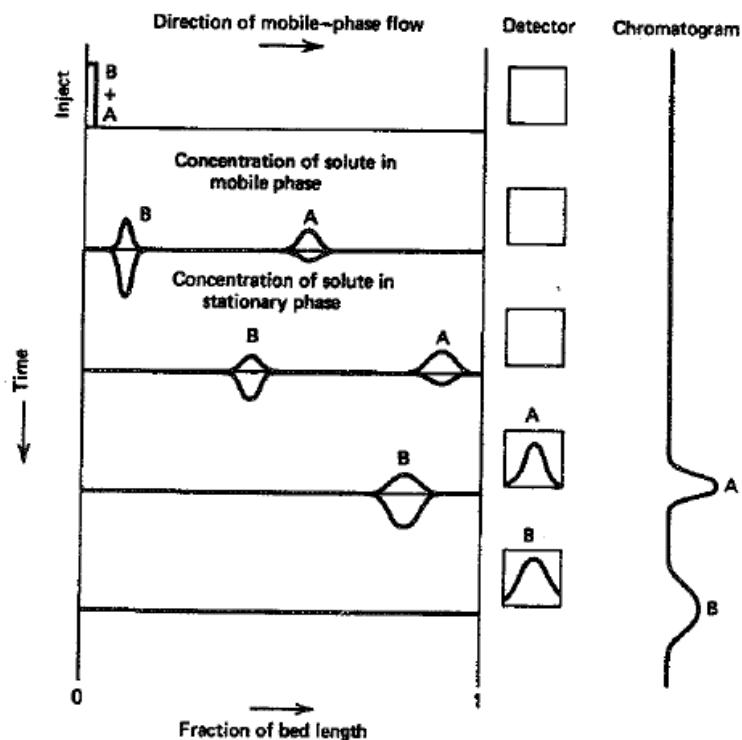


Figure 4-1 Schematic representation of the chromatographic process. (Reproduced from Miller, J.M., *Chromatography: Concepts and contrasts*, 2nd edition, John Wiley & Sons, Inc., 2005, p. 44.)

Chromatography is the method used to separate components of a mixture sample by utilizing their different partition in stationary phase — in the case of capillary GC, the coating of the column wall. Vaporized sample is carried by the mobile phase (the carrier gas) through the separation column, and the components of the sample are separated based on their different affinity to and partition coefficients in the stationary phase. At a given operation temperature, when ideal separation is obtained, each component has its own characteristic elution time at which it exits the column. The effluents from the column are sensed by a detector whose signal is related to the quantity (the relative concentration or total mass/volume) of the chemicals, showing peaks in its signal trace.

Such a trace is called a chromatogram. Then each component can be identified by its corresponding peak's position in the chromatogram. Quantitative analysis of each composition of the sample can be achieved by further analysis of the height, shape, and area of the peaks in the chromatogram.

The chromatographic process and the principle of a GC can be explained further with Figure 4-1. The horizontal lines represent the length of the column, and the vertical direction represents time. Each horizontal line is a stage of the process at different time. The instantaneous signal of the detector is displayed in the boxes, and time trace of it is plotted as the chromatogram in the right. So at the beginning, a sample consisting of two components — A and B — is injected, vaporized and pushed through the column by carrier gas. When they flow through the column, they can exist in two phases: mobile phase in the carrier gas, shown as the peaks above the line, and a stationary phase inside the column coating material, shown as the peaks below the line. Component B has a larger partition coefficient in the stationary phase, which is represented as a larger portion of the peak below the line than component A. Since the mobility in stationary phase is lower than in mobile phase, component B moves at a slower migration speed down the column than component A. Given enough column length and time of flow, the two components will be separated from each other completely as they pass the column, as shown in the third line. Eventually, components A and B will exit the column sequentially, separated both spatially and temporally. They enter the detector and generate two peaks shown on the chromatogram trace at their elution time.

A complete capillary column GC instrument consists of three major components: an injector, a column, and a detector. A diagram of the configuration of a typical GC system is shown in Figure 4-2. All of the three components are crucial for the performance of a GC system, to achieve optimal analysis capacity, sensitivity, and speed. The most often used carrier gases include nitrogen, hydrogen, and helium. In the case of field application, air is also used. The injector is a section of heated tubing to vaporize the injected liquid sample and let the carrier gas push the sample into the column. Various injection modes such as split, splitless, and on-column injection, are applied on capillary GC, using different configurations of flow paths. In order to obtain optimal analysis result, the injection method has to be chosen according to the type and amount of sample to be analyzed.

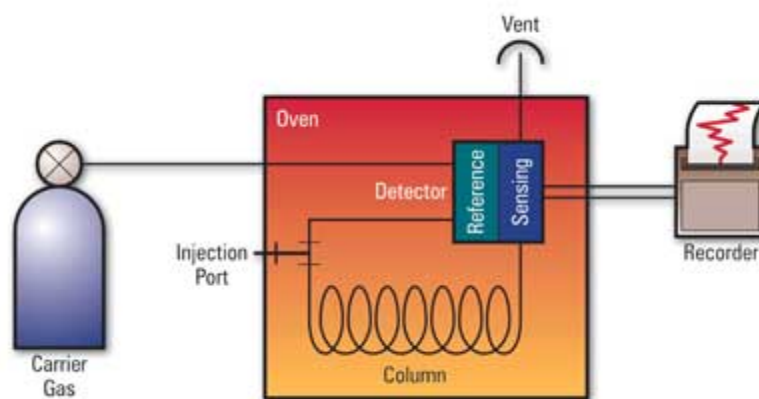


Figure 4-2 Instrument diagram of a GC (from www.practicingoilanalysis.com)

Two types of column are commonly used in modern GC systems: packed and capillary. Pack columns are usually made of stainless steel or glass, filled tightly with liquid stationary phase coated inert solid support material. They are easy and cheap to make, and allow for a larger amount of sample to be injected. Capillary columns are most

often made of fused silica capillary tubes with an inner diameter typically of 100–250 microns. Unlike packed columns, capillary columns are not filled but are open tube with liquid stationary phase coated on the tube walls. They can be made much longer than pack columns, and have higher analysis efficiency and capability.

Frequently used detectors in GC include the flame ionization detector (FID), thermal conductivity detector (TCD), photoionization detector (PID), electron capture detector (ECD), and mass spectrometer (MS). FID and MS are the most widely used among the total of more than 60 different detectors. Put briefly, FID uses a small oxy-hydrogen flame to burn the column effluent, producing some ions in the process. The amount of ions that can be generated in the flame is proportional to the carbon content of the chemical, as quantified using effective carbon numbers (ECN) for various organic compounds. The ions are collected by electrodes under a large bias voltage and form a small current as the signal. Since all organic compound analytes are burnt in the detector, FID is a destructive detector, detecting the total mass flow rate of the analytes.

All the experiments described in this thesis are conducted with a Hewlett-Packard 5890 GC system, using a 100 μm inner diameter capillary column and an FID detector. Hydrogen is used as the carrier gas, because the best separation can be achieved at a higher flow rate than helium or nitrogen so that a higher analysis speed can be obtained.

4.2 NEMS mass sensor in ambient condition

NEMS resonators have been demonstrated as a mass sensor with unprecedented mass sensitivity when their resonance frequency is measured upon the change of their inertial mass^{8,9}. The frequency-mass responsivity of a resonating inertial mass sensor is given by:

$$R = \frac{1}{2\pi} \frac{\partial \omega_0}{\partial M_{eff}} = -\frac{f_0}{2M_{eff}}. \quad (4.1)$$

This expression shows that the minuscule effective mass and high resonance frequency of NEMS account for their very high mass sensitivity, orders of magnitude higher than traditional gravimetric mass sensors such as quartz crystal microbalance (QCM), surface acoustic wave (SAW) and flexural plate wave (FPW) devices. The recent mass sensing milestone was achieved using ultrahigh frequency (UHF) NEMS resonators, demonstrating 100 zeptogram scale mass with a resolution of only 7 zeptogram⁸. The experiment was done at cryogenic temperatures and in an ultrahigh vacuum environment. Physi-sorption of xenon gas on the NEMS surface at low temperature was utilized to accrete the calibrated amount of mass onto the NEMS.

As described in Chapter 2, high frequency nanoscale cantilevers retain their quality factor even at atmospheric pressure and room temperature, which allows high precision measurement of their resonance frequency change. Thus, using them as mass sensors at ambient conditions becomes possible, enabling many applications (such as chemical gas sensing). Since physi-sorption is not possible at room temperature, chemisorption is needed to allow the accretion of mass on the device. The surface of NEMS

devices need to be functionalized with adsorptive materials to enable efficient adsorption or absorption of interested chemical species.

As shown in Figure 4-5, we demonstrate attogram scale mass sensing with nanocantilevers in ambient conditions, namely room temperature and atmospheric pressure. We achieve this by functionalizing the device surface with a thin polymer film having a high partition coefficient for the species of interest. To maintain the nanoresonator's quality factor and frequency, this film must be extremely thin. For our initial demonstration we employ polymethyl methacrylate (PMMA), which forms a very thin, conformal layer without the need for elaborate surface treatments. The NEMS devices are spin coated at 4000 rpm with a solution of 0.5 wt % 495 K PMMA in anisole. The resulting polymer film thickness is approximately 10 nm, as is confirmed by both atomic force microscopy and careful measurement of the change in resonance frequency arising from mass loading by the coating after its application. A decrease of only 20–30% in the resonance quality factor is typically observed after application of a layer of 1–10 nm coating. In Figure 4-3, such a coating process is illustrated, showing the cases of both unsuccessful and successful coating. The frequency shift due to the added mass of PMMA coating can be readily measured and used to calculate the film thickness. Figure 4-4 shows the resonance response of a typical cantilever before and after the coating process. Atmospheric pressure mass sensing measurements are carried out on two typical cantilevers operating at resonance frequencies of 8 and 127 MHz (Figure 2-5's cantilevers c and d). The mass responsivities of the two devices used in these experiments are calibrated by separate low temperature physi-sorption experiments using a controlled

flux of xenon atoms. We obtain values of 7 Hz/ag and 0.68 Hz/zg respectively, in good agreement with our predictions from finite element analysis.

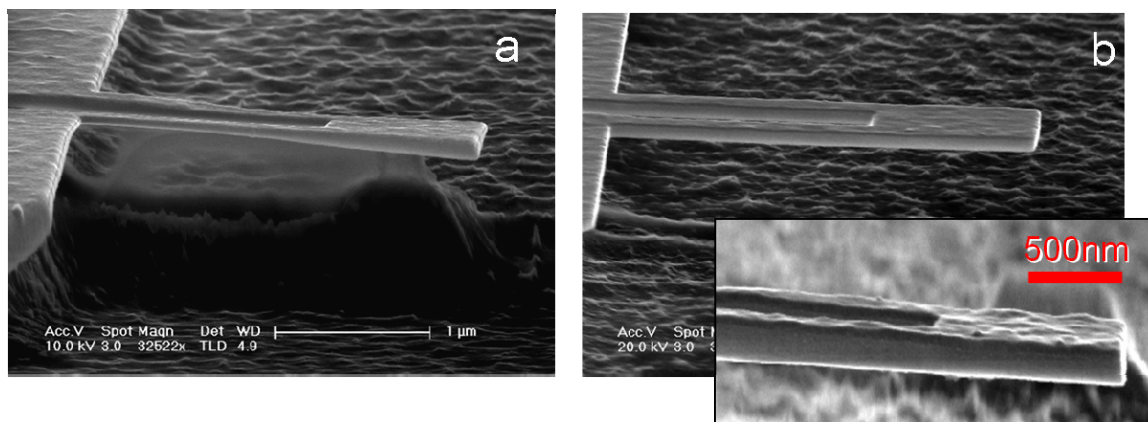


Figure 4-3 Coating cantilever resonators with polymer: a) a too thick layer of polymer glues the cantilever down to the substrate and prevents its oscillation; b) optimal coating of the cantilever with very thin polymer

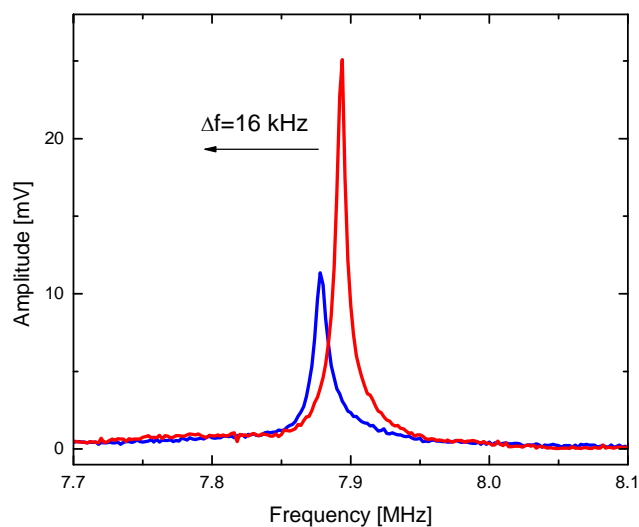


Figure 4-4 Frequency shift and quality factor reduction of the resonance response of the cantilever before (red) and after (blue) coating

In separate experiments, these devices are exposed to a series of 1,1,-difluoroethane ($C_2H_4F_2$, hereafter DFE) gas pulses at room temperature and atmospheric pressure. These devices are read out using a computer-controlled phase-locked loop (PLL), which allows us to excite and track the nanocantilevers' resonance frequency in real time. Our setup enables tracking the resonance frequency of cantilevers in air with a precision better than 10^{-6} (1 ppm) using a time constant of 100 milliseconds. In response to each pulse, the resonance frequency of the cantilevers first decreases rapidly during the injection of gas, then recovers when the injection is completed, as the adsorbed gas species slowly desorb from the coating (Figure 4-5). This reversible adsorption-desorption process carried out under ambient conditions yields temporal “dips” of frequency shift, instead of the “steps” seen in the low temperature UHV physi-sorption experiments. Increasing the DFE pulse length yields progressively higher peak mass adsorption of DFE, as is reflected in the increasing mass response dips. Since the time constant of the frequency tracking phase-locked loop (PLL) circuitry is set to be 100 milliseconds, the response and recovery time are limited only by the dead volume of the testing chamber. With the 8 MHz cantilever, we are able to resolve mass accretion peaks as small as 10 ag in real time, with mass noise floor ~ 1 ag. With the 127 MHz cantilever, we achieve the highest mass resolution, estimated to be ~ 100 zg, allowing mass peaks of 1 ag to be resolved (Figure 4-5).

Theoretically, mass resolution is given by the expression $\delta M \sim (M_{eff} / Q) \cdot 10^{-DR/20}$. The 127 MHz cantilever has effective mass $M_{eff} = 100$ fg, dynamic range DR=80 dB, and quality factor $Q \sim 400$ in air. Using these values, we expect a mass resolution of ~ 25 zg at room temperature. Environmental fluctuations —

which include those of temperature, pressure, humidity, etc. — apparently degrade our resolution to the observed value of ~ 100 zg, which is only a factor of four away from ideal performance.

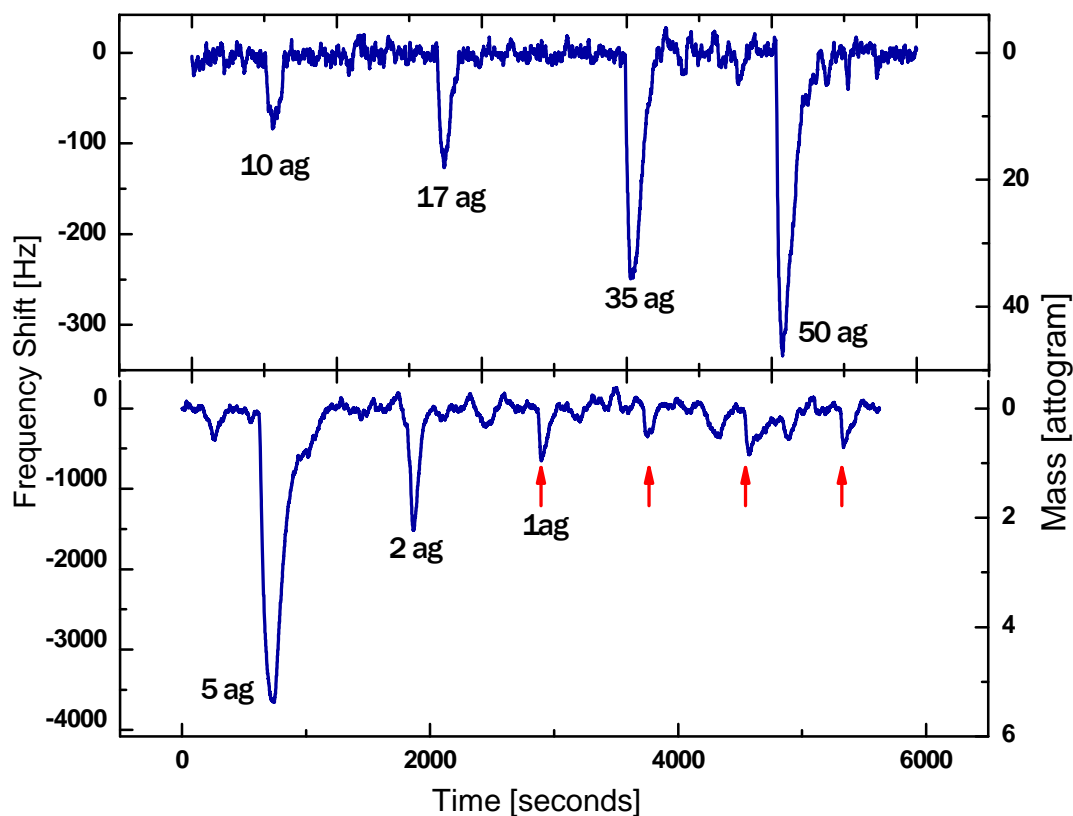


Figure 4-5 Real-time NEMS chemisorption measurements. 1,1-difluoroethane gas molecules are chemisorbed onto the polymer-coated surfaces of two separate nanocantilever devices. The measurements are carried out in air, at atmospheric pressure and room temperature. The top and bottom traces are measured with 8 MHz and 127 MHz nanocantilevers (Figure 2-5's cantilever c and d), respectively. The minimum resolvable mass is below 1 ag (red arrows)

4.3 Polymeric film functionalized NEMS detector in GC

When using gravimetric sensor for gas concentration sensing, instead of absolute mass sensitivity, it is more sensible to use areal mass sensitivity, the mass sensitivity normalized by available device area. This is necessary simply because a larger device has larger surface area to adsorb more mass than a smaller device. The conversion from unprecedented absolute mass sensitivity of the NEMS resonator to an equivalent chemical sensing sensitivity can be justified by examining the Sauerbrey equation of areal mass sensitivity:

$$S_m = \frac{RA_{eff}}{f_0}. \quad (4.2)$$

Here R is the mass responsivity as defined in equation (4.2), A_{eff} is the effective surface area of the device available for adsorption of mass, and f_0 is the resonance frequency. If equation (4.1) is plugged into, it can be written as:

$$S_m = \frac{A_{eff}}{f_0} \left(-\frac{f_0}{2M_{eff}} \right) = -\frac{A_{eff}}{2M_{eff}} \propto \frac{1}{\rho t_{eff}}. \quad (4.3)$$

Here ρ is density of the device material and t_{eff} is the effective thickness of the device.

This relation shows that the areal mass sensitivity is inversely proportional to the thickness of the device. It can be exemplified by the improvement of flexural plate wave devices (FPW) from bulk acoustic wave (BAW) and surface acoustic wave (SAW) devices. In BAW and SAW devices, the effective thickness is the operational acoustic wave length in the devices, on the order of hundreds of microns. While in FPW, since the thickness of the plate is thinner than the acoustic wave length, the actual device thickness, which can be made below 100 micron, is taken as effective thickness. Thus better areal

mass sensitivity can be obtained with FPW. NEMS resonators have much lower thickness than all of these acoustic wave devices. For example, the nanoscale cantilevers described in this thesis have a typical thickness of only 100 nm. Thus, as indicated in Table 4-1, several orders of magnitude of improvement in areal mass sensitivity can be achieved.

Table 4-1 Comparison of areal mass sensitivity of various acoustic devices and NEMS resonators

Sensor	Theoretical S_m (cm ² /g)	Typical S_m (cm ² /g)
Bulk acoustic wave	$-n/\rho\lambda$	-14
Surface acoustic wave	$-K(\sigma)/\rho\lambda$	-10 – -100
Flexural plate wave	$-1/2\rho d$	-400 – -1000
NEMS – nanocantilever 8MHz ~ 127 MHz	$-1/\rho t$	-8000 – - 100000

Polymeric thin films have been widely used as adsorptive materials for various gas sensing applications. Analyte gas molecules are absorbed and diffused into polymeric film until equilibrium is reached. The different chemical interaction forces between different types of gas molecules and the polymer gives the selectivity of a particular polymer. This can be quantified using the partition coefficient K_c . K_c is a thermal equilibrium constant, and is defined as the ratio of analyte volume concentration in gas phase c_{gas} to that inside the polymer film c_{poly} :

$$K_c = \frac{c_{poly}}{c_{gas}} . \quad (4.4)$$

Typical values for K_c for a particular polymer-gas combination can be in the range of 1000–1,000,000. The polymer film will have large selectivity for one analyte gas with large K_c over another analyte gas with low K_c . K_c is also a strong function of temperature and the analyte vapor pressure. Thus, the polymer material can be chemically engineered to target a specific chemical group of gas analytes, to achieve selective sensing with a very low false-alarm rate. For example, a hydrogen-bond acid polymer named DKAP is developed by the Sandia National Laboratory for detection of phosphonate gas molecules, which are precursors and simulants of nerve gas agents. The partition coefficient between DKAP and dimethyl methylphosphonate (DMMP) can approach 1,000,000, while it is very small between DKAP and common alkenes. So DKAP has excellent selectivity toward interested nerve gases.

We used solution evaporation method to coat the cantilever devices with DKPA polymers. A droplet of DKAP solution in toluene with concentration of 0.05mg/ml is put on the device chip. After the solvent evaporates, thin film of polymer with thickness about 10 nm forms on the surface. This method has poor control of film uniformity, but is very simple and still has very high yield. To improve the coating uniformity and prevent coating the substrate, other novel methods with more complexity are possible, including microspray, electrochemical methods, and self-assembly techniques.

An integrated microscale gas analyzer (MGA) includes a microscale injector/pre-concentrator, separation column, and detector. The functionality of the first two components has been demonstrated and is under development in many groups, including the Sandia National Laboratory^{5,10-12}. Before testing a fully integrated system, the functionality of a NEMS-based detector is evaluated using a traditional GC system. We thus set up a commercial GC system (Hewlett-Packard 5890), and tested the NEMS detectors with it, at Sandia initially and later at Caltech. The device is housed in a flow cell, and connected to the outlet of GC column. The original FID detector of the system is connected in serial after the NEMS. A diagram of the experiment setup is shown in Figure 4-6.

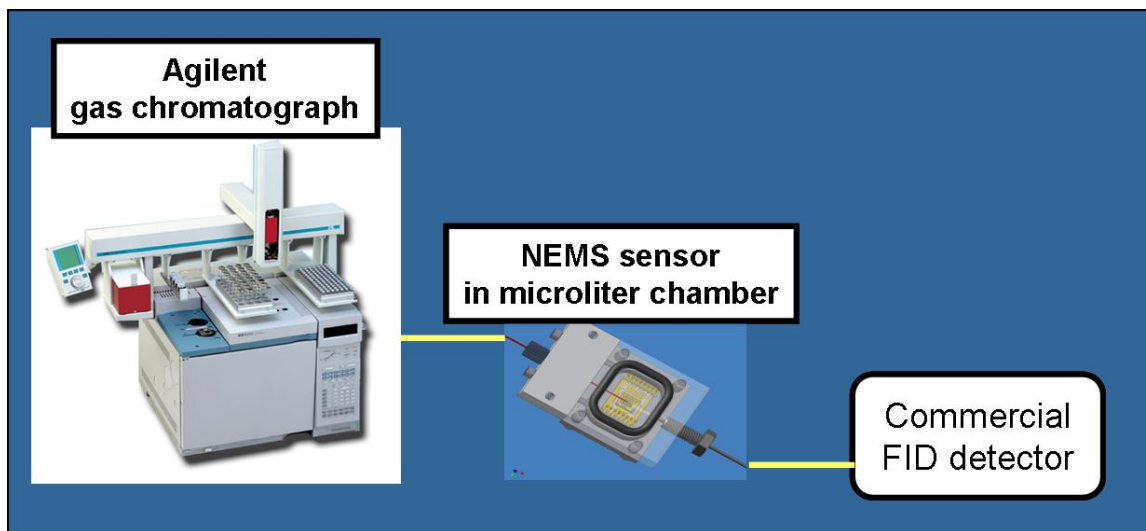


Figure 4-6 Setup to test NEMS detector with commercial GC system with FID detector connected in serial

The minimized volume of the flow cell is crucial in order to reduce the dead volume, or hold-up volume, of the whole system. Large dead volume can cause

broadening in the chromatographic peaks and deteriorate the analysis capability of the system. This becomes more essential for a GC system working at a very fast speed such as in the microscale gas analyzer, which requires total analysis time to be only a few seconds. Thus, reducing the unnecessary dead volume of the system is crucial to obtaining optimal analysis performance. For example, a benchmark of the microscale gas analysis system requires 25 analysis channels (defined as the number of resolvable peaks in predefined time) within 4 seconds, which is equivalent to a maximum peak width of 160 milliseconds. At a typical column flow rate of 1 ml/min, the hold-up volume of the system needs to be smaller than 2.67 microliters.

Initially, a flow cell is designed with volume of 50 microliters. The NEMS device is housed inside the cell. A 10 meter long column is used, GC oven temperature is at 50 °C, and inlet pressure is at 50 PSI. The device assembly is placed inside the oven. Samples containing mixture of various analytes in carbon disulfide (CS₂) solution are tested. Tested chemical analytes include both chemical warfare agent simulants and some interferents. Their names, formulas, densities, and molecular weights are listed in Table 4-2. In Figure 4-7 and Figure 4-8, the chromatograms obtained during this first successful demonstration of the NEMS detector in a GC system are shown.

In Figure 4-7, 1 µl of sample containing equal concentration (1% v/v) of DMMP, DIMP, DEMP and MS in CS₂, together with ten times higher concentration (10% v/v) of 3-MH, is injected into the system. Chromatographic traces from both NEMS (purple) and FID detector (blue) are displayed. Although 3-MH concentration is ten times higher than

other analytes, its corresponding peak only appears in the FID signal as the largest one adjacent to the solvent peak (see inset). The large FID response to 3-MH is because of its large equivalent carbon number (ECN). However, this peak is completely absent in the NEMS signal trace. This indicates that the DKAP coating polymer has very low adsorption of 3-MH. A more complicated mixture of all of the fifteen analytes is then injected, and chromatogram traces are obtained as shown in Figure 4-8. Similar selectivity of NEMS detector to other interferences can be observed. Successful separation of typical CWA simulants including DMMP, DIMP, DEMP, DCP, and MS is achieved and clearly visible as separated peaks on the NEMS frequency shift signal trace. However, even with this 10 meter long column and an analysis time longer than 10 minutes, those analytes are not baseline separated from each other. Each peak, both in NEMS and FID traces, is severely broadened with extra long tailing. In fact, in an attempt to do faster separation of only DMMP and solvent when using a one meter long column, poor separation can be achieved within a 30 second analysis time, as shown in Figure 4-9. Also, those NEMS traces show poor resolution with low signal to noise ratio, indicating a reduced limit of detection. These problems are mainly caused by the substantially large dead volume of the 50 microliter chamber used to house the NEMS chip. By reducing the chamber volume further, both improved separation ability and limit of detection of the system can be obtained.

Table 4-2 List of tested chemicals and their formulas, densities, and molecular weights (MW), including CWA simulants (*) and interferents

No.	Symbol	Formula	Density (g/ml)	MW	Full name
1	3MH	$\text{CH}_3\text{CH}_2\text{CH}_2\text{CH}(\text{CH}_3)\text{CH}_2\text{CH}_3$	0.687	100.20	3-methylhexane
2	TOL	$\text{C}_6\text{H}_5\text{CH}_3$	0.865	92.14	Toluene
3	C8	$\text{CH}_3(\text{CH}_2)_6\text{CH}_3$	0.703	114.23	Octane
4	DMMP*	$\text{CH}_3\text{P}(\text{O})(\text{OCH}_3)_2$	1.145	124.08	Dimethyl methylphosphonate
5	C7OH	$\text{CH}_3(\text{CH}_2)_5\text{CHO}$	0.817	114.19	Heptanal
6	2-CEES*	$\text{ClCH}_2\text{CH}_2\text{SC}_2\text{H}_5$	1.07	124.63	2-Chloroethyl ethyl sulfide
7	C8OH	$\text{CH}_3(\text{CH}_2)_6\text{CHO}$	0.82	128.21	Octanal
8	DEMP*	$\text{CH}_3\text{P}(\text{O})(\text{OC}_2\text{H}_5)_2$	1.041	152.13	Diethyl methylphosphonate
9	DCP*	$(\text{C}_2\text{H}_5\text{O})_2\text{P}(\text{O})\text{Cl}$	1.194	172.55	Diethyl chlorophosphate
10	DNBS*	$\text{CH}_3(\text{CH}_2)_3\text{S}(\text{CH}_2)_3\text{CH}_3$	0.838	146.29	di-n-butyl sulfide
11	DIMP*	$(\text{C}_3\text{H}_7\text{O})_2\text{P}(\text{O})\text{CH}_3$	0.976	180.18	Diisopropyl methylphosphonate
12	C11	$\text{CH}_3(\text{CH}_2)_9\text{CH}_3$	0.74	156.31	Undecane
13	DCH*	$\text{Cl}(\text{CH}_2)_6\text{Cl}$	1.068	155.07	Dichlorohexane
14	NAPTH	$\text{C}_{10}\text{H}_7\text{OH}$		144.17	1-Naphthol
15	MS*	$2\text{-(HO)C}_6\text{H}_4\text{CO}_2\text{CH}_3$	1.174	152.15	Methyl salicylate

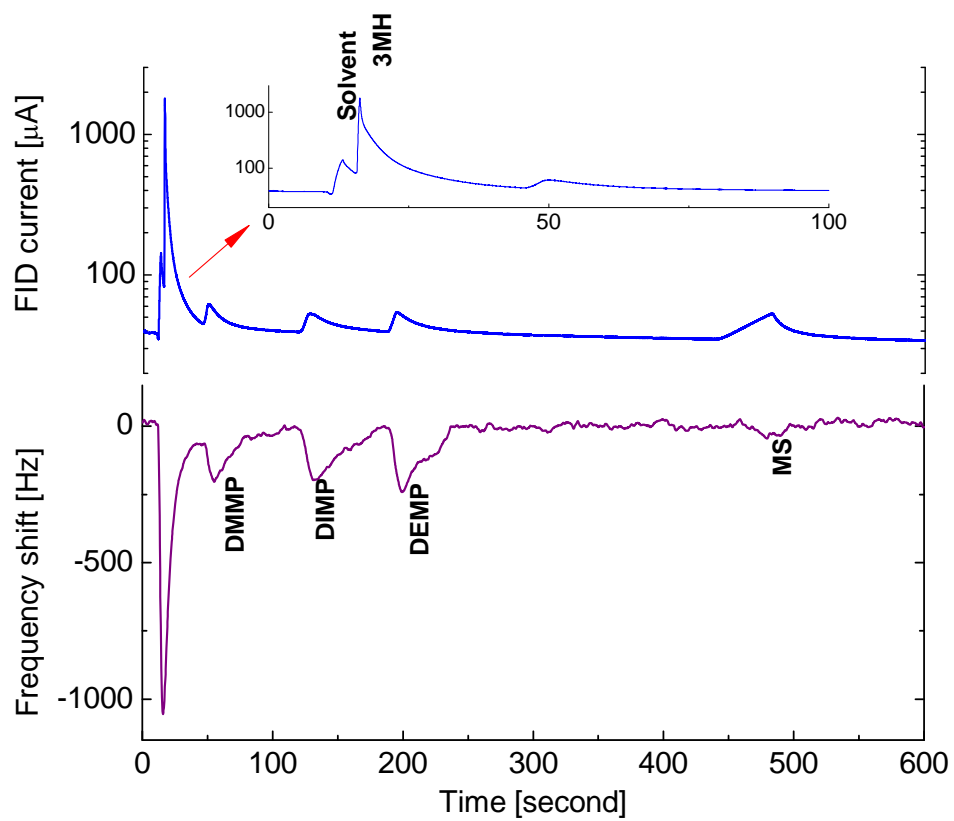


Figure 4-7 Gas chromatogram from NEMS detector (purple) and FID detector (blue), showing peaks from five analytes (3MH, DMMP, DIMP, DEMP, MS) with similar concentration

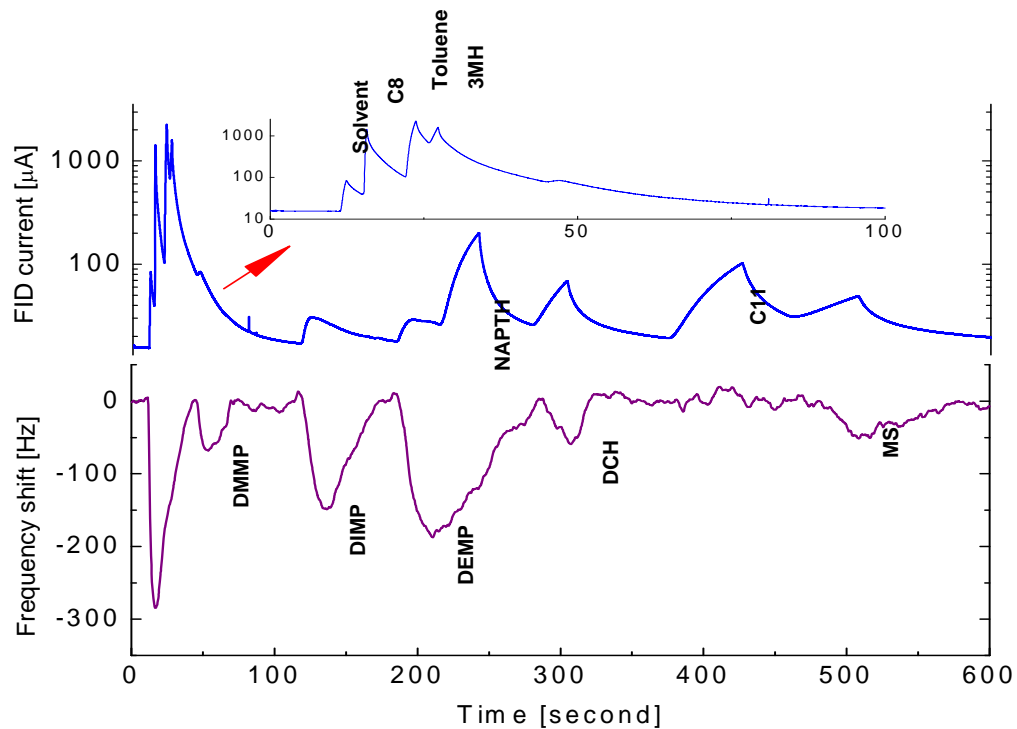


Figure 4-8 Gas chromatogram from NEMS detector (purple) and FID detector (blue), showing peaks from ten analytes (C8, Toluene, 3MH, DMMP, DIMP, DEMP, DCH, NAPTH, C11, MS) with similar concentration

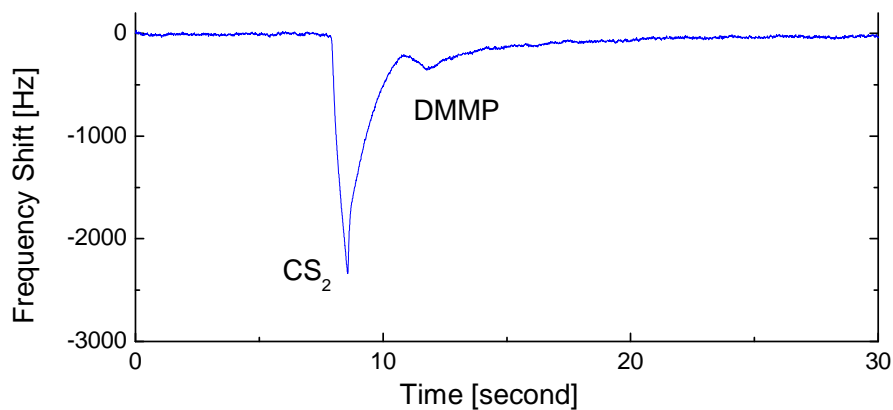


Figure 4-9 Faster GC separation with 1 meter long column

To further reduce the dead volume of the system, a micro-machined flow chamber using a microfluidic formation is designed and made. A 20 micrometer deep and 2.5 millimeter long channel is etched between inlet/outlet holes on a glass chip. Thus the total volume of this flow cell is defined by the channel, which has a volume of only 15 nanoliters. Then, instead of the previous flow cell configuration which puts the device chip inside the flow chamber, the glass lid/channel is assembled on top of the device chip and sealed with vacuum epoxy. Two pieces of capillary tubing with 100 micron inner diameter are inserted into the holes to allow inlet and outlet gas flow. A diagram and photo of such an assembly is shown in Figure 4-10.

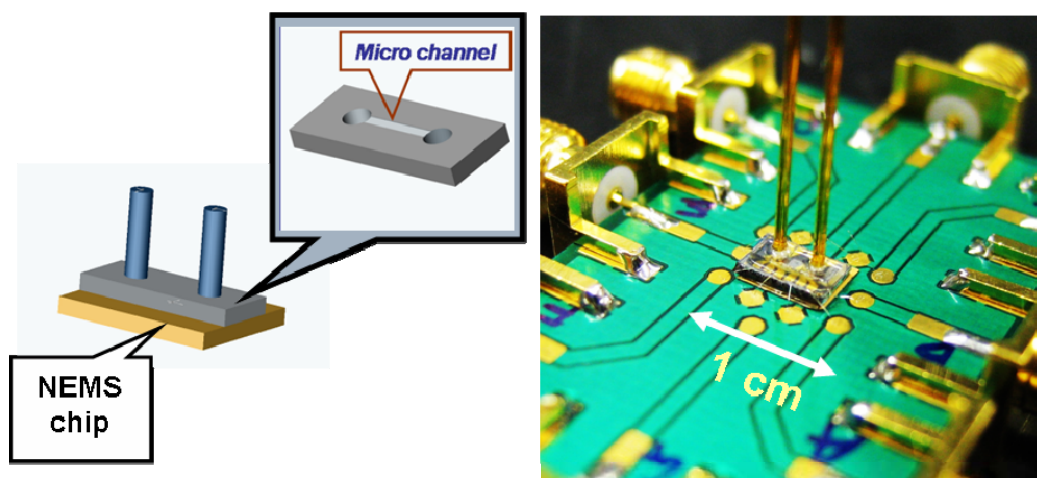


Figure 4-10 Micro-machined flow chamber with microfluidic flow channel and the assembly with NEMS device chip. Total channel volume is only 15 nanoliters.

Remarkable improvement of the system performance is achieved immediately after using the nanoliter volume assembly. Figure 4-11 shows chromatograms obtained at very fast speed. A one meter long column is used, and fast temperature programming is employed to further improve the speed and separation. To do that, an on-column heater

made of Ni-Cr wire, is wound around the column. The heater can provide a heating ramp of about 20 °C/sec when 20 V heating voltage is applied at the moment when the sample is injected. Very good separation can be achieved within the analysis time of only a few seconds. To acquire the first chromatogram in Figure 4-11, 1 µl of sample containing a solution of five simulants (DMMP, DEMP, DIMP, DCP, MS) in CS₂ solvent is injected. They can be successfully baseline separated as indicated by the individual sharp peaks in both the NEMS and FID signal traces. In the second chromatogram, sample containing thirteen analytes (excluding 3-MH and NAPTH in Table 4-2) is injected. Although baseline separation of all analytes is not achieved, nine analytes can be clearly identified from the chromatogram. Some analytes (CEES, DNBS and Undecane) are missing in the chromatogram, due to the adjacent large peaks with broader width which cover the peak from these analytes with smaller response. The fastest analyte peak (DMMP) shows a full width at half maximum (FWHM) of less than 100 millisecond, indicating a channel number of more than forty at this condition.

Another important feature of the polymer coated NEMS sensors is their chemical selectivity to different analytes, as determined by the interaction of the analyte and the coating polymer. In comparison, the FID detector is not very selective, with its response proportional to the equivalent carbon number (ECN) of the analyte only. The DKAP polymer (Figure 4-12) has a strong hydrogen bond and is designed to be selective to organophosphonate chemicals, such as DMMP and DIMP. This selectivity can be clearly seen from the second chromatogram in Figure 4-11, as the largest peaks corresponding to toluene and octane in the FID signal are completely absent in the NEMS signal. But the

NEMS signal shows strong response to other organophosphonates. It indicates the strong selective of DKAP polymer for organophosphonates to alkenes and toluene. In Figure 4-12, the relative responses of DKAP-coated NEMS and FID detectors to all tested analytes are plotted. The strong selectivity of DKAP to DMMP, DEMP, and DIMP is clear as the protrusion point toward them; FID is not very selective showing a more isotropic distribution of data points.

The selectivity of the detector is very important in improving the analytical capability of the microscale analysis system, since at a very fast analysis speed and microscale dimension, baseline separation of large number of analytes is challenging and many analytes may co-elute. Using a selective detector relaxes the demand for separation, as two overlapped analyte peaks that can not be resolved with a nonselective detector can be detected by two detectors with strong selectivity for each of them respectively. Ideally, two completely chemically orthogonal detectors will double the resolvable channel number of the system. Although chemically orthogonal coating is difficult to realize, a set of different coatings with less degree of chemical orthogonality still will improve the analysis capability of the system by using some pattern recognition algorithm. Because of the separation of the column, such an algorithm will be much simpler than those needed for the proposed system using bare sensor arrays^{13,14}.

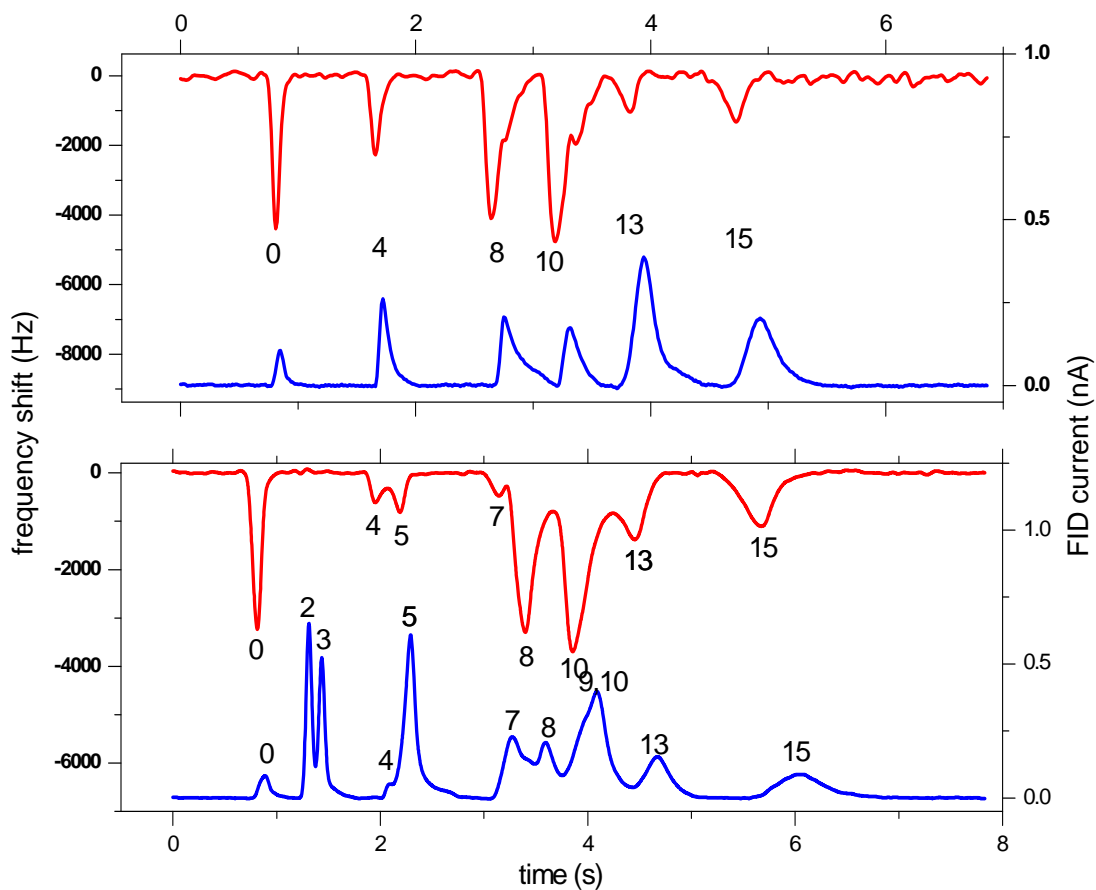


Figure 4-11 Very fast GC chromatogram from both NEMS (red) and FID (blue) detectors, obtained using nanoliter volume chamber. Top graph shows chromatogram acquired from sample solution of five different analytes, and bottom chromatogram is obtained from sample solution of thirteen different analytes. Each analyte peak is identified with the number listed in Table 4-2.

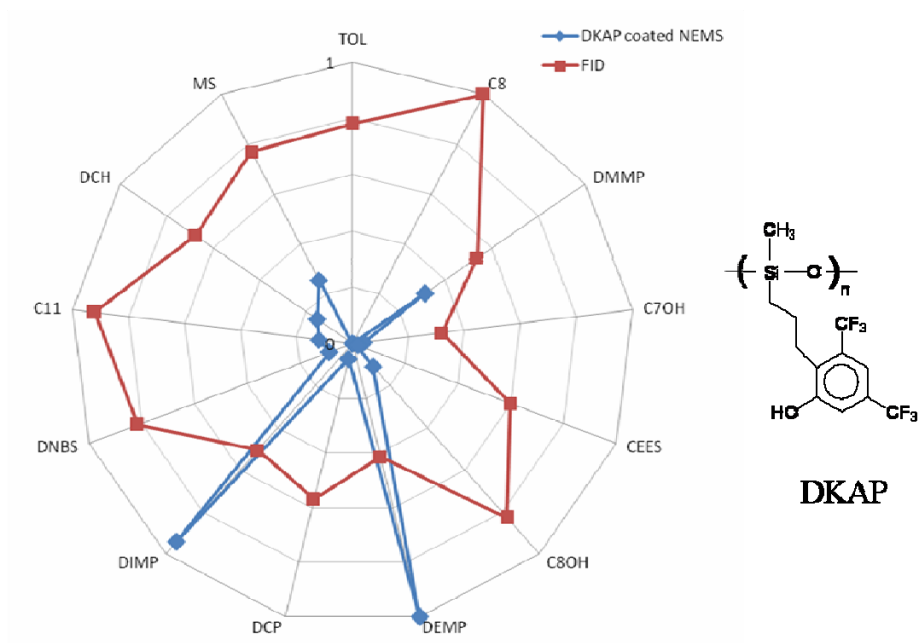


Figure 4-12 Relative response of DKAP-coated NEMS and FID detectors to various analytes

A different polymer, poly-caprolactone (PCL), is tested to determine the extent of difference between its selectivity and that of DKAP polymer. Chromatograms are acquired using cantilever resonators coated with DKAP and PCL respectively, as shown in Figure 4-13. Their relative response of different analytes is plotted in Figure 4-14. Apparently, the PCL polymer shows no difference in chemical selectivity from the DKAP polymer. But it shows a different distribution of responses among test analytes, which gives additional information that can be used to analyze the sample.

There are several dozen commonly used sensitive polymer coatings for gas sensing. It still remains to find the optimal combination which provides the best orthogonality for different applications involving different types of targeted analytes.

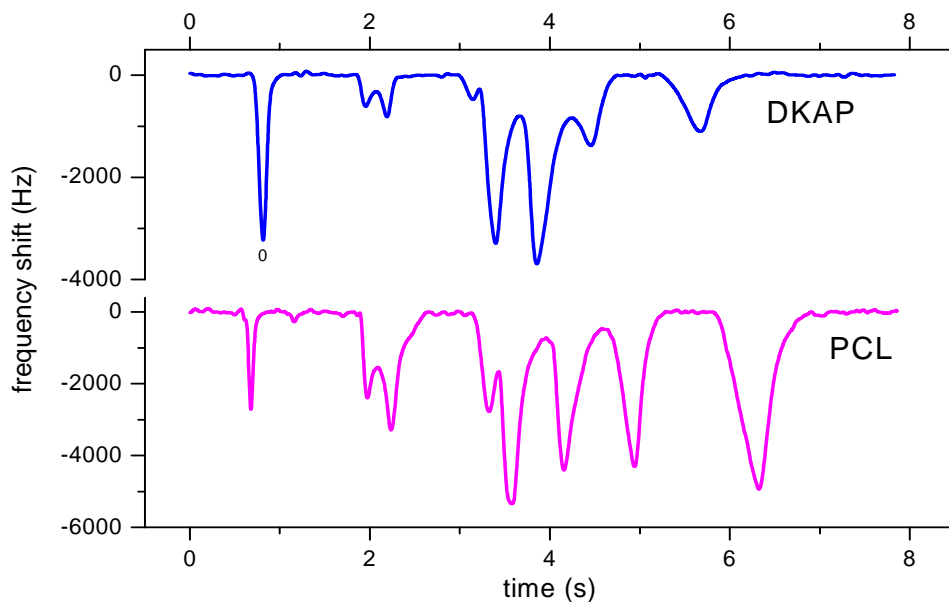


Figure 4-13 Chromatogram of thirteen analytes from cantilever resonators coated with DKPA and PCL polymer, respectively, acquired in different runs

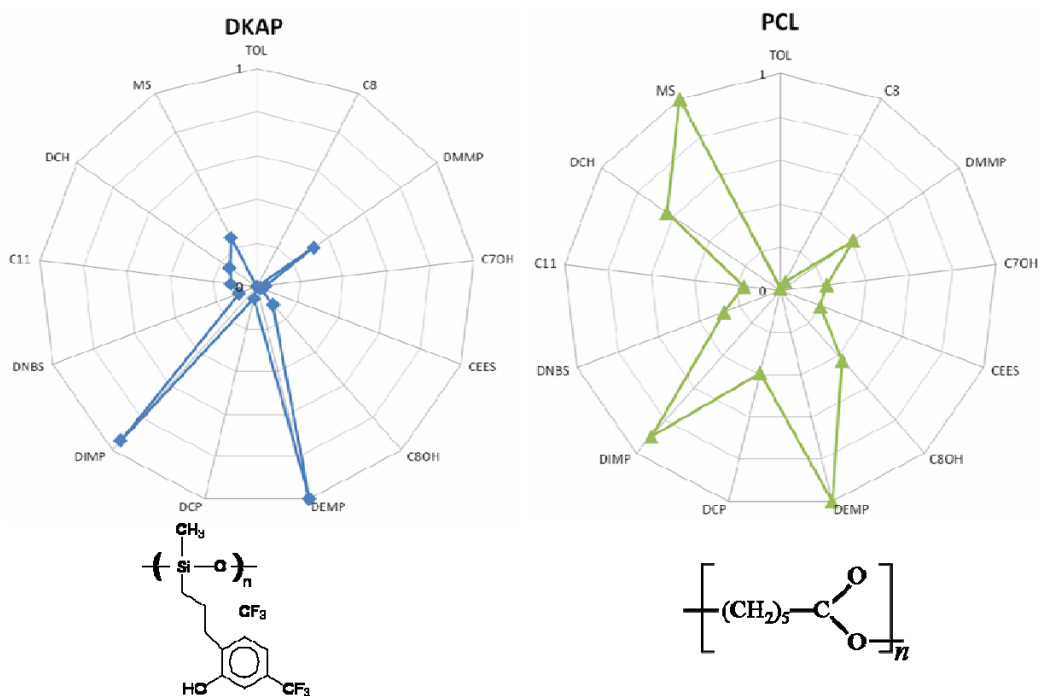


Figure 4-14 Relative response of DKAP- and PCL-polymer coated NEMS to various analytes

The limit of detect (LOD) of the NEMS detector can be determined by measuring the response at various analyte concentrations, and then extrapolating to the frequency readout noise floor to find out the corresponding lowest concentration. However, in a gas chromatography measuring system, constant concentration cannot be generated; instead the effluent of analytes in carrier gas with time-varying concentrations exits the column. By using the mass concentration in injected sample solution, the flow rate in the column and split line, and measuring the peak width, the averaged concentration within the peak can be determined. In this way, by varying the concentration in the sample solution, various averaged concentrations in the gas phase of the column effluent can be generated. The NEMS detector response in frequency shift is then measured at various averaged concentrations, as shown in Figure 4-15. Two sets of data of NEMS response to DIMP are obtained using 10 meter and one meter long columns. When using the 10 meter long column, the analyte peak shows a typical width of 600 seconds, while the 1 meter column generates peaks with a width of about 1 second. At slow separation speed with longer peak width, the LOD can be determined as better than one part-per-billion (ppb). However, when the separation speed is increased with the 1 meter column, the sensitivity of the NEMS detector is dramatically reduced. As shown in Figure 4-15, with a 1 second peak width, the sensitivity is decreased by a factor of 300, giving a LOD of about 300 ppb. The concentration sensitivity of the NEMS detector is traded for improved speed. This effect is due to the slower diffusion speed of the gas phase into the polymer phase, so that the polymer coating film takes a relatively longer time to reach equilibrium with the gas phase concentration and give the maximum possible response from the detector. Thus, the faster the separation speed with the shorter peak width, the less response the

detector outputs. A similar problem was seen previously — large chamber size reduces sensitivity too, but it can be improved by using a smaller chamber with a volume of only nanoliters. But since the diffusion constant of gas molecules in the polymer phase is orders of magnitude smaller than that in gas phase, the corresponding time constant is much longer.

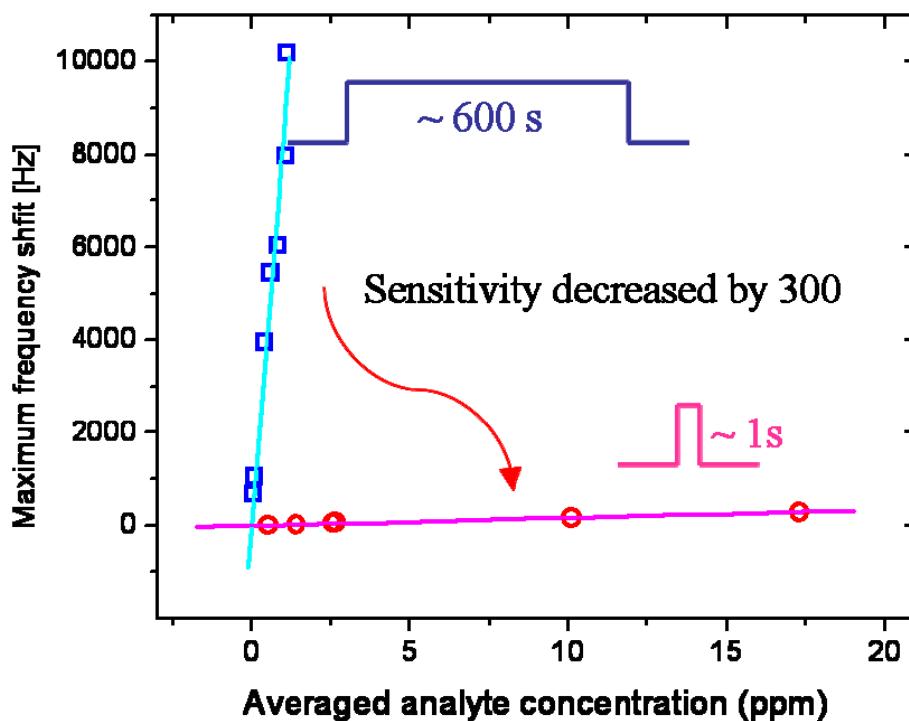


Figure 4-15 Maximum NEMS detector frequency shift at various DIMP concentrations. Two sets of data obtained using slow and fast GC separation are plotted, showing reduced sensitivity at high separation speed.

This diffusion problem can be manifested qualitatively by solving the diffusion equation in polymer phase:

$$\frac{\partial c}{\partial t} = D \frac{\partial^2 c}{\partial x^2}. \quad (4.5)$$

Two boundary conditions are:

$$\partial c / \partial t = 0 \text{ at } x = 0 \text{ (i.e., no diffusion beyond the substrate)} \quad (4.6)$$

and

$$\begin{aligned} c(L, t) = c_0 \text{ for } t > 0 \\ \text{(i.e., concentration at the polymer-gas interface is constant)} \end{aligned} \quad (4.7)$$

If c_0 is constant, Equation (4.5) can be solved to give an analytical solution for the total amount of mass of absorbed gas molecules as¹⁵:

$$m(t) = m_{\max} \left[1 - \frac{2}{\pi^2} \sum_{n=1}^{\infty} \frac{\exp\left(\frac{-\pi^2 (n - 1/2)^2}{L^2} Dt\right)}{(n - 1/2)^2} \right], \quad (4.8)$$

where D is the diffusion coefficient of the gas molecules inside the polymer, L is the polymer film thickness and m_{\max} is the maximum accumulated mass inside the polymer film at $t \rightarrow \infty$ (i.e., when equilibrium is reached). In Figure 4-16, solution (4.8) is plotted against time with various assumed values of diffusion coefficient D . As clearly seen in the plot, at a very low diffusion coefficient, a very long time is needed for the detector to reach the maximum response. For example, for a diffusion coefficient of 10^{-16} cm²/s, 1000 seconds after the start of exposure to the analyte, the response of the detector only reaches 36% of the maximum. After 1 second exposure, the detector only shows 1% of the maximum response. When t is so small that $m(t)/m_{\max} < 0.6$, equation (4.8) can be very well approximated with the square root of t as shown in Figure 4-17. The spatial concentration distribution of the gas molecules inside the polymer coating at various times is plotted in Figure 4-18, further manifesting the absorption process of gas molecules from gas phase to the polymer phase. Fourier number $\tau = t \cdot D / L^2$ is used as the unit of time. More complete solutions to the problem of chemical species diffusion into a thin film can be found in the literature¹⁶.

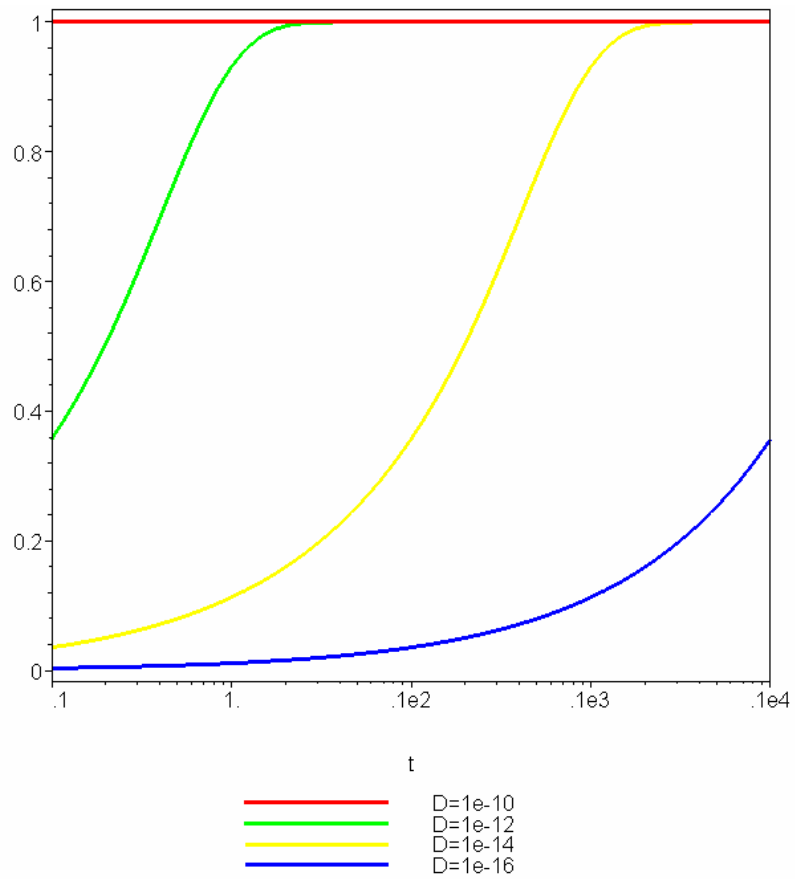


Figure 4-16 Relative response of the NEMS detector with 10 nm thick polymer coating. Various diffusion coefficients of the gas molecules in polymer phase are assumed.

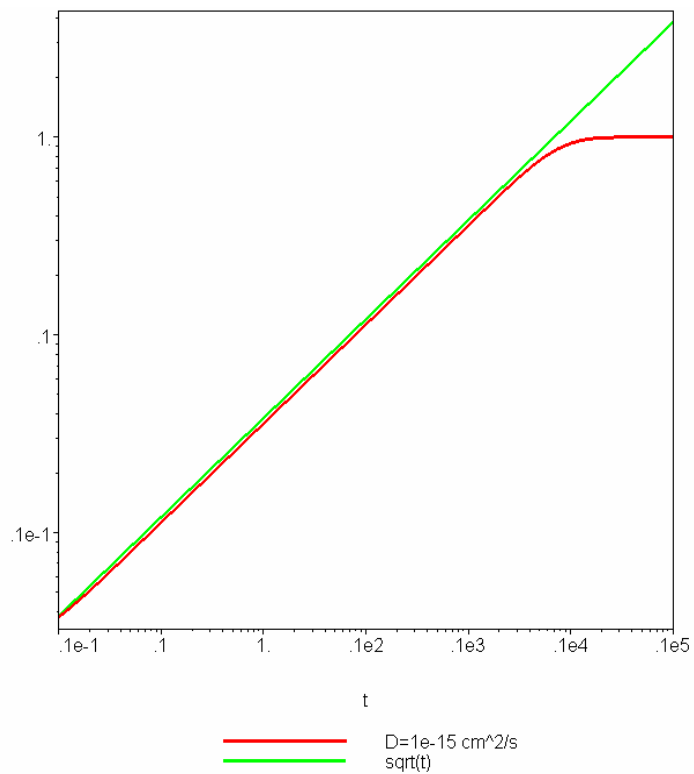


Figure 4-17 The function of equation (4.8) can be approximated using the square root of t when $m(t)/m_{max} < 0.6$.

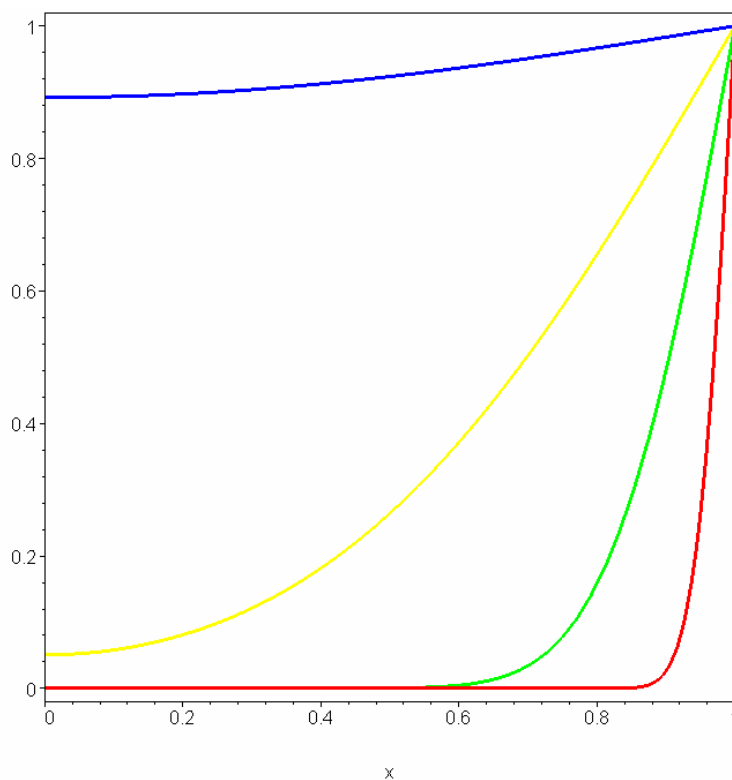


Figure 4-18 Spatial (depth) distribution of gas molecule concentration inside the polymer at various times (0.001, 0.01, 0.1, and 1 τ)

This slow diffusion puts major limitations on detection speed to acquire expected sensitivity. It will be a universal problem for all polymer-coating-based chemical sensors which rely on gas species diffusing into the polymer phase to be transduced to the sensor response. Engineering the properties of the polymer coating to improve the diffusion speed is possible by adding plasticizers into the polymer to turn the film more rubbery. However, in the microscale fast gas analysis system, the application of a pre-concentrating stage can also significantly compensate the loss of sensitivity at increased analysis speed by pre-concentrating the analyte species and then quickly releasing them. Such a system will have unprecedented detection and analysis speed and sensitivity, all implemented at microscale and in integrated formation. Employing both the separation

column and chemically selective detectors, an extraordinary analysis capability of a very complex sample can be achieved in almost real time. Applications in homeland security, environmental monitoring, and disease diagnosis are within reach in the near term.

4.4 Reference

- 1 Dittrich, P. S., Tachikawa, K., and Manz, A. Micro total analysis systems. Latest advancements and trends. *Analytical Chemistry* **78**, 3887-3907 (2006).
- 2 Janasek, D., Franzke, J., and Manz, A. Scaling and the design of miniaturized chemical-analysis systems. *Nature* **442**, 374-380 (2006).
- 3 Thompson, M. and Stone, D. C. Surface acoustic-wave detector for screening molecular recognition by gas-chromatography. *Analytical Chemistry* **62**, 1895-1899 (1990).
- 4 Wohltjen, H. and Dessy, R. Surface acoustic-wave probes for chemical-analysis .2. Gas-chromatography detector. *Analytical Chemistry* **51**, 1465-1470 (1979).
- 5 Agah, M. *et al.* High-speed mems-based gas chromatography. *Journal of Microelectromechanical Systems* **15**, 1371-1378 (2006).
- 6 McNair, H. M. and Miller, J. M., *Basic gas chromatography*. (Wiley, New York, 1998).
- 7 Miller, J. M., *Chromatography : Concepts and contrasts*, 2nd ed. (Wiley, Hoboken, N.J., 2005).

- 8 Yang, Y. T. *et al.* Zeptogram-scale nanomechanical mass sensing. *Nano Lett.* **6**, 583-586 (2006).
- 9 Ekinci, K. L., Huang, X. M. H., and Roukes, M. L. Ultrasensitive nanoelectromechanical mass detection. *App. Phys. Lett.* **84**, 4469-4471 (2004).
- 10 Stadermann, M. *et al.* Ultrafast gas chromatography on single-wall carbon nanotube stationary phases in microfabricated channels. *Analytical Chemistry* **78**, 5639-5644 (2006).
- 11 Tian, W. C. *et al.* Multiple-stage microfabricated preconcentrator-focuser for micro gas chromatography system. *Journal of Microelectromechanical Systems* **14**, 498-507 (2005).
- 12 Lu, C. J. *et al.* First-generation hybrid mems gas chromatograph. *Lab on a Chip* **5**, 1123-1131 (2005).
- 13 Park, J., Groves, W. A., and Zellers, E. T. Vapor recognition with small arrays of polymer-coated microsensors. A comprehensive analysis. *Analytical Chemistry* **71**, 3877-3886 (1999).
- 14 Burl, M. C. *et al.* Classification performance of carbon black-polymer composite vapor detector arrays as a function of array size and detector composition. *Sens. Actuator B-Chem.* **87**, 130-149 (2002).
- 15 Frye, G. C. *et al.* Monitoring thin-film properties with surface acoustic-wave devices - diffusion, surface-area, and pore-size distribution. *Acs Symposium Series* **403**, 208-221 (1989).
- 16 Bartlett, P. N. and Gardner, J. W. Diffusion and binding of molecules to sites within homogeneous thin films. *Philosophical Transactions of the Royal Society*

of London Series a-Mathematical Physical and Engineering Sciences **354**, 35-57
(1996).

Chapter 5

Conclusion and future work

5.1 Conclusion

This thesis has described the development and application of self-sensing NEMS resonator devices. The method of piezoresistive detection using thin metal film as the sensing material is discussed in detail. For NEMS, the advantages of using metallic film over conventional semiconductor materials are analyzed theoretically and demonstrated experimentally. These advantages mostly stem from the low resistivity and high electron density of metallic material. They include the low Johnson noise and $1/f$ noise, low device impedance for optimal impedance matching with RF readout electronics, ease and robustness of fabrication at nanoscale, and versatile selection of substrate. By using such a method, nanoscale NEMS resonators (cantilevers) with resonance frequency up to the very high frequency (VHF) band are demonstrated. The readout sensitivity is thermomechanical noise limited, as verified by successful measurement of thermomechanical noise at room temperature. The nanomechanical resonators also show remarkable quality factor even at atmospheric pressures, due to their small dimensions (which are close to the mean free path of air). Further theoretical discussion and experimental study of this dimensional effect of damping in air are included. This high quality factor makes these nanomechanical resonators readily operational at everyday conditions, namely room temperature and atmospheric pressure. A successfully

demonstration using them for mass sensing in air is described. Mass sensing resolution below 1 attogram is achieved.

These nanomechanical resonators become highly sensitive chemical gas sensors after they are functionalized with chemically sensitive polymer films. The method of coating is developed. As detectors in a gas-chromatography-based integrated system, these nanomechanical resonators are proved superior in performance, including a very good limit of detection and very high response speed. Successful demonstration of separation and analysis of a complex mixture of various chemical compounds is achieved. Particularly, chemical warfare agent (CWA) simulants and their interferents can be clearly discriminated by the system. After optimization of the packaging of the system, an analysis time for 13 different species in as short as 4 seconds is obtained. With the sharpest peak width shorter than 100 milliseconds, the demonstrated optimal channel number is more than 40. The polymer film functionalized NEMS resonators are also very selective in that they are not responsive to interferents at orders of magnitude higher concentration than targeted analytes, indicating an excellent false-alarm rate. Although reduced sensitivity is observed when analysis speed is increased, due to the slow diffusion process inside the polymer layer, this drawback can be compensated for by fast pre-concentration of analyte before reaching the separation column.

In general, NEMS resonators have been demonstrated to be excellent chemical gas sensors, particularly suitable for microscale total analysis systems that require detection at high speed and high sensitivity. The use of the metallic film piezoresistive self-sensing method is the critical element that enables the application of the NEMS resonator in compact and convenient packages. Finally, the integration of NEMS

resonators with other microfabricated components, such as a pre-concentrator, GC column, and valves, is a successful demonstration of the merging of NEMS and MEMS technologies.

5.2 Future work

Integrated actuation

Operation of NEMS devices need both actuation or excitation and detection or readout of the devices. (Only noise measurement does not need actuation.) The integrated metallic piezoresistive detection method described in this thesis successfully makes the NEMS device self-sensing. However, the actuation method employed in this research is still not integrated — a piezoelectric disk is used to actuate or shake the whole device chip. This method is not only bulky and inconvenient, but also inefficient. In addition, all the devices on the same chip are actuated at the same time, but cannot be excited individually at different frequencies. This lack of efficient integrated actuation is the major hurdle to further implementation of NEMS, in multiplexed large-array devices, or for feedback control of the devices.

Other traditional actuation methods include magnetomotive and optic-thermal driving. The strong magnetic field and the optical system are not scalable. Alternative methods need to be developed. One very promising candidate is to integrate piezoelectric material at the device. Piezoelectric material can provide mechanical actuation when electrical voltage is applied, just like the piezoelectric shaker disk that was used before. Commonly seen strong piezoelectric materials are some ceramics with perovskite

structure, such as BaTiO₃, SrTiO₃, and PbZrTiO₃ (PZT). Some polymeric materials such as polymer polyvinylidene fluoride (PVDF) are also piezoelectric. III-V and II-VI semiconductor materials, including aluminum nitride (AlN), gallium nitride (GaN), zinc oxide (ZnO), and gallium arsenide (GaAs) are also piezoelectric. However, ceramic materials are difficult to deposit as thin films at submicron thickness and maintain their piezoelectricity, as are polymeric materials. The most promising materials are AlN and ZnO, which show piezoelectricity in deposited thin film, or even in bottom-up grown nanostructures. Further research into integration and application of these materials with the NEMS structure are still ongoing in our group. Some other challenges still remains with exciting possibilities. Problems such as the strong coupling and interference between actuation and detection, when both are integrated at nanoscale need to be solved.

Array and multiplexing

There are interests in multiplexing or developing an array of a large number of NEMS devices for many application purposes. For example, in chemical gas sensing, differentially coating each NEMS resonator sensors with chemically selective polymeric films, as shown conceptually in Figure 5-1, will enable classification and quantization of known and unknown analytes in complex mixture^{1,2}. Eventually, this sensor array integrated with a microscale gas chromatography system, can realize an “electronic nose” system with superior performance. Synchronized NEMS array can also improve the sensitivity of individual devices, for the signal can be averaged within the array so that the signal will be less susceptible to noise. As a concentration sensor, the areal sensitivity is also improved by a factor which equals the number of devices in the array, because the

frequency of each device remains, but the total surface area is the sum of all the devices in the array. For RF signal processing applications, using an array of devices improves the power-handling capability of the system. With reduced noise level, the dynamic range of the system can be dramatically augmented.

However, although fabrication of a large number of devices in an array is straightforward by lithography, operation of them collectively still remains a challenging task. In order to achieve this, NEMS devices need to be addressed (actuate and detect) individually or made to work synchronically and coherently^{3,4}. Solving these problems and understanding the operating principles will be critical to implementing the ideas. Their collective behavior in a nonlinear regime is also an interesting research subject.

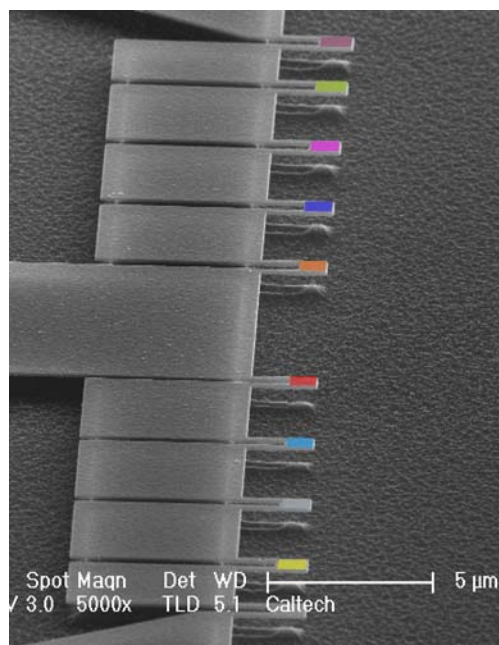


Figure 5-1 Differentially coated NEMS resonator array

Active feedback control

Feedback control is ubiquitous and a basic technique in electronic circuitry. It has also been used very often in the measurement of NEMS. In fact, phase-locked loop is a feedback controlled circuit where the signal from the NEMS resonator is used to control the voltage controlled oscillator, thus the loop is stabilized and the frequency of the NEMS resonator is tracked. Typical feedback control circuits use negative feedback. Positive feedback can be used to make self-excited loops or oscillators. A ultrahigh frequency oscillator has been demonstrated using NEMS as the frequency determining element⁵. But magnetomotive actuation detection is used, which makes such an oscillator not scalable. Given an integrated actuation technique, an integrated NEMS oscillator circuit can be developed and will have more application potentials.

Using active feedback, the effective quality factor NEMS resonator can also be improved. Such a technique applies a positive feedback that is proportional to the resonator's linear velocity, equivalently cancels out the damping forces and boosts the effective Q of the resonator by orders of magnitude. This method has already been applied to atomic force microscopy to achieve very high force resolutions even in aqueous measurement conditions⁶. Active Q control has not been demonstrated with the NEMS resonator yet. Potentially, the augmented Q will greatly improve the signal to noise ratio and accuracy of frequency measurement in ambient or even aqueous conditions. This will make liquid-phase chemical or biological sensing possible, and thus promise tremendous application opportunities.

5.3 Reference

- 1 Burl, M. C. *et al.* Classification performance of carbon black-polymer composite vapor detector arrays as a function of array size and detector composition. *Sens. Actuator B-Chem.* **87**, 130-149 (2002).
- 2 Park, J., Groves, W. A., and Zellers, E. T. Vapor recognition with small arrays of polymer-coated microsensors. A comprehensive analysis. *Analytical Chemistry* **71**, 3877-3886 (1999).
- 3 Sato, M. *et al.* Observation of locked intrinsic localized vibrational modes in a micromechanical oscillator array. *Phys. Rev. Lett.* **90**, - (2003).
- 4 Buks, E. and Roukes, M. L. Electrically tunable collective response in a coupled micromechanical array. *J. Microelectromech. Syst.* **11**, 802-807 (2002).
- 5 Feng, X. L., *et al.* *unpublished* (2006).
- 6 Tamayo, J. *et al.* High-q dynamic force microscopy in liquid and its application to living cells. *Biophysical Journal* **81**, 526-537 (2001).

Appendix A

Electrochemical deposition of nano-magnet tip on microscale scanning probes

In this appendix, a method to electrochemically deposit a high-aspect-ratio nano-magnet tip on scanning probes is described. Such a nano-magnet tip can provide high vertical magnetic field gradients as needed for magnetic resonance force microscopy (MRFM) and for magnetic actuation of a cantilever device. Electrochemical deposition is a versatile and robust way to fabricate metallic and metal oxide micro- and nanostructures. It is compatible with other integrated circuit fabrication processes. It is also a self-aligned process, as deposition can only happen at the position where the seed layer is exposed to solution. As described in the following, electrochemical deposition is also advantageous in the fabrication of structures with high vertical aspect ratios, which is rather challenging for other methods such as lithography, vacuum deposition, and lift-off. Excellent magnetic properties of electrodeposited magnetic films are reported, including nickel-iron, nickel-iron-copper, and cobalt-iron-copper alloys¹⁻³.

The electrodeposition setup of the experiment is shown in Figure A-1. A cathode plate made of copper and an anode plate made of nickel are connected to a DC power supply, with both the current and voltage measured by meters. The substrate of the sample is mounted on the cathode plate with a metallic clamp. It is crucial that the clamp makes good electrical contact with the seed layer on the substrate so that current can flow

to the seed layer. The both cathode and anode plates are inserted in to a beaker filled with electrodeposition solution. The composition of the solution for permalloy deposition is listed in Table A-1.

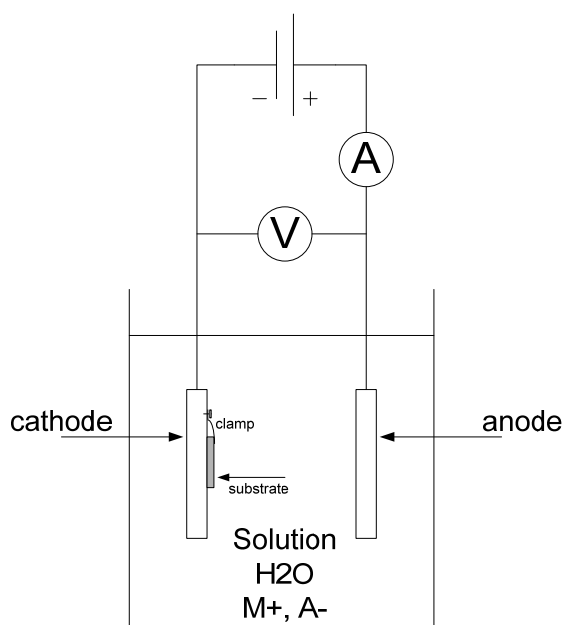


Figure A-1 Electrodeposition setup

Table A-1 Electrodeposition solution for permalloy ($\text{Fe}_{20}\text{Ni}_{80}$) electro-deposition

	$\text{NiSO}_4 \cdot 6\text{H}_2\text{O}$	$\text{FeSO}_4 \cdot 7\text{H}_2\text{O}$	$\text{NiCl}_2 \cdot 6\text{H}_2\text{O}$	H_3BO_3	Saccharin	PH
Amount (g/L)	200	8	5	25	3	2.5~3.0

The deposition rate depends on the current density at the solution and seed layer interface. And since the deposition rate is also critical in determining the formation and stoichiometry of deposited film and structure, it's important to optimize it. In Figure A- 2, the deposition rate is measured with a different current level. The area current density is also calculated using the total cathode plate area. It can be seen that the deposition rate

depends linearly on the current or current density as expected. Current density around 10–15 mA/cm² is suggested by the literature to obtain the best stoichiometry of permalloy³. Also, since very uniform agitation is hard to achieve in a small beaker, it is crucial to avoid any agitation in order to obtain uniform and consistent deposition¹.

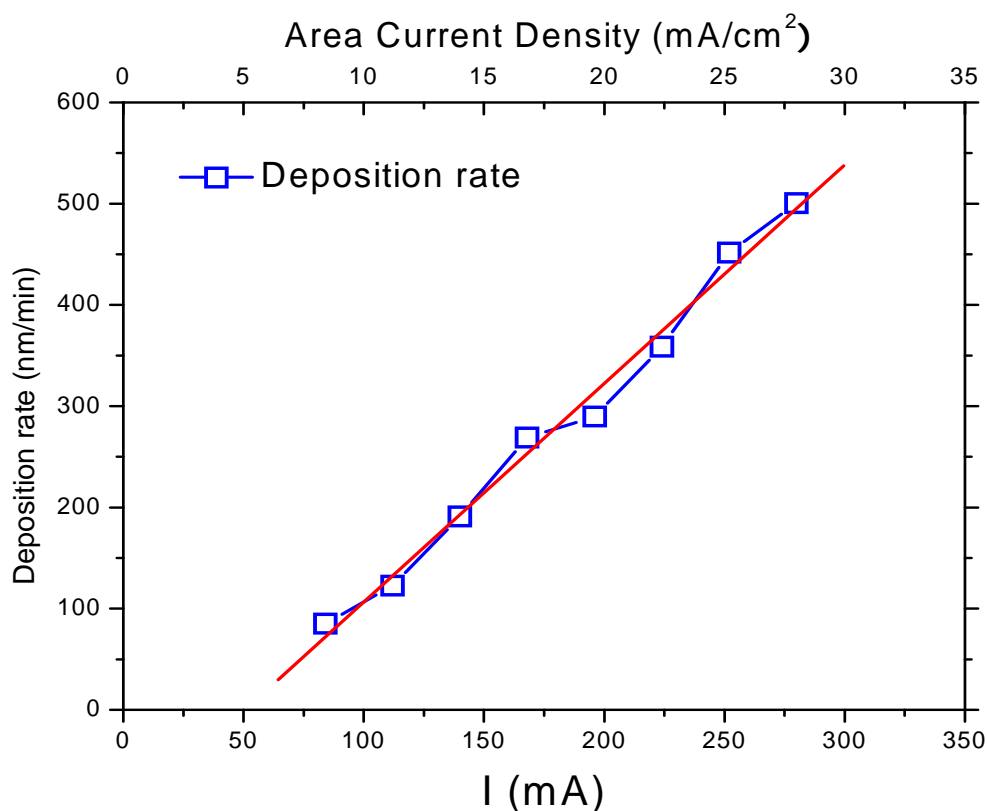


Figure A- 2 Deposition rate versus current density

To electrodeposit microscale structure, a seed layer or a mask layer can be patterned to allow deposition to only happen at the exposed area. Gold and copper are good seed layers for permalloy deposition. Both blank coating (Au/Cr) and patterned seed layer pads (Au/Cr) connected with conduction leads (Al) have been used successfully. A good electrical connection is crucial for successful deposition. PMMA electron beam resist is used as a mask layer on seed layers. A diagram shown in Figure A-3 explains the

patterning and deposition process. To acquire high aspect ratio, very thin PMMA layer is used. We use bi-layer of PMMA to improve the patterning. The first layer is 200 K A3 PMMA, which has a thickness of about 200 nm after the spinning. The second layer is 495 K A11 PMMA, which has a thickness of about 2 μm .

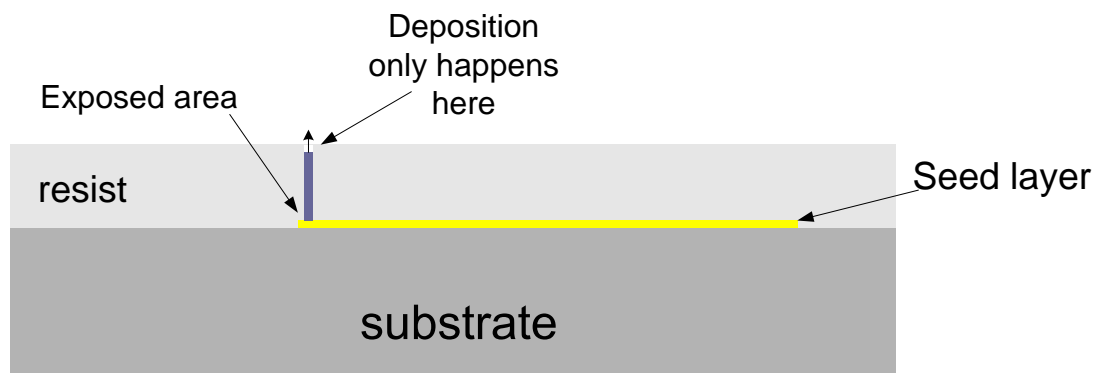


Figure A-3 Patterning the PMMA e-beam resist on a seed layer for self-aligned electrodeposition

Then the sample is patterned with electron beam lithography using JOEL 6400 SEM with 40 kV beam voltage. To fully expose the very thick PMMA layer, very large exposure dosage has to be used. The the smaller pattern size, the larger the areal dosage is needed. In Table A-2, typical exposure dosages for hole patterns with various sizes are listed.

Table A-2 Exposure dosage for hole patterns using on bilayer PMMA resist.

Hole diameter (μm)	1	0.5	0.2~0.3
Dosage Setup(nC/cm^2)	1600	2500~3000	4000~5000

The electrodeposition is conducted at current value of 120 mA–150 mA, which gives a current density of about 15 mA/cm² and a growth rate of about 150–200 nm/min. Typical results are shown in Figure A-4 and Figure A-5. In Figure A-4, a blank gold seed layer is used and an array of holes is patterned in PMMA. Then permalloy is electrodeposited inside the PMMA holes and forms high-aspect-ratio nanomagnets. A patterned seed layer can also be used to fabricate the nanomagnet at a specific site. In Figure A-5, a pad of gold seed layer is patterned and it is connected to outer electrodes by an aluminum line to allow electrical current to flow to the pad. This aluminum layer can be removed by using KOH etching after the electrodeposition. After the deposition, the PMMA layer can be dissolved in acetone with the nanomagnet staying firmly on the substrate. In Figure A-6, a nanomagnet is fabricated to the tip of a cantilever, although it is overgrown into the shape of a mushroom.

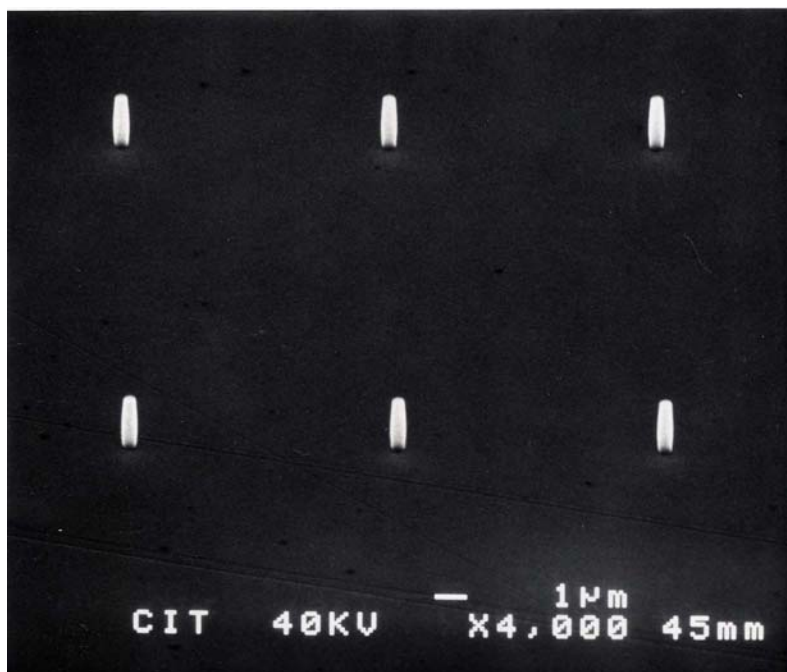


Figure A-4 Array of nanomagnets with dimension of 2 μm high and 300 nm wide

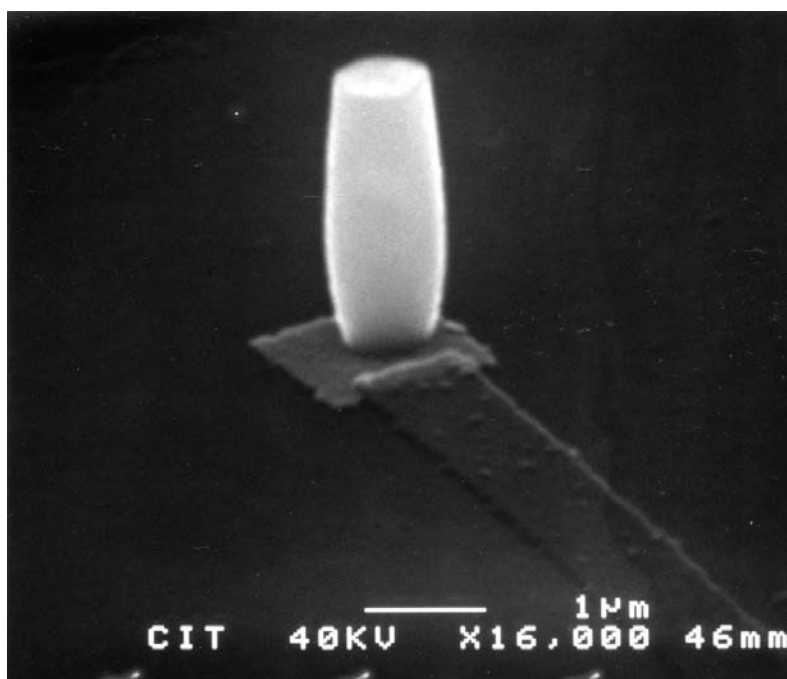


Figure A-5 A 500 nm by 2 μm permalloy nanomagnet on SiN membrane. The nanomagnet is grown on a gold seed layer pad. An aluminum line connects the pad to the outer electrodes and will be removed by KOH etch in a later step.

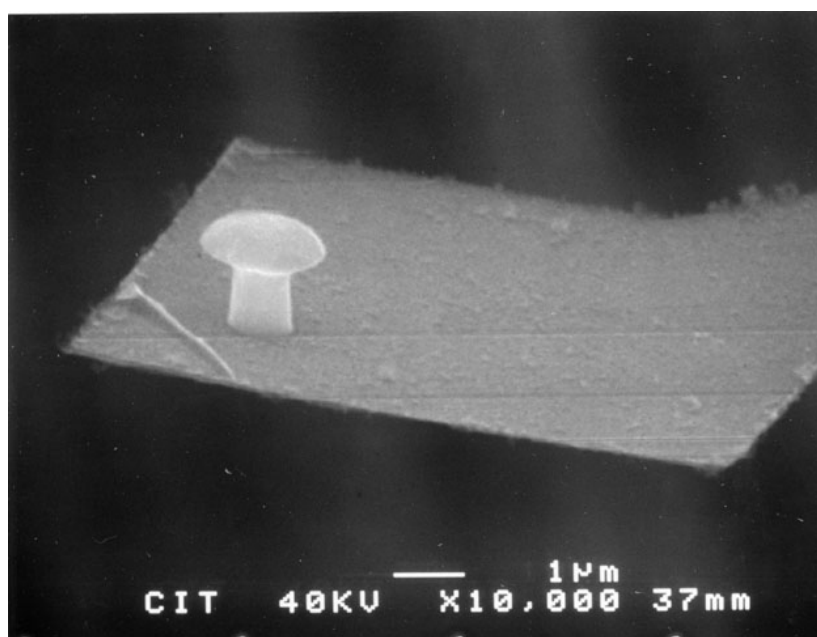


Figure A-6 A mushroom shaped overgrown nanomagnet on the tip of a release cantilever

Reference

- 1 Lemehaut.C and Rocher, E. Electrodeposition of stress-insensitive ni-fe and ni-fe-cu magnetic alloys. *Ibm Journal of Research and Development* 9, 141 (1965).
- 2 Gao, L. J. *et al.* Characterization of permalloy thin films electrodeposited on si(111) surfaces. *J. Appl. Phys.* 81, 7595-7599 (1997).
- 3 Park, J. Y. and Allen, M. G. Development of magnetic materials and processing techniques applicable to integrated micromagnetic devices. *Journal of Micromechanics and Microengineering* 8, 307-316 (1998).